

Numerical Analysis of Geosynthetic-reinforced Soil (GRS) Piers Using the Subloading t_{ij} Model

A THESIS SUBMITTED TO THE GRADUATE DIVISION OF THE UNIVERSITY OF HAWAII AT
MĀNOA IN PARTIAL FULFILLMENT OF THE REQUIREMENTS FOR THE DEGREE OF
MASTER OF SCIENCE
IN
CIVIL ENGINEERING

August 2024

BY

Miles Alexander Drazkowski

Thesis Committee:

Dr. Phillip S. K. Ooi, Committee Chair

Dr. Amin Rafiei

Dr. Osvaldo Paiva Magalhães Vitali

Acknowledgments

My sincere gratitude and thanks go out to all the following people without whom this report would not have been possible.

- My advisor, Dr. Phillip S.K. Ooi, whose support, insight, and care have inspired and helped me navigate my master's program and chart a course through my future academic and professional career.
- Dr. Teruo Nakai for providing the Subloading*tij.exe* program and the Subloading t_{ij} user defined model, without which this work would not be feasible.
- Dr. Phillip Ooi, Dr. Amin Rafiei, Dr. Osvaldo P.M. Vitali, thank you all for agreeing to sit on my master's committee and share in a discussion of this work.
- Dr. Phillip Ooi, Dr. Amin Rafiei, Dr. Melia Talagi, Dr. Harry Lee, Dr. Adrian Archilla, and Dr. Mohammed Rahman for the insightful and interesting courses you provided during my master's course of study, increasing my knowledge, and preparing me for my academic and professional career.
- Ms. Jean Zhang for all the help and answered questions she provided during my time at UH Mānoa.
- My cohort and lab group, stressing with me and pushing to improve, to be that much better. You provided a sounding board but also a group of true partners and peers.
- To my friends, for your support and kindness. For the words of encouragement and the insight, motivating me to improve and pursue this work.
- Finally, my family, whose support and love are my most precious possession.

Abstract

Over the past half-century geosynthetic reinforced soil (GRS) structures have become increasingly ubiquitous, and for good reason (Müller & Saathoff, 2015). Geosynthetics offer rapid deployment, are cost-effective, can reduce the carbon footprint generated by traditional reinforced concrete designs, and produce resilient earthwork structures. As the use of geosynthetics has become more prevalent, novel design implementation, risk factors, and material interaction have become areas of increased study. The focus of this paper is to provide insight into the settlement behavior and bearing capacity of various GRS “mini pier” configurations with particular interest in GRS implementation as bridge abutments.

This paper is primarily concerned with the deployment of GRS in the so-called Integrated Bridge System (GRS-IBS). The results presented herein are intended to model and provide insight into the large-scale load testing behavior performed by the Federal Highway Administration (2013). These large-scale load tests investigated the axial load-deformation behavior of GRS columns and provided design guidance for implementation in GRS-IBS applications. Due to the cost-prohibitive nature of large-scale load testing, this paper utilizes numerical solutions as a viable alternative.

PLAXIS 3D finite element analysis software was utilized to perform numerical simulations of load tests on GRS columns. To model the behavior of the granular soil, this study utilized the Subloading t_{ij} constitutive model first proposed by Nakai and Mihara (1984). The model is based on the “Spatially Mobilized Plane” (SMP) stress space concept originally proposed by Matsuoka and Nakai (1974) and is outlined in Nakai (2013).

Prior to numerical simulation, optimized Subloading t_{ij} model parameters were obtained using two soft algorithms and the existing “Subloading_Tij.exe” element software (Nakai T., tij地盤解析研究会). A Python script was written to run the element software, generating triaxial and isotropic compression test data which was then compared to the laboratory test results from FHWA (2013). Optimization of model parameters to the laboratory test results involved both the differential evolution and “emcee” algorithm and was conducted using the “Model” class provided by LMFIT (Newville, et al., 2023).

Parameter optimization yielded the following conclusions and results of note. By modeling the parameter space of the Subloading t_{ij} model, a graph of bivariate contours of the model’s local posterior distribution demonstrated parametric interaction during optimization. A second conclusion observed is that there is a possibility of localized overfitting that can produce non-optimum model performance despite apparent desirable statistical outcomes.

The optimized model parameters were used to create a three-dimensional (3D) finite element (FE) model of selected large-scale GRS column load tests in PLAXIS 3D. A Subloading t_{ij} user-defined model provided by (Nakai n.d.) was imported into PLAXIS as a dynamic link library (.dll) to model the soil. The study successfully modeled the unfaced GRS pier load-deformation curves well, largely matching the experimental results.

Table of Contents

Acknowledgments.....	i
Abstract.....	ii
Table of Figures	vi
1. Introduction.....	1
1.1 Objectives	1
1.2 Motivation	2
1.3 Thesis Outline.....	4
2. Literature Review.....	5
2.1 Subloading t_{ij} Model.....	5
2.2 Finite Element Method.....	19
2.3 Numerical Modeling of GRS Mini-Piers.....	20
2.4 Optimization with Machine Learning.....	27
3. Mini-pier Performance Testing	32
3.1 Test Setup	32
3.2 Aggregate, Geosynthetic, and Facing.....	34
3.2.1 Aggregate Backfill	34
3.2.2 Geotextile Reinforcement	37
3.2.3 CMU Facing.....	38
3.3 Load Testing and Instrumentation	38
3.4 Results	42
4. Model Input Parameters.....	52
4.1 Aggregate	52
4.1.1 Test Results	52
4.1.2 Subloading t_{ij} Model Parameters	57
4.1.3 Machine Learning Implementation	58
4.1.4 Parameter Optimization Results.....	61
4.2 Geosynthetics	68
4.3 Interface Elements	69
4.4 Summary.....	70
5. Numerical Modeling	72
5.1 PLAXIS 3D Model Input	72
5.2 PLAXIS 3D Model Overview	74

5.3	Model Runs	76
6.	Results.....	83
6.1	Stress Development.....	83
6.2	Vertical Displacement.....	88
6.3	Horizontal Displacement	90
7.	Conclusions.....	96
7.1	Conclusions	96
7.2	Recommendations	97
8.	References.....	98
9.	Appendix A	103
10.	Appendix B	111

Table of Figures

Figure 1-1 Typical cross-section of a GRS-IBS abutment (Adams et al., 2011)	1
Figure 1-2 Faced "mini pier" load testing conducted by the FHWA. (Nicks et. al, 2013).....	2
Figure 1-3 Un-faced "mini pier" load testing conducted by the FHWA. (Nicks et. al, 2013)	2
Figure 2-1 Mohr's circles under three different principal stresses. (Nakai T. , 2013)	6
Figure 2-2 Spatially mobilized plane in three-dimensional principal stress space. (Nakai T. , 2013)	6
Figure 2-3 Definition of modified stress invariants (t_N and t_S) in modified stress space. (Nakai T. , 2013)	8
Figure 2-4 Definition of modified strain invariants ($d\varepsilon_N^*$ and $d\varepsilon_S^*$) in strain increment space. (Nakai T. , 2013)	9
Figure 2-5 Shape of SMP criterion, Extended Von Mises criterion, and Mohr-Coulomb criterion on the octahedral plane in principal stress space (Nakai, 2013)	10
Figure 2-6 Initial and current yield surfaces in the modified shear-normal (t_N-t_S) plane and direction of plastic flow for t_{ij} model. (Nakai T. , 2013)	11
Figure 2-7 Stress-dilatancy behavior of the t_{ij} model (Nakai and Hinokio, 2004).....	12
Figure 2-8 Change in void ratio on an e -ln p plot. (Nakai T. , 2013).....	15
Figure 2-9 Observed stress-dilatancy relationship under different stress paths; Left: in terms of q/p and $d\varepsilon_v/d\varepsilon_d$; Right: in terms of t_S/t_N and $d\varepsilon_N^*/d\varepsilon_S^*$. (Nakai T. , 2013)	16
Figure 2-10 Plastic strain increments $d\varepsilon_{ij}^{p(AF)}$ and $d\varepsilon_{ij}^{p(IC)}$, shown on the modified shear-normal plane (Nakai T. , 2013)	17
Figure 2-11 The effect of soil-facing friction angle on the load-settlement curve of TF-6 (left) and TF-7 (right). (Kaya, 2016)	21
Figure 2-12 The effect of soil-facing friction angle on the lateral displacement of TF-6 (left) and TF-7 (right) at 4, 8, and 12 inches of settlement. (Kaya, 2016).....	21
Figure 2-13 The effect of the facing's constitutive model on the TF-6 load-settlement curve. (Kaya,2016)	22

Figure 2-14 The effect of the facing's constitutive model on lateral displacement of TF-6 at 4, 8, and 12 inches of settlement. (Kaya, 2016).....	22
Figure 2-15 The effect of geosynthetic constitutive model on the load-settlement curve of TF-6 (left) and TF-7 (right). (Kaya, 2016)	23
Figure 2-16 The effect of the geosynthetic constitutive model on lateral displacement of TF-6(right) and TF-7(left) at 4, 8, and 12 inches of settlement. (Kaya, 2016)	23
Figure 2-17 The results of Subloading t_{ij} best fit using triaxial test results. (Kaya, 2016)	24
Figure 2-18 Vertical load-displacement curve for mini piers TF-6 and TF-9. (Shen, et al., 2019).....	25
Figure 2-19 Lateral load-displacement curve for mini piers TF-6 (left) and TF-9 (right). (Shen, et al., 2019)	25
Figure 2-20 The resulting displaced shape of the finite difference analysis vs the resulting shape of the load testing for TF-6. (Shen, et al., 2019)	26
Figure 2-21 General description of deformed shape for faced GRS mini piers. (Shen, et al., 2019)	27
Figure 2-22 Affine-invariant MCMC algorithm step. (Foreman-Mackey et al., 2013)	30
Figure 2-23 The emcee algorithm step. (Foreman-Mackey et al., 2013).....	30
Figure 3-1 Typical GRS mini pier elevation view with instrumentation. (Nicks et al., 2013).....	33
Figure 3-2 Typical Cross section (top view) and CMU facing dimensions for GRS mini pier. (Nicks et al., 2013)	33
Figure 3-3 VDOT 21A aggregate backfill aggregate. (Nicks et al., 2013)	34
Figure 3-4 Results of standard Proctor test on the aggregate backfill, VDOT 21A. (Nicks et al., 2013) ...	35
Figure 3-5 Results of large-scale direct shear testing conducted on various backfill materials. (Nicks et al., 2013)	35
Figure 3-6 Comparison of saturated, unsaturated, and fully softened Mohr-Coulomb envelopes. (Iwamoto, 2014)	36
Figure 3-7 Staged construction employed to construct FHWA GRS test piers. (Iwamoto, 2014).....	37
Figure 3-8 Schedule of geosynthetic properties utilized during GRS pier load tests. (Iwamoto, 2014)....	37

Figure 3-9 CMU block dimensions. (Iwamoto, 2014).....	38
Figure 3-10 FHWA TFHRC GRS mini pier load testing set up. (Iwamoto, 2014).....	38
Figure 3-11 Spherical bearing interface between hydraulic jack and footing. (Nicks et al., 2013)	39
Figure 3-12 Schematics of deflection instrumentation for mini piers (a) with facing and (b) without facing. (Iwamoto, 2014).....	40
Figure 3-13 Instrumentation and schematic for a) plan and profile of TF-6 and b) plan and profile of TF-7. (Iwamoto, 2014).....	41
Figure 3-14 Instrumentation and schematic for a) plan and profile of TF-9 and b) plan and profile of TF-10. (Iwamoto, 2014).....	42
Figure 3-15 Vertical load-displacement curves for all of the TFHRC load tests. (Nicks et al., 2013).....	44
Figure 3-16 TF-10 at failure with $S_v = 15\frac{1}{4}$ inches, $T_f = 4,800 \text{ lb/ft}$, and VDOT 21A material. (Nicks et al., 2013)	44
Figure 3-17 Normalized load-settlement curves for selected TFHRC GRS mini pier load tests. (Iwamoto, 2014)	45
Figure 3-18 For TF-6: a) through i) images of individual reinforcement rupture; j) elevation view of reinforcement rupture. (Iwamoto, 2014).....	46
Figure 3-19 TF-6 ($S_v = 7\frac{5}{8}$ inches, $T_f = 4,800 \text{ lb/ft}$) facing cracking and crushing post load testing. (Nicks et al., 2013)	47
Figure 3-20 Fatback cell measured lateral pressures during load testing of TF-6, -9, -12, and -14. (Iwamoto, 2014).....	48
Figure 3-21 Lateral deflections along GRS pier height for TF-6.....	49
Figure 3-22 Lateral deflections along GRS pier height for TF-7.....	49
Figure 3-23 Lateral deflections along GRS pier height for TF-9.....	50
Figure 3-24 Lateral deflections along GRS pier height for TF-10.....	50
Figure 3-25 Lateral deformation profiles of GRS piers at approximately 83% of ultimate load capacity. (Iwamoto, 2014).....	51

Figure 4-1 Results of isotropic consolidation testing, e - $\log p$ curve.....	53
Figure 4-2 Membrane volumetric strain correlation with horizontal stress.	53
Figure 4-3 Deviator stress vs. axial strain from consolidated drained triaxial tests with $\sigma_3 = 5, 10, 20,$ and 30 psi.....	54
Figure 4-4 Volume change curves for consolidated drained triaxial tests.....	55
Figure 4-5 Stress ratio vs. axial strain curves for CD triaxial tests.....	55
Figure 4-6 R_{cs} vs axial strain curves for CD triaxial tests.....	56
Figure 4-7 e - $\log p$ (volume change curves) for CD triaxial tests.....	57
Figure 4-8 Stress-strain curves for triaxial tests from CD testing vs model simulation.	62
Figure 4-9 Triaxial volume change curves from CD testing vs model simulation.	62
Figure 4-10 e - $\log p$ curve from IC testing vs model simulation.	63
Figure 4-11 Correlation plots for triaxial tests: Top Left - q at $\sigma_3 = 5$ psi; Top Right - ε_v at $\sigma_3 = 5$ psi; Center Left - q at $\sigma_3 = 10$ psi; Center Right - ε_v at $\sigma_3 = 10$ psi; Bottom Left - q at $\sigma_3 = 30$ psi; Bottom Left - ε_v at $\sigma_3 = 30$ psi.....	65
Figure 4-12 Correlation plot for IC test: Left - e ; Right - p	66
Figure 4-13 Simplified corner plot for optimization using just volumetric testing data.....	66
Figure 4-14 corner plot for optimization using triaxial testing data.	67
Figure 4-15 Acceptance fraction for the emcee optimization procedure.	67
Figure 4-16 Idealized interface behavior (Nakai T. , 2013).	70
Figure 5-1 PLAXIS 3D parameter input for user-defined Subloading tij .dll.....	73
Figure 5-2 Alternating pattern geotextile layers (red-yellow) and plate (dark blue) with interfaces (turquoise):.....	73
Figure 5-3 Soil after the removal of the volumes with unsaturated confining loads.	74
Figure 5-4 PLAXIS generated mesh using the "medium" element distribution.....	75
Figure 5-5 PLAXIS individual stage control parameters.....	76

Figure 5-6 Comparison of different user-defined model .dlls using the same Subloading t_{ij} parameters..	77
Figure 5-7 TF7 model simulation results using different Subloading t_{ij} parameters compared to test data.	
.....	78
Figure 5-8 Comparison of the various Subloading t_{ij} parameter sets to testing data for TF-7.....	79
Figure 5-9 Stress-strain curve for triaxial tests from CD testing vs Averaged parameter model simulation.	
.....	80
Figure 5-10 Triaxial volume change curves from CD testing vs Averaged parameter model simulation...	80
Figure 5-11 e - log p curve from IC testing vs Average parameter model simulation.	81
Figure 5-12 Sensitivity analysis of mesh density selection in PLAXIS	82
Figure 6-1 TF-7 45° diagonal cross-section shear stress distribution: σ_{yz} (kPa) – Left, σ_{zx} (kPa) - Right..	84
Figure 6-2 TF-7 YZ-plane cross-section stress distributions: σ_{zx} (kPa) – Left, σ_{xx} (kPa) - Right.....	85
Figure 6-3 TF-7 XZ-plane cross-section stress distributions: σ_{yz} (kPa) – Left, σ_{yy} (kPa) - Right.....	85
Figure 6-4 Deviatoric strain γ_s distributions: Left - YZ cross section, Right - XZ cross section.....	85
Figure 6-5 TF-7 geotextile force distributions: N_1 (in-plane force, kN/m) – Left, Q_{12} (in-plane shear, kN/m) - Right.....	86
Figure 6-6 TF-10 45° diagonal cross-section shear stress distribution: σ_{yz} (kPa) – Left, σ_{zx} (kPa) - Right.86	
Figure 6-7 TF-10 XZ-plane cross-section stress distributions: σ_{yz} (kPa) – Left, σ_{yy} (kPa) - Right.....	86
Figure 6-8 TF-10 YZ-plane cross-section stress distributions: σ_{zx} (kPa) – Left, σ_{xx} (kPa) - Right.....	87
Figure 6-9 Deviatoric strain γ_s distributions: Left - XZ cross section, Right - YZ cross section.....	87
Figure 6-10 TF-10 geotextile force distributions: N_2 (in-plane force, kN/m) – Left, Q_{12} (in-plane shear, kN/m) - Right.....	87
Figure 6-11 TF-7 vertical displacement at the center of the top of the pier.	89
Figure 6-12 TF-10 vertical displacement at the center of the top of the pier.	89
Figure 6-13 TF-7 and TF-10 vertical displacements vs PLAXIS models.....	90
Figure 6-14 TF-7 horizontal displacement at 0 to 0.90 inches of vertical displacement.	92
Figure 6-15 TF-7 horizontal displacement at 1.08 to 2.59 inches of vertical displacement.	92

Figure 6-16 TF-7 horizontal displacements at 3.65 to 9.54 inches of vertical displacement.....	93
Figure 6-17 TF-10 horizontal displacements at 0 to 0.39 inches of vertical displacement.....	93
Figure 6-18 TF-10 horizontal displacements at 0.50 to 1.56 inches of vertical displacement.....	94
Figure 6-19 TF-10 horizontal displacements at 1.46 to 3.86 inches of vertical displacement.....	94
Figure 6-20 PLAXIS vertical pressure vs horizontal displacement behavior curves.....	95

1. Introduction

1.1 Objectives

The fundamental objective of this study is to numerically simulate the behavior of a series of load tests performed on unfaced geosynthetic reinforced soil (GRS) “mini piers” conducted by the Federal Highway Administration or FHWA (Nicks et. al, 2013). This study aims to reproduce the test behavior using numerical modeling by way of finite element (FE) software (PLAXIS 3D 2024) allowing for economical desk analysis of GRS behavior rather than the more laborious and expensive physical testing. The primary purpose of the FHWA load testing that was performed was to comment on parametric relationships and to assist in the creation of a design methodology for GRS-IBS (Integrated Bridge System). Figure 1-1 below shows the typical cross-section of a GRS-IBS abutment. Figure 1-2 and Figure 1-3 show the two general GRS load test configurations, faced and un-faced, respectively.

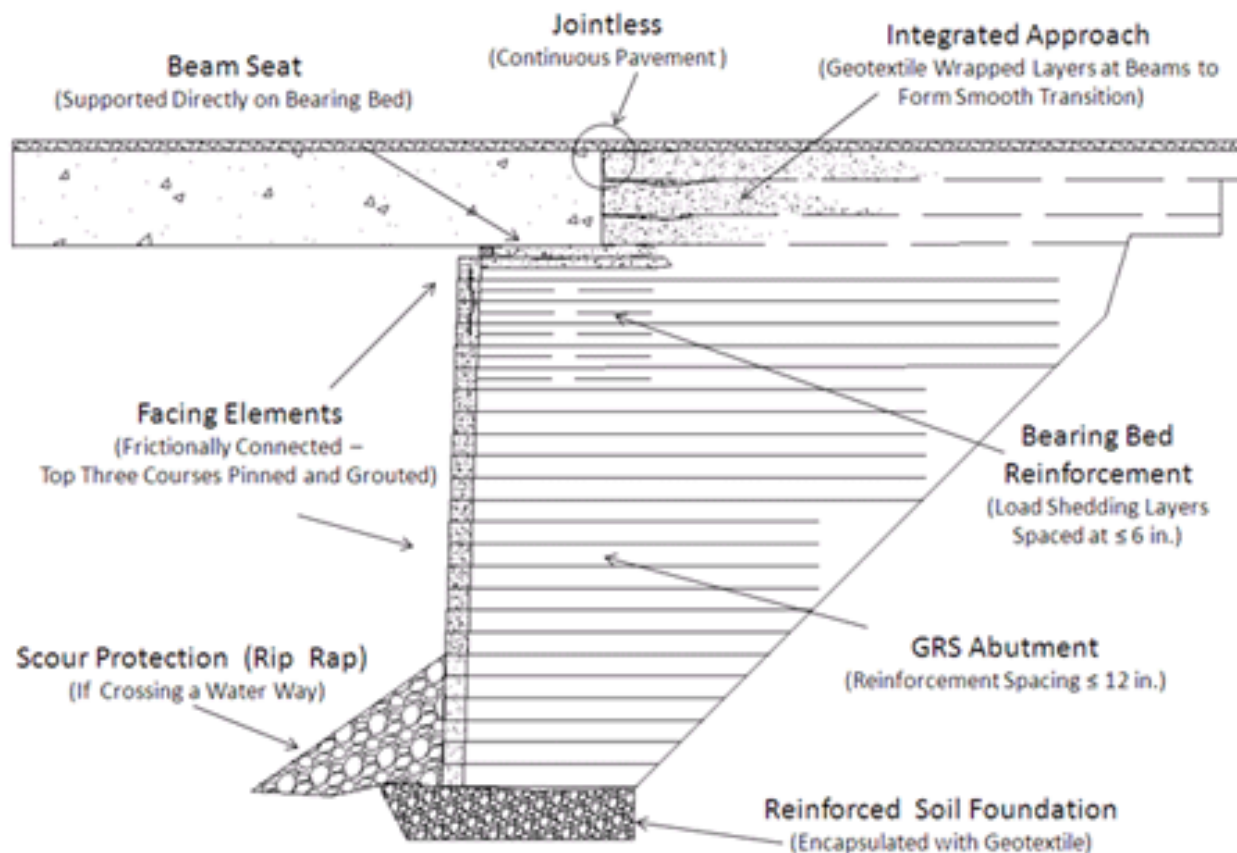


Figure 1-1 Typical cross-section of a GRS-IBS abutment (Adams et al., 2011)



Figure 1-2 Faced "mini pier" load testing conducted by the FHWA. (Nicks et. al, 2013)



Figure 1-3 Un-faced "mini pier" load testing conducted by the FHWA. (Nicks et. al, 2013)

1.2 Motivation

Bridges are vital pieces of infrastructure that provide critical access to a wide array of emergency responses as well as to the general public. However, bridge construction is a costly and time-intensive endeavor. Optimizing constructability, cost-efficiency, and long-term reliability have all been areas of interest and study (Zhao et al., 2021, 2022, etc.). GRS is defined as closely spaced (≤ 0.3 m) layers of geosynthetic reinforcement and compacted granular fill material (Adams et al., 2011). GRS bridge abutments were first constructed in Japan in the 1980s (Tatsuoka et al., 1997). Studies and implementation demonstrated that GRS offered superior cost advantage, superior performance, in terms of wall deformability, wall stability, and wall face durability and pleasing aesthetics (Tatsuoka et al., 1997). In the late 2000s and early 2010s, the GRS integral bridge concept was developed and implemented (Tatsuoka et al., 2016). Numerous examples of studies attempting to understand GRS

behavior exist in the literature (Nicks et al, 2013, Wu and Ooi, 2015, Tatsuoka et al., 2016). Of particular interest to this report, are the FHWA large-scale load tests (Nicks et al., 2013).

Kaya (2016) cites 7 primary advantages of the GRS-IBS (Integrated Bridge System) concept.

1. “Fast and cost-effective method of bridge support. It eliminates the need for cast-in-place reinforced concrete abutments traditionally supported on deep foundations.”
2. “Reduced carbon footprint with less use of concrete and hence cement, the production of which is known to contribute significantly to global warming.”
3. “Quality compaction control can be realized since backfill is placed in thin lifts between the closely spaced geosynthetics.”
4. “Closely-spaced geosynthetic systems are not prone to catastrophic abutment collapse. This has been observed in numerous load tests carried out to failure (Nicks et al., 2013).”
5. “Can be built in variable weather conditions with common labor, materials, and equipment, and can be easily modified in the field.”
6. “Alleviates the ‘bump at the end-of-the-bridge’ problem caused by differential settlement between the bridge abutment and the approach roadway. This is made possible by eliminating deep foundations, by using GRS to construct the integrated approach to the superstructure and by limiting its use to short, single-span integral abutment bridge systems.”
7. “Very flexible system that is amenable to differential settlement.”

GRS has been used as part of an integral bridge system in which the bridge abutment is the GRS backfill itself (Adams et al., 2011). Nick et al. (2013) conducted several load tests on GRS columns with different geotextiles, geotextile spacings, soil, and with and without facing. Kaya (2013) performed a 2D plane strain numerical simulation of the FHWA large-scale load tests using an FE program (FEMtij). That analysis employed the Subloading t_{ij} constitutive model (Nakai and Mihara (1984) while recognizing that a 3D analysis is more appropriate. At that time, Kaya (2013) did not have reliable 3D FEM software that utilized the Subloading t_{ij} constitutive model at his disposal. Kaya (2013) highlighted the need to numerically model the costly large-scale GRS column testing as an economical alternative.

Numerous studies employing simple constitutive models to simulate existing GRS bridge abutments and large-scale testing of GRS structures exist in the literature (Ardah et al., 2017; Helwany et al., 2003, 2007; Mirmoradi and Ehrlich, 2015; Pham, 2009; Shen et al., 2019; Taeb and Ooi, 2020; Zheng and Fox, 2016; among many). Despite the extensive literature on numerical simulations of GRS structures, very few numerical simulations have been conducted in 3D conditions (Shen et al., 2019; Zheng et al., 2018). The above studies have largely employed simple constitutive models (e.g. Mohr-Coulomb and Hardening Soil) to model the soil media response. In general, more complex soil loading and behavior have largely been ignored with Huang et al. (2009) implying that there exists a negligible difference between these simpler models and more complex models that capture a wide range of soil behavior. However, it is well known that it is challenging for simple constitutive models to fully mimic soil element tests well in terms of both stress-strain and volume change behavior. To fully account for material behavior during numerical modeling of the FHWA large-scale load test of GRS mini piers (Nicks et al., 2013), Dr. Teruo Nakai’s Subloading t_{ij} model (Nakai, 2013) is adopted.

1.3 Thesis Outline

Chapter 2 summarizes a review of the literature on the Subloading t_{ij} model (Nakai, 2013) as well as some work on numerical modeling of GRS. The FHWA GRS column load test configurations and experimental results are contained in Chapter 3. In Chapter 4, justification of the model input parameters for the GRS column elements are elucidated. Chapter 5 presents the results of the numerical load tests. The report ends with a summary, conclusions, and a short section on suggestions for future research.

2. Literature Review

2.1 Subloading t_{ij} Model

The Subloading t_{ij} model for geomaterials was developed and proposed to address issues that arise in critical state soil models (namely the Cam clay model; Roscoe, 1968). The model aims to present a simple yet sophisticated model that can address 11 specific shortcomings of the Cam clay model. The Cam Clay model has problems in describing the following as indicated in Nakai (2013):

1. “Influence of intermediate principal stress on the deformation and strength of geomaterials”
2. “Dependency of the direction of plastic flow on the stress path”
3. “Positive dilatancy during strain hardening”
4. “Stress-induced anisotropy and cyclic loading”
5. “Inherent anisotropy”
6. “Influence of density and/or confining pressure on deformation and strength”
7. “Behavior of structured soils such as naturally deposited clay”
8. “Time-dependent behavior and rheological characteristics”
9. “Temperature-dependent behavior”
10. “Behavior of unsaturated soils”
11. “Influence of particle crushing”

While several of these features are likely not central factors in accurately simulating the FHWA load tests, several are essential to accurately represent the stress conditions. For example, simulating the stress distribution in the mini piers necessitates the consideration of non-linear stress-strain behavior, the effect of the intermediate principal stress, the influence of density and confining pressure, as well as stress-induced anisotropy of the soil media, all of which are likely non-trivial.

The Subloading t_{ij} model was first proposed by Nakai and Mihara (1984) and was based on the spatially mobilized plane (SMP) concept (Matsuoka and Nakai, 1974). The SMP concept was formulated based on the maxim that soil behavior is fundamentally governed by frictional law. Any model formulated using Cambridge mean (p) and deviator (q) stresses with respect to the 2D octahedral plane can be easily transformed. By defining the stress vector t_{ij} with respect to the SMP, where t_N and t_s are analogous normal and in-plane components, the previously 2D model can be described in 3D stress space. Flow rules can be likewise transformed to apply not in σ_{ij} space but in t_{ij} space.

The SMP can be thought of as the most frictionally mobilized plane of soil particles where, on average, the ratio of shear to normal stress is largest. Matsuoka and Nakai (1974) postulate that the SMP does not remain parallel to the intermediate principal stress axis in principal stress space. The SMP’s position is influenced by the intermediate stress resulting in a plane that is not fixed in principle stress space as it is dependent on existing stress conditions. The SMP’s sides delineate the maximum shear-normal stress ratio. The resulting SMP will only become co-planar with the octahedral plane under isotropic stress conditions (Nakai T. , 2013). Figure 2-1 and Figure 2-2 show the SMP in relation to Mohr’s circles and the principal stress space. Finding the maximum shear-normal stress ratio for each circle leads to multiple mobilized friction angles as seen in Figure 2-1.

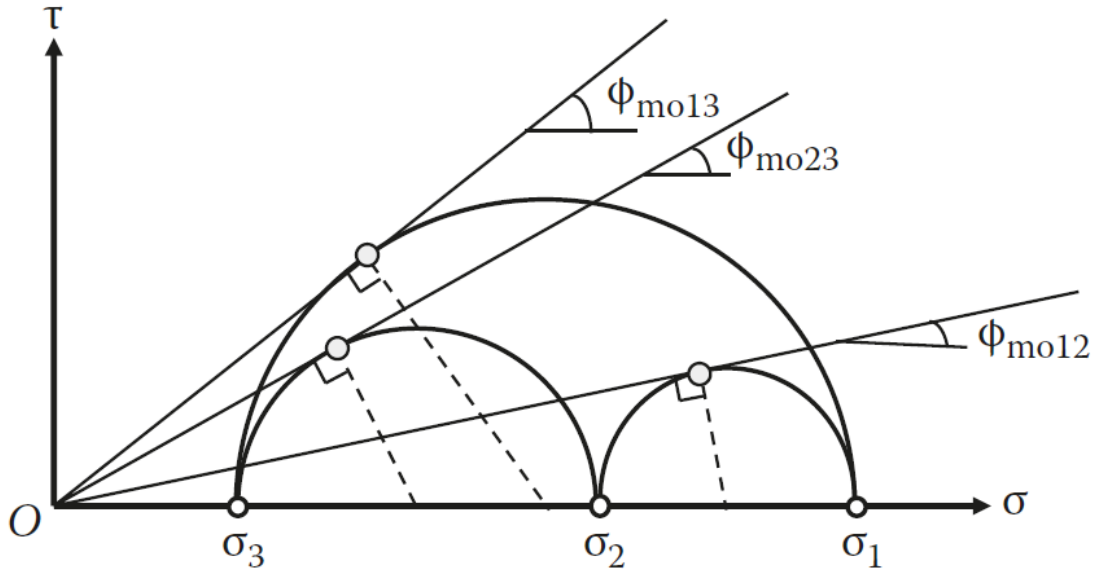


Figure 2-1 Mohr's circles under three different principal stresses. (Nakai T. , 2013)

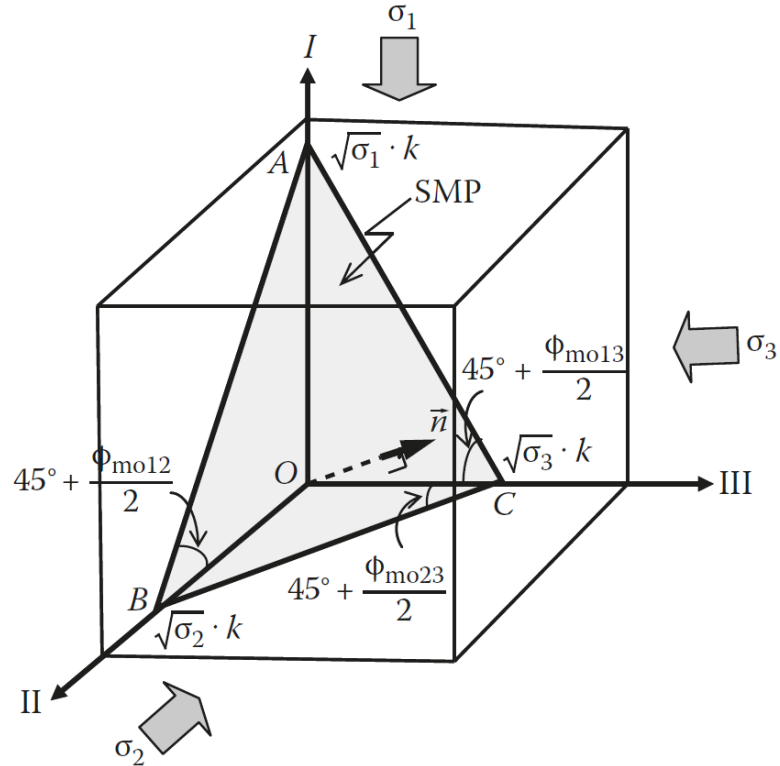


Figure 2-2 Spatially mobilized plane in three-dimensional principal stress space. (Nakai T. , 2013)

From Figure 2-1 and Figure 2-2, the following equation holds based on the intersection of the SMP and principal stress coordinate axes (Nakai, 1989):

$$\tan\left(45^\circ + \frac{\phi_{moij}}{2}\right) = \sqrt{\frac{1 + \sin\phi_{moij}}{1 + \cos\phi_{moij}}} = \sqrt{\frac{\sigma_i}{\sigma_j}} \quad (i, j = 1, 2, 3; i < j) \quad (\text{Eq 2.1})$$

The normal to the SMP is related to the directional cosines (a_1 , a_2 , and a_3), which are defined in terms of the stress invariants (I_1 , I_2 , and I_3) of the stress tensor (σ_{ij}) and the square root stress invariants (I_{r1} , I_{r2} , and I_{r3}) of the root tensor (r_{ij}) (Nakai, 1989):

$$I_1 = \sigma_1 + \sigma_2 + \sigma_3 = \sigma_{ii} \quad (\text{Eq 2.2.1})$$

$$I_2 = \sigma_1\sigma_2 + \sigma_2\sigma_3 + \sigma_3\sigma_1 = \frac{1}{2}\{(\sigma_{ii})^2 - \sigma_{ij}\sigma_{ji}\} \quad (\text{Eq 2.2.2})$$

$$I_3 = \sigma_1\sigma_2\sigma_3 = \frac{1}{6}\varepsilon_{ijk}\varepsilon_{lmn}\sigma_{il}\sigma_{jm}\sigma_{kn} \quad (\text{Eq 2.2.3})$$

$$I_{r1} = \sqrt{\sigma_1} + \sqrt{\sigma_2} + \sqrt{\sigma_3} = r_{ii} \quad (\text{Eq 2.3.1})$$

$$I_{r2} = \sqrt{\sigma_1\sigma_2} + \sqrt{\sigma_2\sigma_3} + \sqrt{\sigma_3\sigma_1} = \frac{1}{2}\{(r_{ii})^2 - r_{ij}r_{ji}\} \quad (\text{Eq 2.3.2})$$

$$I_{r3} = \sqrt{\sigma_1\sigma_2\sigma_3} = \frac{1}{6}\varepsilon_{ijk}\varepsilon_{lmn}r_{il}r_{jm}r_{kn} \quad (\text{Eq 2.3.3})$$

where

σ_i ($i = 1, 2, 3$) are the three principal stresses

ε_{ijk} is the Levi-Civita epsilon

The directional cosines can be defined in terms of the stress invariants and the unit tensor/Kronecker Delta (δ_{ij}) as (Nakai, 1989):

$$a_1 = \sqrt{\frac{I_3}{I_2\sigma_1}}, \quad a_2 = \sqrt{\frac{I_3}{I_2\sigma_2}}, \quad a_3 = \sqrt{\frac{I_3}{I_2\sigma_3}} \quad (\text{where } a_1^2 + a_2^2 + a_3^2 = 1) \quad (\text{Eq 2.4})$$

$$a_{ij} = \sqrt{\frac{I_3}{I_2}} \cdot r_{ij}^{-1} = \sqrt{\frac{I_3}{I_2}} \cdot (\sigma_{ik} + I_{r2}\delta_{ik})(I_{r1}\sigma_{kj} + r_{r3}\delta_{kj})^{-1} \quad (\text{Eq. 2.5})$$

Nakai and Mihara (1984) defined a modified stress tensor t_{ij} by multiplying the principal stress tensor (σ_{jk}) by the directional cosine (a_{ik}), whose principal values have coordinate axes in the modified stress space:

$$t_{ij} = a_{ik}\sigma_{kj} \quad (\text{Eq. 2.6})$$

such that principal values are:

$$t_1 = a_1\sigma_1, \quad t_2 = a_2\sigma_2, \quad t_3 = a_3\sigma_3 \quad (\text{Eq. 2.7})$$

In the Cam clay model, volumetric and deviatoric strain increments ($d\varepsilon_v$ and $d\varepsilon_d$) and mean effective normal and deviator stresses (p and q) are described by the normal and in-plane components of the strain increments and principal stresses with respect to the octahedral plane. Similarly, the t_{ij} model defines modified strain increment ($d\varepsilon_N^*$ and $d\varepsilon_S^*$) and modified stresses (t_N and t_S) with respect to the SMP as normal and in-plane components of the strain increments and modified stress tensor t_{ij} , respectively. Figure 2-3 and Figure 2-4 below show these definitions in modified stress space and strain increment space. They are defined as follows (Nakai & Mihara, 1984):

$$t_N = t_1a_1 + t_2a_2 + t_3a_3 = t_{ij}a_{ij} \quad (\text{Eq 2.8})$$

$$t_S = \sqrt{(t_1 a_2 - t_2 a_1)^2 + (t_2 a_3 - t_3 a_2)^2 + (t_3 a_1 - t_1 a_3)^2} =$$

$$\sqrt{t_1^2 + t_2^2 + t_3^2 - (t_1 a_1 + t_2 a_2 + t_3 a_3)^2} = \sqrt{t_{ij} t_{ij} - (t_{ij} a_{ij})^2} \quad (\text{Eq 2.9})$$

$$d\varepsilon_N^* = d\varepsilon_1 a_1 + d\varepsilon_2 a_2 + d\varepsilon_3 a_3 = d\varepsilon_{ij} a_{ij} \quad (\text{Eq. 2.10})$$

$$d\varepsilon_S^* = \sqrt{(d\varepsilon_1 a_2 - d\varepsilon_2 a_1)^2 + (d\varepsilon_2 a_3 - d\varepsilon_3 a_2)^2 + (d\varepsilon_3 a_1 - d\varepsilon_1 a_3)^2} =$$

$$\sqrt{d\varepsilon_1^2 + d\varepsilon_2^2 + d\varepsilon_3^2 - (d\varepsilon_1 a_1 + d\varepsilon_2 a_2 + d\varepsilon_3 a_3)^2} = \sqrt{d\varepsilon_{ij} d\varepsilon_{ij} - (d\varepsilon_{ij} a_{ij})^2} \quad (\text{Eq 2.11})$$

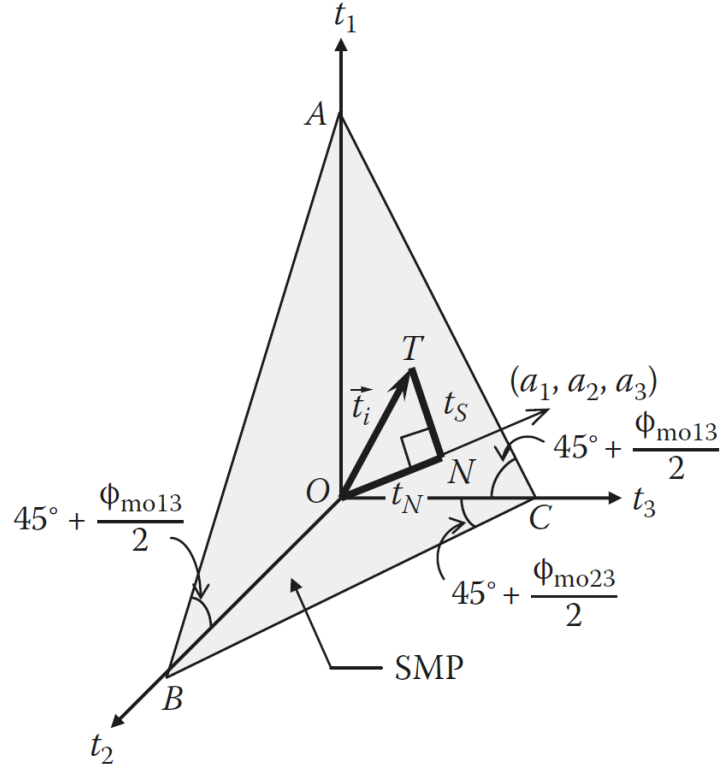


Figure 2-3 Definition of modified stress invariants (t_N and t_S) in modified stress space. (Nakai T., 2013)

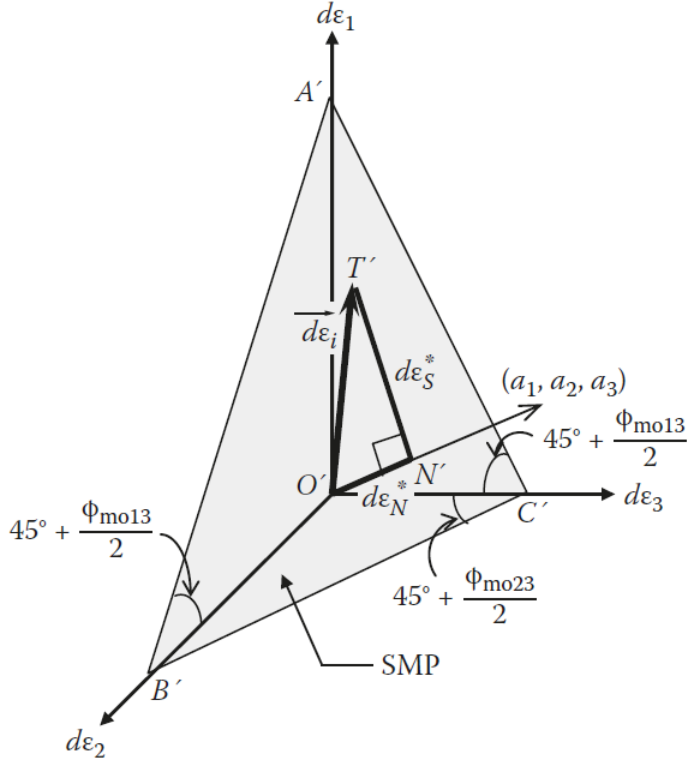


Figure 2-4 Definition of modified strain invariants ($d\epsilon_N^*$ and $d\epsilon_S^*$) in strain increment space. (Nakai T., 2013)

The modified stresses t_N and t_S are equal to normal and shear stresses (σ_{SMP} and τ_{SMP}) on the spatially mobilized plane as shown in Figure 2-3. t_N and t_S can be expressed in terms of the principal stresses and the stress invariants as follows (Matsuoka & Nakai, 1974):

$$t_N = t_1 a_1 + t_2 a_2 + t_3 a_3 = \sigma_1 a_1^2 + \sigma_2 a_2^2 + \sigma_3 a_3^2 = 3 \frac{I_3}{I_2} = \sigma_{SMP} \quad (\text{Eq. 2.12})$$

$$\begin{aligned} t_S &= \sqrt{(t_1 a_2 - t_2 a_1)^2 + (t_2 a_3 - t_3 a_2)^2 + (t_3 a_1 - t_1 a_3)^2} \\ &= \sqrt{(\sigma_1 - \sigma_2)^2 a_1^2 a_2^2 + (\sigma_2 - \sigma_3)^2 a_2^2 a_3^2 + (\sigma_3 - \sigma_1)^2 a_3^2 a_1^2} \\ &= \sqrt{\frac{I_1 I_2 I_3 - 9 I_3^2}{I_2}} = \tau_{SMP} \end{aligned} \quad (\text{Eq. 2.13})$$

$$\begin{aligned} \chi &= \frac{t_S}{t_N} = \frac{2}{3} \sqrt{\frac{(\sigma_1 - \sigma_2)^2}{4\sigma_1\sigma_2} + \frac{(\sigma_2 - \sigma_3)^2}{4\sigma_2\sigma_3} + \frac{(\sigma_3 - \sigma_1)^2}{4\sigma_3\sigma_1}} = \frac{2}{3} \sqrt{\tan \phi_{mo12}^2 + \tan \phi_{mo23}^2 + \tan \phi_{mo31}^2} \\ &= \sqrt{\frac{I_1 I_2}{9 I_3} - 1} \end{aligned} \quad (\text{Eq. 2.14})$$

In the case of the t_{ij} model, X is the stress ratio and is analogous to the Cam clay stress ratio ($\eta = q/p$). In order to define the “failure” or critical state condition, Matsuoka & Nakai’s (1974) formulation include an “SMP criterion”. To meet the criterion X must be a constant (i.e., $I_1 I_2 / I_3 = \text{constant}$). When this criterion is

met, the result is a rounded triangle in principal stress space as shown in Figure 2-5. This criterion is analogous to the Lade-Duncan criterion ($I_1^3/I_3 = \text{constant}$; Lade & Duncan, 1975), which also generates a rounded triangle in principal stress space.

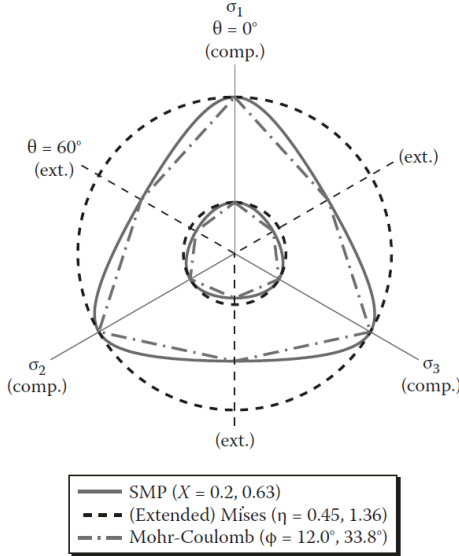


Figure 2-5 Shape of SMP criterion, Extended Von Mises criterion, and Mohr-Coulomb criterion on the octahedral plane in principal stress space (Nakai, 2013)

Table 2-1 Comparison between formulations in the traditional concept and the t_{ij} concept. (Nakai T., 2013)

	Ordinary Concept	t_{ij} Concept
Tensor normal to reference plane	δ_{ij}	a_{ij}
Stress tensor	σ_{ij}	t_{ij}
Mean stress	$p = \sigma_{ij} \delta_{ij}/3$	$t_N = t_{ij} a_{ij}$
Deviatoric stress tensor	$s_{ij} = \sigma_{ij} - p\delta_{ij}$	$t'_{ij} = t_{ij} - t_N a_{ij}$
Deviatoric stress	$q = \sqrt{(3/2)s_{ij}s_{ij}}$	$t_S = \sqrt{t'_{ij}t'_{ij}}$
Stress ratio tensor	$\eta_{ij} = s_{ij}/p$	$x_{ij} = t'_{ij}/t_N$
Stress ratio	$\eta = q/p$	$X = t_S/t_N$
Strain increment normal to reference plane	$d\varepsilon_v = d\varepsilon_{ij}\delta_{ij}$	$d\varepsilon^*_N = d\varepsilon_{ij}a_{ij}$
Deviatoric strain increment tensor	$d\varepsilon_{ij} = d\varepsilon_{ij} - d\varepsilon_v\delta_{ij}/3$	$d\varepsilon'_{ij} = d\varepsilon_{ij}a_{ij} - d\varepsilon^*_N a_{ij}$
Strain increment parallel to reference plane	$d\varepsilon_d = \sqrt{(2/3)d\varepsilon_{ij}d\varepsilon_{ij}}$	$d\varepsilon^*_S = \sqrt{d\varepsilon'_{ij}d\varepsilon'_{ij}}$

Table 2-1 compares the parameters in the traditional Cam clay model with those used by the Subloading t_{ij} model. Matsuoka & Nakai (1986) first formulated a model to describe the behavior of normally consolidated (NC) clay. The following yield function and flow rule formulated in t_{ij} space was proposed (Nakai T., 2013):

$$f = F(t_N, X = t_S/t_N) - H = 0 \quad (\text{Eq. 2.15})$$

$$d\varepsilon_{ij}^p = \Lambda \frac{\partial F}{\partial t_{ij}} \quad (\text{Eq. 2.16})$$

where

Λ is a positive proportional constant

Figure 2-6 shows the yield surface in the modified shear-normal stress (t_N and t_S) plane. In Figure 2-6, t_{N0} and t_{N1} are analogous to the preconsolidation pressures in the Cam Clay model, defining the vertex of the yield surface. The evolution of stress under elastoplastic conditions shown in Figure 2-6 is from the initial state I ($t_N = t_{N0}$) to current state P ($t_N = t_N$, $X = t_S/t_N$). Replacing the preconsolidation pressure in the Cam clay model described by Roscoe and Burland (1968) with t_{N0} and t_{N1} yields the following yield function and flow rule (Nakai T., 2013):

$$F = H \quad \text{or} \quad f = F - H = 0 \quad (\text{Eq. 2.17})$$

$$F = (\lambda - \kappa) \ln \frac{t_{N1}}{t_{N0}} = (\lambda - \kappa) \left\{ \ln \frac{t_N}{t_{N0}} + \zeta(X) \right\} \quad (\text{Eq. 2.18})$$

$$H = (-\Delta e)^p = (1 + e_0) \cdot \varepsilon_v^p \quad (\text{Eq. 2.19})$$

$$d\varepsilon_{ij}^p = \Lambda \frac{\partial F}{\partial t_{ij}} = \Lambda \left(\frac{\partial F}{\partial t_N} \frac{\partial t_N}{\partial t_{ij}} + \frac{\partial F}{\partial X} \frac{\partial X}{\partial t_{ij}} \right) \quad (\text{Eq. 2.20})$$

$$\Lambda = \frac{dF}{(1+e_0) \frac{\partial F}{\partial t_{kk}}} = \frac{dF}{h^p} \quad \left(\text{where } dF = \frac{\partial F}{\partial \sigma_{ij}} d\sigma_{ij} \right) \quad (\text{Eq. 2.21})$$

where

λ is the slope compression index

κ is the recompression index

e and e_0 are the void ratio and initial void ratio, respectively

Superscript p indicates the plastic component

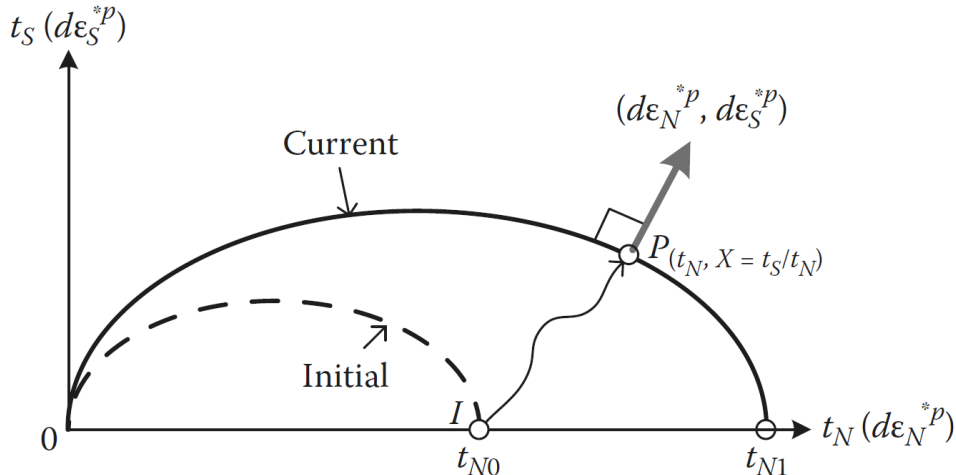


Figure 2-6 Initial and current yield surfaces in the modified shear-normal (t_N - t_S) plane and direction of plastic flow for t_{ij} model.
(Nakai T., 2013)

The plastic strain increment (Eq. 2.20) was first derived assuming an associated flow rule in t_{ij} space as seen in Figure 2-6. The proportionality constant Λ is obtained from the consistency condition ($df = 0$).

In Eq. 2.18, $\zeta(X)$ is an increasing function of the stress ratio that is analogous to the Cam clay $\zeta(\eta)$, as defined by the linear dilatancy relationship proposed by Shibata (1963). From Nakai & Matsuoka (1986) and Nakai and Hinokio (2004), $\zeta(X)$ has the following proposed form for the Subloading t_{ij} model:

$$\zeta(X) = \frac{1}{\beta} \left(\frac{X}{M^*} \right)^\beta \quad (\text{Eq. 2.22})$$

β is a shape parameter that controls the form of the yield function. When $\beta = 1$, the yield function is equivalent to the original or unmodified Cam clay model. Figure 2-7 below shows how each variable relates to the modified stress ratio X and the modified strain increment ratio Y . From Eq. 2.18, 2.20, and 2.22, the following can be derived:

$$\frac{d\varepsilon_N^{*p}}{d\varepsilon_S^{*p}} = \frac{\frac{\partial F}{\partial t_N} + \frac{\partial F}{\partial X} \frac{\partial X}{\partial t_N}}{\frac{\partial F}{\partial X} \frac{\partial X}{\partial t_S}} = \frac{1 + \zeta'(X) \cdot X}{\zeta'(X)} = \frac{(M^*)^\beta - X^\beta}{X^{\beta-1}} \quad (\text{Eq. 2.23})$$

$$\zeta'(X) = \frac{d\zeta(X)}{dX} \quad (\text{Eq. 2.24})$$

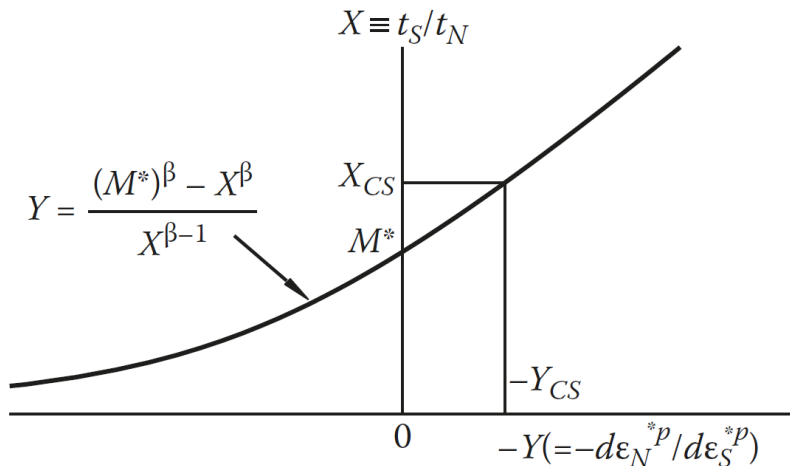


Figure 2-7 Stress-dilatancy behavior of the t_{ij} model (Nakai and Hinokio, 2004)

Figure 2-7 and Eq. 2.22, 2.23, and 2.24 represent the stress-dilatancy relationship in terms of the modified stress ratio X and the modified strain increment ratio Y as well as M^* . M^* is the vertical intercept of the relationship in Figure 2-7 and can be defined in terms of the critical state stress and strain ratios (Nakai & Mihara, 1984; Nakai & Hinokio, 2004):

$$R_{CS} = \left(\frac{\sigma_1}{\sigma_3} \right)_{CS(comp)} \quad (\text{Eq. 2.25})$$

$$X_{CS} = \frac{\sqrt{2}}{3} \left(\sqrt{R_{CS}} - \frac{1}{\sqrt{R_{CS}}} \right) \quad (\text{Eq. 2.26})$$

$$\gamma_{cs} = \frac{1+\sqrt{R_{cs}}}{\sqrt{2}(\sqrt{R_{cs}}+0.5)} \quad (\text{Eq. 2.27})$$

$$M^* = \left(X_{cs}^\beta + X_{cs}^{\beta-1} \gamma_{cs} \right)^{1/\beta} \quad (\text{Eq. 2.28})$$

Eq. 2.26 and 2.27 are derived from Eq. 2.8 through 2.11 by assuming triaxial compression conditions ($\sigma_2 = \sigma_3$). Elastic strains are expressed through a generalized Hooke's law. As opposed to the Cam clay model where the mean stress p governs the elastic volumetric strain, the t_{ij} model utilizes the mean modified stress t_N to dictate the elastic volumetric strain. The relationship is as follows (Nakai T., 2013):

$$d\varepsilon_{ij}^e = \frac{1+\nu_e}{E_e} d \left(\frac{\sigma_{ij}}{1+X^2} \right) - \frac{\nu_e}{E_e} d \left(\frac{\sigma_{mm}}{1+X^2} \right) \delta_{ij} \quad (\text{Eq. 2.29})$$

$$E_e = \frac{3(1-2\nu_e)(1+e_0)t_N}{\kappa} \quad (\text{Eq. 2.30})$$

$$t_N = \frac{p}{1+X^2} \quad (\text{Eq. 2.31})$$

To define the plastic strain increment in Eq. 2.20 requires partial derivatives of F with respect to the modified stress t_{ij} and the ordinary stress σ_{ij} . Additional partial derivatives of the modified normal stress t_N , the modified stress ratio X , the modified stress ratio tensor x_{ij} , and the stress invariants are also required. Nakai (2013) indicates that these partial derivatives are sufficient to express any isotropic hardening model in the t_{ij} stress space. The partial derivatives are as follows (Nakai T., 2013):

$$\frac{\partial F}{\partial t_{ij}} = \frac{\partial F}{\partial t_N} \frac{\partial t_N}{\partial t_{ij}} + \frac{\partial F}{\partial X} \frac{\partial X}{\partial t_{ij}} \quad (\text{Eq. 2.32})$$

$$\frac{\partial F}{\partial t_N} = (\lambda - \kappa) \frac{1}{t_N} \quad (\text{Eq. 2.33})$$

$$\frac{\partial t_N}{\partial t_{ij}} = \frac{\partial(t_{kl}a_{kl})}{\partial t_{ij}} = a_{ij} \quad (\text{Eq. 2.34})$$

$$\frac{\partial F}{\partial X} = (\lambda - \kappa) \zeta'(X) \quad (\text{Eq. 2.35})$$

$$\frac{\partial X}{\partial t_{ij}} = \frac{\partial(\sqrt{x_{mn}x_{mn}})}{\partial x_{kl}} \frac{\partial x_{kl}}{\partial t_{ij}} = \frac{1}{X \cdot t_N} (x_{ij} - X^2 a_{ij}) \quad (\text{Eq. 2.36})$$

where

$$x_{ij} = \frac{t'_{ij}}{t_N} = \frac{t_{ij} - t_N a_{ij}}{t_N} = \frac{t_{ij}}{t_N} - a_{ij} \quad (\text{Eq. 2.37, Table 2-1})$$

$$\frac{\partial X}{\partial x_{kl}} = \frac{\partial(\sqrt{x_{mn}x_{mn}})}{\partial x_{kl}} = \frac{x_{kl}}{X} \quad (\text{Eq. 2.38})$$

$$\frac{\partial x_{kl}}{\partial t_{ij}} = \frac{\partial}{\partial t_{ij}} \left(\frac{t_{kl}}{t_N} - a_{kl} \right) = \frac{1}{t_N} \{ \delta_{ik} \delta_{jl} - (x_{kl} + a_{kl}) a_{ij} \} \quad (\text{Eq. 2.39})$$

Partial derivatives of F with respect to σ_{ij} are shown below (Nakai, 2013):

$$\frac{\partial F}{\partial \sigma_{ij}} = \frac{\partial F}{\partial t_N} \frac{\partial t_N}{\partial \sigma_{ij}} + \frac{\partial F}{\partial X} \frac{\partial X}{\partial \sigma_{ij}} \quad (\text{Eq. 2.40})$$

$$\frac{\partial t_N}{\partial \sigma_{ij}} = \frac{\partial}{\partial \sigma_{ij}} \left(3 \frac{I_3}{I_2} \right) = -3 \frac{I_3}{I_2^2} \frac{\partial I_2}{\partial \sigma_{ij}} + 3 \frac{1}{I_2} \frac{\partial I_3}{\partial \sigma_{ij}} \quad (\text{Eq. 2.41})$$

$$\frac{\partial X}{\partial \sigma_{ij}} = \frac{\partial}{\partial \sigma_{ij}} \left(\sqrt{\frac{I_1 I_2}{9I_3} - 1} \right) = \frac{1}{2X} \left(\frac{I_2}{9I_3} \frac{\partial I_1}{\partial \sigma_{ij}} + \frac{I_1}{9I_3} \frac{\partial I_2}{\partial \sigma_{ij}} - \frac{I_1 I_2}{9I_3^2} \frac{\partial I_3}{\partial \sigma_{ij}} \right) \quad (\text{Eq. 2.42})$$

where

$$\frac{\partial I_1}{\partial \sigma_{ij}} = \frac{\partial \sigma_{kk}}{\partial \sigma_{ij}} = \delta_{ij} \quad (\text{Eq. 2.43})$$

$$\frac{\partial I_2}{\partial \sigma_{ij}} = \frac{\partial}{\partial \sigma_{ij}} \left(\frac{(\sigma_{kk})^2 - \sigma_{lm}\sigma_{ml}}{2} \right) = \sigma_{kk} \delta_{ij} - \sigma_{ij} \quad (\text{Eq. 2.44})$$

$$\frac{\partial I_3}{\partial \sigma_{ij}} = \frac{\partial}{\partial \sigma_{ij}} \left(\frac{e_{klm} e_{opq} \sigma_{ko} \sigma_{lp} \sigma_{mq}}{6} \right) = \frac{1}{2} e_{ilm} e_{jpq} \sigma_{lp} \sigma_{mq} \quad (\text{Eq. 2.45})$$

The above is described by Nakai (2013) to be roughly identical to his earlier “wet clay” model (Nakai & Matsuoka, 1986). Nakai (2013) indicates that the model still brings several of the limitations of the traditional Cam clay model along with it. Strain behavior is elastic when the stress state lies below the yield surface. When the stress state lies above the yield surface, superimposed elastic/plastic behavior occurs. To account for material behavior not described by the “wet clay” model (e.g., overconsolidation, granular behavior, etc.), several additions are proposed by Nakai (2013). Nakai (2013) first adopts the Hashiguchi (1989) subloading surface. The subloading surface accounts for the behavior of overconsolidated soil. The subloading surface can allow the model to realistically reproduce stress history (Nakai et al., 2011) by creating a smooth transition from the recompression to the normally consolidated line.

For an NC soil, and as shown in Eq. 2.18, the plastic change in void ratio upon application of a change in stress can be expressed as:

$$(-\Delta e)_N^p = (e_{N0} - e_N) - (-\Delta e)^e = (-\Delta e)_{NC} - (-\Delta e)^e = (\lambda - \kappa) \ln \frac{t_{N1}}{t_{N0}} \quad (\text{Eq. 2.46})$$

As shown in Figure 2-8, when an overconsolidated soil at an initial state (e_0, t_{N0}) at Point I undergoes a stress change to Point P (e, t_{N1}) that is not on the normally consolidated line, there is a corresponding offset (ρ_0) from the normally consolidated line. These offsets have been described as the influence of density by Nakai et al. (2011) but is typically thought of as the recompression curve. From Figure 2-8, it follows that:

$$\rho = e_N - e \quad (\text{Eq. 2.47})$$

$$(-\Delta e)^p = (-\Delta e)_{NC}^p - (\rho_0 - \rho) = (\lambda - \kappa) \ln \frac{t_{N1}}{t_{N0}} - (\rho_0 - \rho) \quad (\text{Eq. 2.48})$$

It further follows from Eq. 2.17 that:

$$F + \rho = H + \rho_0 \quad \text{or} \quad f = F - \{H + (\rho_0 - \rho)\} = 0 \quad (\text{Eq. 2.49})$$

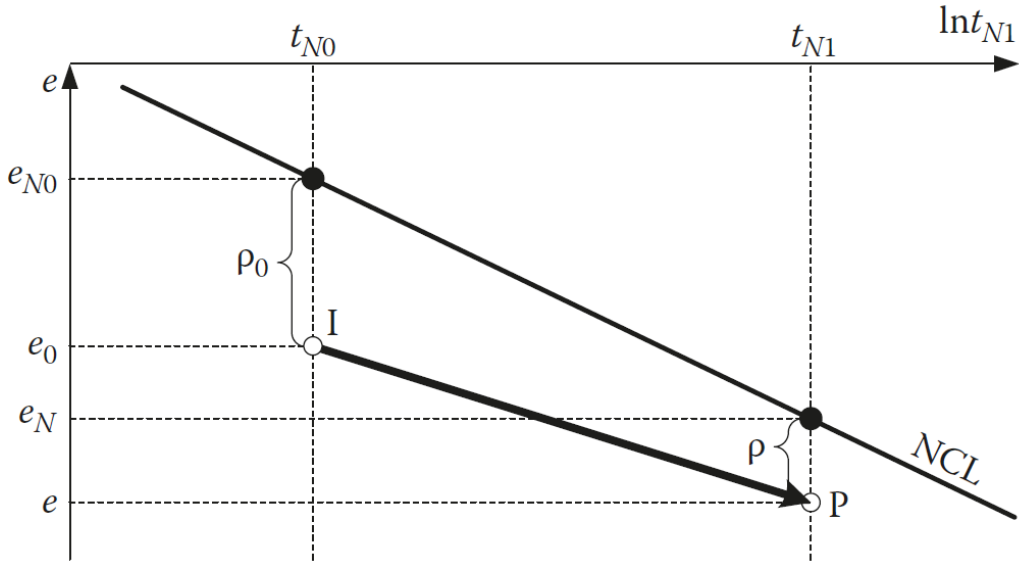


Figure 2-8 Change in void ratio on an e - $\ln t_{Np}$ plot. (Nakai T., 2013)

With the consistency condition ($df = 0$) and the plastic flow rule in Eq. 2.20, Eq. 2.49 can be restated as:

$$\begin{aligned} df &= dF - \{dH - d\rho\} = dF - \{d(-e)^p - d\rho\} \\ &= dF - \left\{ (1 + e_0) \Lambda \frac{\partial F}{\partial t_{ij}} - d\rho \right\} = 0 \quad (\text{Eq. 2.50}) \end{aligned}$$

In this model, ρ is a positive decreasing value that is zero during plastic straining or virgin compression. To dimensionally satisfy Eq. 2.50, the evolution rule for ρ is expressed using a monotonically increasing function $G(\rho)$ that satisfies $G(0) = 0$ (Nakai et al., 2011):

$$d\rho = -(1 + e_0) \frac{G(\rho)}{t_N} \Lambda \quad (\text{Eq. 2.51})$$

There are several existing options for $G(\rho)$ that satisfy the requisite conditions. However, under specific conditions, ρ can become negative. Structured clays and cemented soils can produce negative ρ values, becoming less stiff with increased debonding demonstrating brittle and compressive behavior. To ensure that $G(\rho)$ is an increasing function that satisfies all necessary conditions, Nakai et. al (2011) proposes:

$$G(\rho) = \text{sign}(\rho) a \rho^2 \quad (\text{Eq. 2.52})$$

Substituting Eq. 2.51 into Eq. 2.50:

$$\Lambda = \frac{dF}{(1+e_0) \left(\frac{\partial F}{\partial t_{ij}} + \frac{G(\rho)}{t_N} \right)} = \frac{dF}{h^p} \quad \left(\text{where } dF = \frac{\partial F}{\partial \sigma_{kl}} d\sigma_{kl} \right) \quad (\text{Eq. 2.53})$$

When considering a subloading surface, the soil at the current stress is assumed to be “passing over” the subloading surface regardless of whether plastic deformation occurs or not (Hashiguchi, 1989). In this model, the plastic strain increment is non-zero when $\Lambda > 0$ and is 0 otherwise:

$$\begin{cases} d\varepsilon_{ij}^p \neq 0 & \text{if } \Lambda = \frac{dF}{h^p} > 0 \\ d\varepsilon_{ij}^p = 0 & \text{otherwise} \end{cases} \quad (\text{Eq. 2.54})$$

$$d\varepsilon_{ij}^p = \langle \Lambda \rangle \frac{\partial F}{\partial t_{ij}} = \langle \frac{dF}{h^p} \rangle \frac{\partial F}{\partial t_{ij}} \quad (\text{where } dF = \frac{\partial F}{\partial \sigma_{kl}} d\sigma_{kl}) \quad (\text{Eq. 2.55})$$

where

$\langle \rangle$ are Macaulay brackets

The total strain $d\varepsilon_{ij} = d\varepsilon_{ij}^e + d\varepsilon_{ij}^p$, with the elastic strain component calculated using Eq. 2.29.

Nakai (2013) points out that this model utilizes classical plasticity theory, where the direction of plastic flow is independent of the direction of the stress increments. The result is a stress-dilatancy relationship that is not affected by the stress path. However, Tatsuoka (1980) and El-Sohby (1969) have demonstrated that inherent anisotropy in the soil can cause stress-dilatancy to depend on the stress path except when at or near failure. Nakai (2013) argues that stress path dependency of stress-dilatancy relationships is controlled by the intermediate principal stress which is automatically accounted for when using t_{ij} (except at or near peak strength) and presents Figure 2-9 as demonstratory evidence.

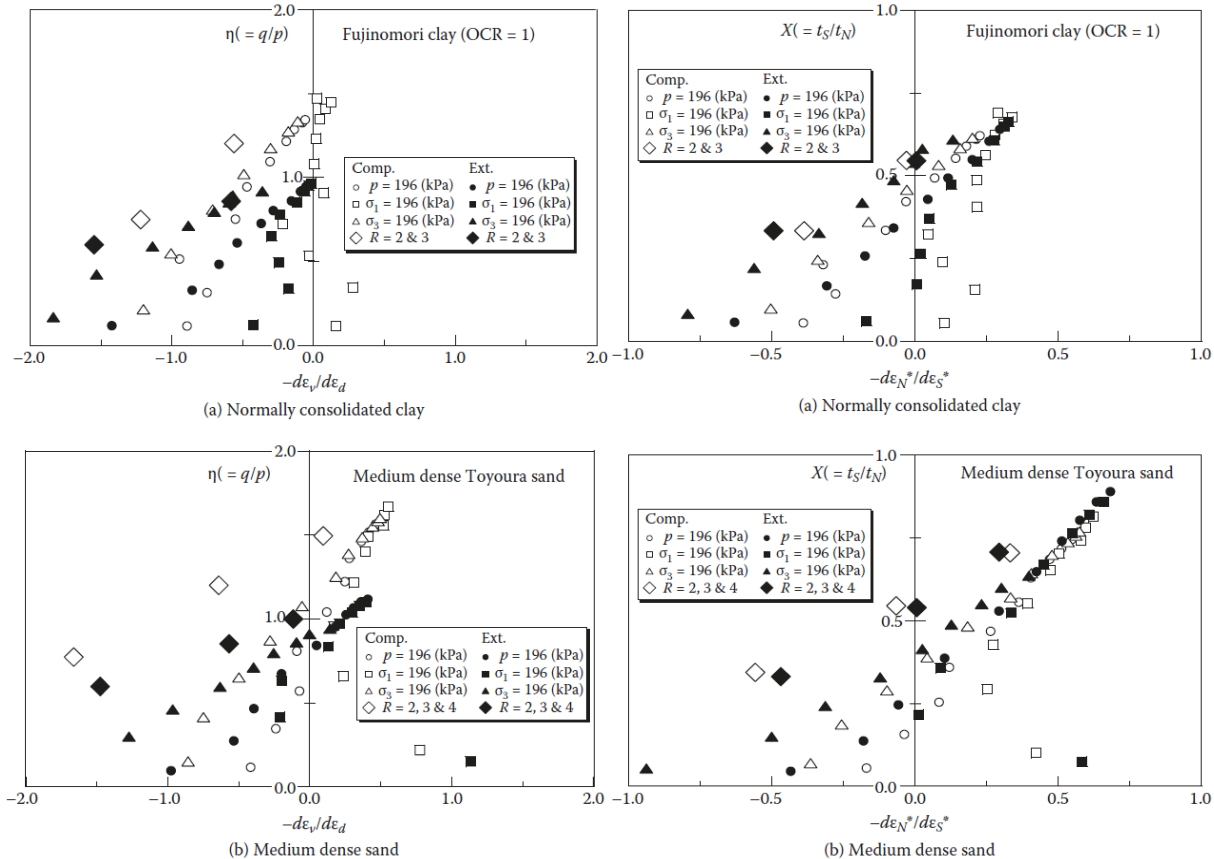


Figure 2-9 Observed stress-dilatancy relationship under different stress paths; Left: in terms of q/p and $-d\varepsilon_v/d\varepsilon_d$; Right: in terms of $X(t_S/t_N)$ and $-d\varepsilon_N^*/d\varepsilon_S^*$. (Nakai T., 2013)

Nakai (2013) further defines the stress-dilatancy relationship for the t_{ij} model by separating the plastic strain increment into two components: a plastic strain increment $d\varepsilon_{ij}^{p(AF)}$, satisfying the associated

flow rule in t_{ij} space, and an isotropic compression plastic strain increment $d\varepsilon_{ij}^{p(IC)}$, under increasing t_N . Figure 2-10 shows the current yield surface as a solid line and a subsequent yield surface as a dotted line. The current stress point A lies on the current yield surface with two possible subsequent stress states, B and C. When the stress state moves to point B in region II ($dF > 0$ and $dt_N \leq 0$), the plastic strain increment is described by only an associated flow component ($d\varepsilon_{ij}^{p(AF)}$) as given by Eq. 2.55. When the stress state moves to point C in region III ($dF > 0$ and $dt_N > 0$), the plastic strain is assumed to be composed of an associated flow component ($d\varepsilon_{ij}^{p(AF)}$) and an isotropic compression component ($d\varepsilon_{ij}^{p(IC)}$). From Eq. 2.53 and Eq. 2.55, isotropic compression plastic volumetric strain is given by:

$$d\varepsilon_v^p = d\varepsilon_{ii}^p = \Lambda \frac{\partial F}{\partial t_{ii}} = \frac{dF}{(1+e_0)\left(\frac{\partial F}{\partial t_{kk}} + \frac{G(\rho)}{t_N}\right)} \cdot \frac{\partial F}{\partial t_{ii}} \quad (\text{Eq. 2.56})$$

Given $X = 0$ during isotropic compression:

$$t_{N1} = t_N = p \quad (\text{Eq. 2.57})$$

$$\frac{\partial F}{\partial t_{ii}} = \frac{\lambda - \kappa}{t_N} a_{ii} \quad (\text{Eq. 2.58})$$

$$d\varepsilon_v^p = \frac{\lambda - \kappa}{(1+e_0)\left(1 + \frac{G(\rho)}{(\lambda - \kappa)a_{ii}}\right)} \cdot \frac{dt_N}{t_N} \quad (\text{Eq. 2.59})$$

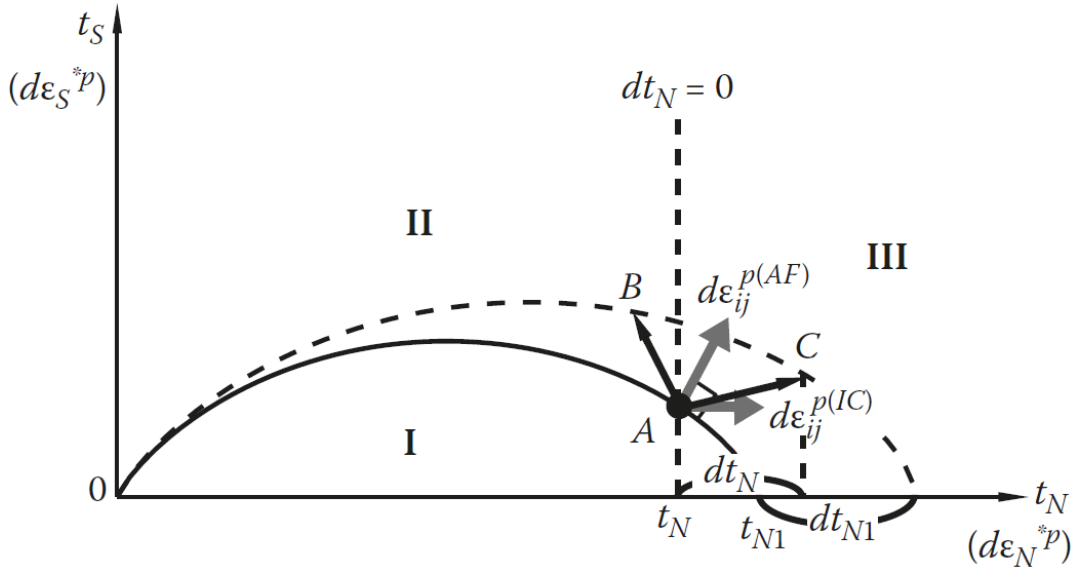


Figure 2-10 Plastic strain increments $d\varepsilon_{ij}^{p(AF)}$ and $d\varepsilon_{ij}^{p(IC)}$, shown on the modified shear-normal plane (Nakai T., 2013)

The isotropic compression plastic volumetric strain increment ($d\varepsilon_{ij}^{p(IC)}$) in general stress conditions ($dt_N > 0$), is taken as a fraction t_N/t_{N1} of the plastic volumetric strain as described in Eq. 2.59. This formulation is based on the “wet clay” t_{ij} model proposed earlier by Nakai and Matsuoka (1986). The result is:

$$d\varepsilon_{ij}^{p(IC)} = \Lambda^{(IC)} \frac{\delta_{ij}}{3} = \frac{\lambda - \kappa}{(1+e_0)\left(1 + \frac{G(\rho)}{(\lambda - \kappa)a_{ii}}\right)} \cdot \frac{\langle dt_N \rangle}{t_N} \cdot \frac{t_N}{t_{N1}} \cdot \frac{\delta_{ij}}{3}$$

$$= \frac{\frac{\lambda-\kappa}{t_{N1}} \langle dt_N \rangle}{(1+e_0) \left(1 + \frac{G(\rho)}{(\lambda-\kappa)a_{ii}} \right)} \cdot \frac{\delta_{ij}}{3} = \frac{\frac{\lambda-\kappa}{t_{N1}} \langle dt_N \rangle}{h^{p(IC)}} \cdot \frac{\delta_{ij}}{3} \quad (\text{Eq. 2.60})$$

where $\langle \rangle$ are Macaulay brackets

From Eq. 2.18 and Eq. 2.22 we have:

$$t_{N1} = t_N \cdot \exp(\zeta(X)) = t_N \cdot \exp\left(\frac{1}{\beta} \left(\frac{\chi}{M^*}\right)^\beta\right) \quad (\text{Eq. 2.61})$$

To derive similar parameters for the associated flow component, Nakai (2013) first considered the normally consolidated case ($\rho = 0$). Taking the two strain components into consideration as well as the consistency condition ($df = 0$), the following can be stated:

$$\begin{aligned} df = dH = d(-e)^p &= (1 + e_0) \left(d\varepsilon_v^{p(AF)} + d\varepsilon_v^{p(IC)} \right) \\ &= (1 + e_0) \left(\Lambda_{(\rho=0)}^{(AF)} \frac{\partial F}{\partial t_{ii}} + \frac{\lambda-\kappa}{1+e_0} \frac{1}{t_{N1}} \langle dt_N \rangle \right) \end{aligned} \quad (\text{Eq. 2.62})$$

$$\Lambda_{(\rho=0)}^{(AF)} = \frac{dF - \frac{\lambda-\kappa}{t_{N1}} \langle dt_N \rangle}{(1+e_0) \frac{\partial F}{\partial t_{kk}}} \quad (\text{Eq. 2.63})$$

This yields the proportionally constant $\Lambda_{(\rho=0)}^{(AF)}$ of $d\varepsilon_{ij}^{p(AF)}$ at normally consolidated states. To derive $d\varepsilon_{ij}^{p(AF)}$ under the overconsolidated state, $\Lambda^{(AF)}$ will reduce to $\Lambda_{(NC)}^{(AF)}$ when normally consolidated ($\rho = 0$). Referring to Eq. 2.53, Eq. 2.55, and Eq. 2.63, the following results:

$$\begin{aligned} d\varepsilon_{ij}^{p(AF)} &= \Lambda^{(AF)} \frac{\partial F}{\partial t_{ij}} = \frac{dF - \frac{\lambda-\kappa}{t_{N1}} \langle dt_N \rangle}{(1+e_0) \left(\frac{\partial F}{\partial t_{kk}} + \frac{G(\rho)}{t_N} \right)} \cdot \frac{\partial F}{\partial t_{ij}} \\ &= \frac{dF - \frac{\lambda-\kappa}{t_{N1}} \langle dt_N \rangle}{h^p} \cdot \frac{\partial F}{\partial t_{ij}} \quad \left(\text{where } dF = \frac{\partial F}{\partial \sigma_{mn}} d\sigma_{mn} \right) \end{aligned} \quad (\text{Eq. 2.64})$$

The t_{ij} model can be summarized for Regions I, II, and III from Figure 2-10 as (Nakai T. , 2013):

- Elastic Region I ($dF = \frac{\partial F}{\partial \sigma_{mn}} d\sigma_{mn} < 0$):

$$\begin{aligned} d\varepsilon_{ij} &= d\varepsilon_{ij}^e \\ &= \frac{1+\nu_e}{E_e} d\sigma_{ij} - \frac{\nu_e}{E_e} d\sigma_{mm} \delta_{ij} \end{aligned} \quad (\text{Eq. 2.65})$$

- Elastoplastic Region II with strain hardening ($dF = \frac{\partial F}{\partial \sigma_{mn}} d\sigma_{mn} > 0 \quad \& \quad h^p > 0$):

$$\begin{aligned} d\varepsilon_{ij} &= d\varepsilon_{ij}^e + d\varepsilon_{ij}^{p(AF)} + d\varepsilon_{ij}^{p(IC)} \\ &= \frac{1+\nu_e}{E_e} d\sigma_{ij} - \frac{\nu_e}{E_e} d\sigma_{kk} \delta_{ij} + \frac{dF - \frac{\lambda-\kappa}{t_{N1}} \langle dt_N \rangle}{(1+e_0) \left(\frac{\partial F}{\partial t_{mm}} + \frac{G(\rho)}{t_N} \right)} \cdot \frac{\partial F}{\partial t_{ij}} + \frac{\frac{\lambda-\kappa}{t_{N1}} \langle dt_N \rangle}{(1+e_0) \left(1 + \frac{G(\rho)}{(\lambda-\kappa)a_{kk}} \right)} \cdot \frac{\delta_{ij}}{3} \end{aligned} \quad (\text{Eq. 2.66})$$

3. Elastoplastic Region III with strain softening ($dF = \frac{\partial F}{\partial \sigma_{mn}} d\sigma_{mn} > 0$ & $h^p < 0$):

$$\begin{aligned} d\varepsilon_{ij} &= d\varepsilon_{ij}^e + d\varepsilon_{ij}^p \\ &= \frac{1+\nu_e}{E_e} d\sigma_{ij} - \frac{\nu_e}{E_e} d\sigma_{kk} \delta_{ij} + \frac{dF}{(1+e_0) \left(\frac{\partial F}{\partial t_{mm}} + \frac{G(\rho)}{t_N} \right)} \cdot \frac{\partial F}{\partial t_{ij}} \end{aligned} \quad (\text{Eq. 2.67})$$

This model can be refined to account for several more facets of soil behavior; structured behavior, time-dependent behavior, unsaturated behavior, and temperature-dependent behavior. These further refined versions of the model accounting for additional aspects of soil behavior are available in the literature (Nakai T., 2013; Nakai and Shahin, 2013). The more complex versions of the t_{ij} model are not included here as those behaviors are not anticipated to have a significant impact on the simulation conducted herein.

Several of the parameters employed in the subloading t_{ij} model, such as λ and κ , are also employed in the Cam clay model (Roscoe & Burland, 1968). These parameters can be derived from isotropic consolidation tests. One unique parameter utilized by the subloading t_{ij} model is R_{cs} which is defined by Eq. 2.25 but can also be expressed as:

$$R_{cs} = \frac{2M+3}{3-M} \quad (\text{Eq. 2.68})$$

Only two parameters utilized by the subloading t_{ij} model are “fitting parameters” and require direct iteration. The α density parameter and β yield function shape parameters both require iteration to obtain best-fits. Optimization of these parameters is discussed further in both Section 2.4 and Section 4.1.3 below.

2.2 Finite Element Method

Ubiquitous numerical modeling methodologies include the finite element (FE) and finite difference methods. Both methodologies require discretization of geometries into “finite” subdivisions to approximate the continuum. Numerical modeling problems assume values at the domain boundaries to constrain the problem, allowing the governing differential equation to be solved. Problems are either time-dependent (as in the case of transient flow problems) or time-independent (as in the case of plastic deformation problems) and require analogous boundary conditions.

FE discretization generates a mesh consisting of tangential elements composed of node points and boundary lines. The cardinality of the elements is defined based on the dimensionality of the problem, but elements generally organize first to form local meshes and then global meshes. When performing three-dimensional FE analysis, boundary lines and nodes combine to form volume elements. There are two primary 3D element shapes, quadrilateral and triangular.

FE can be utilized to simulate a wide range of engineering structures. This study involves utilizing FE to solve a stress-deformation problem. The stress-strain behavior of each material in the model is governed by a constitutive model. Constitutive models range from simple linear elastic (Hooke’s law) to linear elastoplastic (Mohr-Coulomb theory) to more sophisticated non-linear elastoplastic models. The Subloading t_{ij} model is chosen to represent the soil in this study because it is theoretically sound, elegant with being overly complex, and has sufficient stability that solutions are easily attainable. The general procedure can be summarized as:

1. Discretization of geometry and selecting element type and configuration
2. Choose coordinate shape function that maps element displacement to nodal displacement
3. Define constitutive relationship
4. Derive elemental equations based on shape function and constitutive relationship
5. Develop a global equation based on individual elemental equations
6. Solve the global equation after applying boundary conditions
7. Compute secondary quantities
8. Interpret results

In modeling soil-structure interaction, interface elements are used to allow slippage to occur between the soil and structure. Interface elements are solid elements that provide transition between materials but have effectively zero thickness. Interface elements are primarily defined by a normal and shear stiffness (Desai et al., 1984). The constitutive behavior of interface elements is typically defined by a simple elastoplastic model (Mohr-Coulomb). In this study, interface elements are used to describe the behavior of geosynthetic-soil interaction,

2.3 Numerical Modeling of GRS Mini-Piers

Kaya (2016) and Shen et al. (2019) both performed numerical studies of the FHWA mini-pier load tests (Nicks et al., 2013). Kaya (2016) modeled the mini piers assuming plane strain conditions as a robust 3D software incorporating the Subloading t_{ij} model was not available at that time. The result was that Kaya (2016) achieved very limited agreement between modeling results and load test data, achieving the best agreement between test results and modeling of an unfaced mini pier. Shen et al. (2019) achieved much better agreement between modeling and test results however only conducted modeling of faced mini piers.

Kaya (2016) analyzed the load testing of mini-piers TF-6 (faced) and TF-7 (unfaced). He also utilized the Subloading t_{ij} constitutive model to simulate the granular fill material, using the model-specific FE software, FEMtij-2D. Kaya (2016) additionally attempted to perform a three-dimensional FE analysis using FEMtij-3D but the analysis did not produce reasonable results. His study included a parametric study of three primary factors: soil-facing interface friction angle, facing constitutive model, and geosynthetic constitutive model. The following conditions were assumed during the parametric study:

1. Two soil-facing interface friction angles, δ , were investigated as δ was assumed to be between 0° and the granular fill friction angle, ϕ :
 - a. Frictionless or 0°
 - b. 33° or approximately $2/3$ of ϕ , i.e. assuming a “smooth” concrete interface
2. Facing is modeled using
 - a. A linear elastic model
 - b. Mohr-Coulomb theory
 - c. Drucker-Prager yield criterion
3. The geosynthetic is modeled using
 - a. A linear elastic model
 - b. A linear elastic model with post-yield softening

Figure 2-11 and Figure 2-12 contain the parametric study results of the soil-facing interface angle. Figure 2-13 and Figure 2-14 contain the results of different facing constitutive models. Finally, Figure 2-15 and Figure 2-16 are the results of different geosynthetic constitutive models. As seen from Figure 2-12, Figure 2-14, and Figure 2-16, the FE model produced by Kaya (2016) generally displays stiff vertical behavior; resulting in overestimation of lateral displacements.

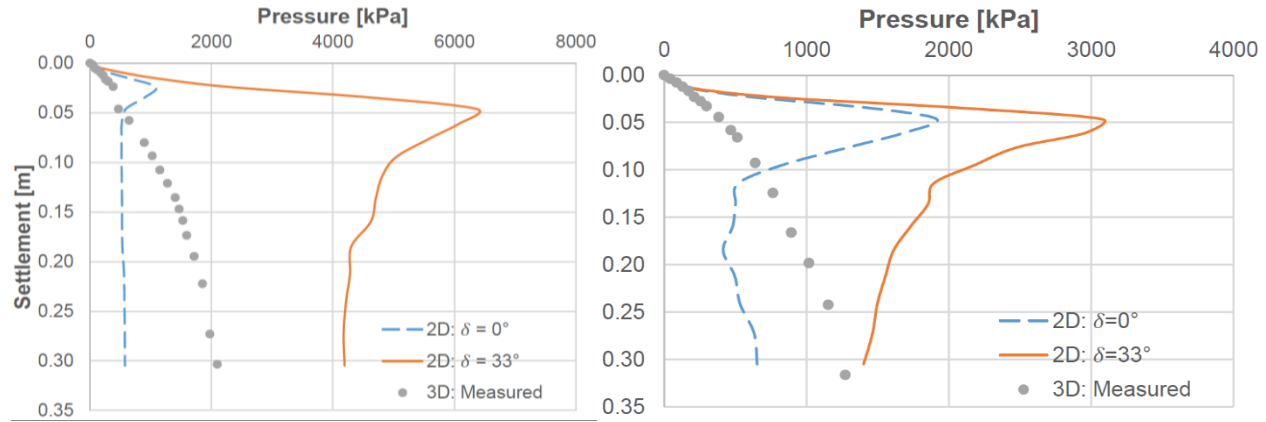


Figure 2-11 The effect of soil-facing friction angle on the load-settlement curve of TF-6 (left) and TF-7 (right). (Kaya, 2016)

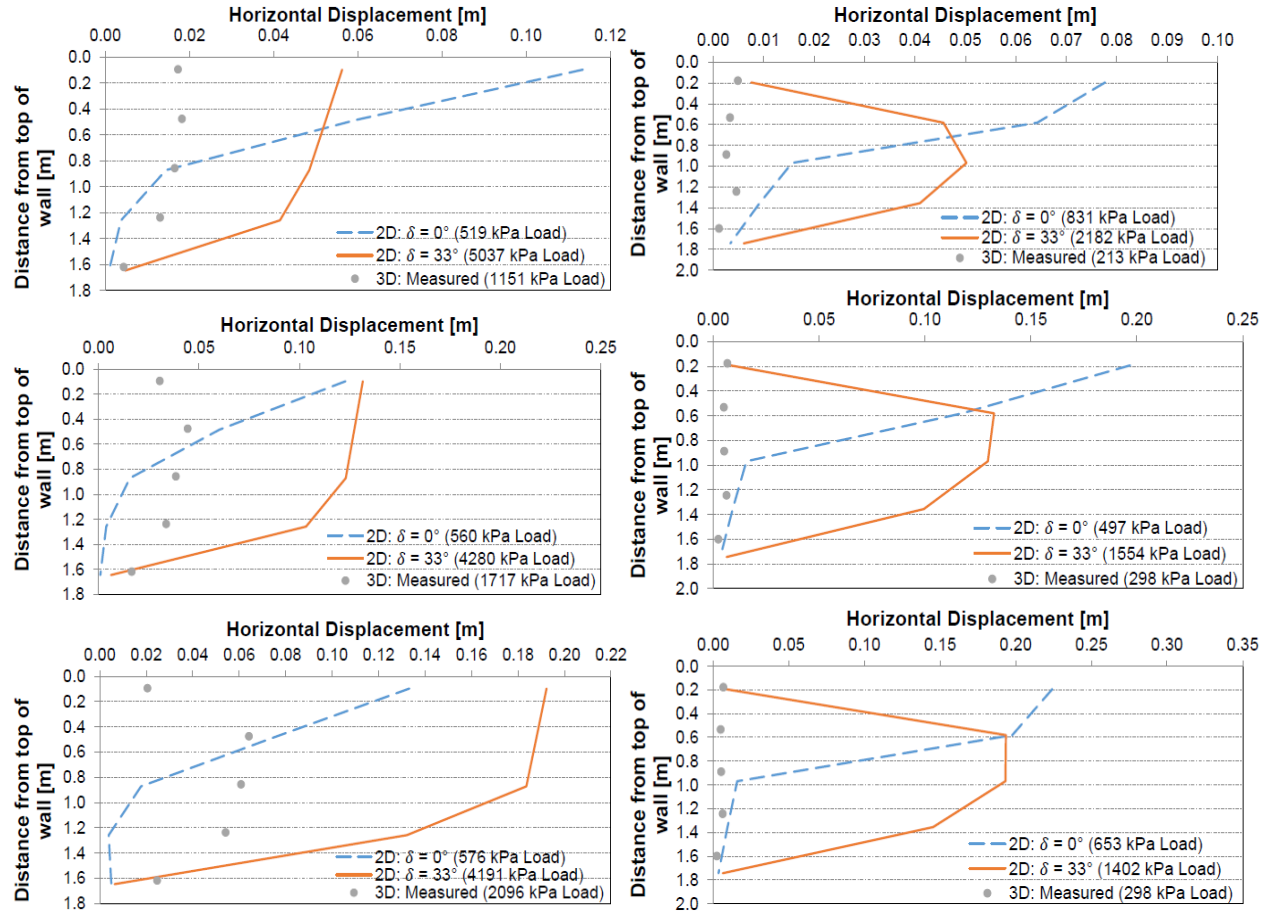


Figure 2-12 The effect of soil-facing friction angle on the lateral displacement of TF-6 (left) and TF-7 (right) at 4, 8, and 12 inches of settlement. (Kaya, 2016)

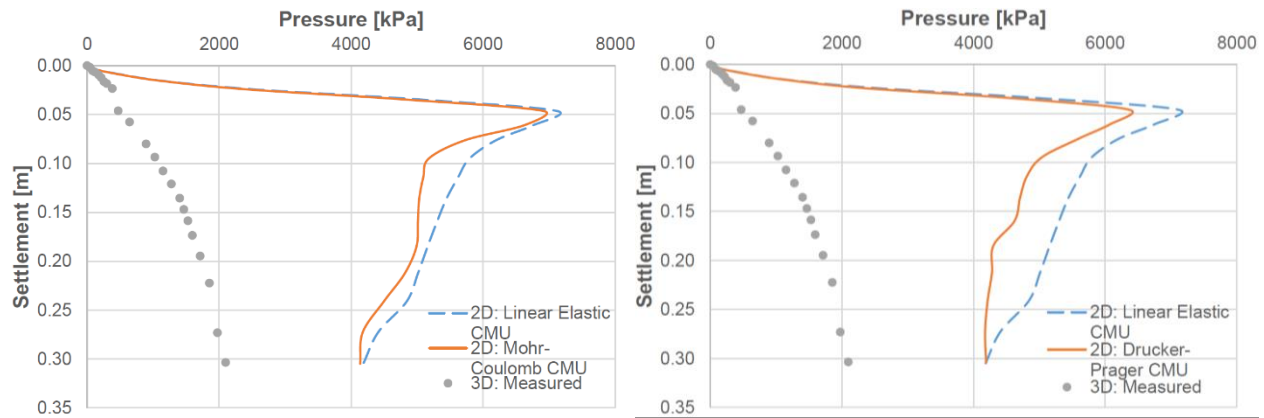


Figure 2-13 The effect of the facing's constitutive model on the TF-6 load-settlement curve. (Kaya,2016)

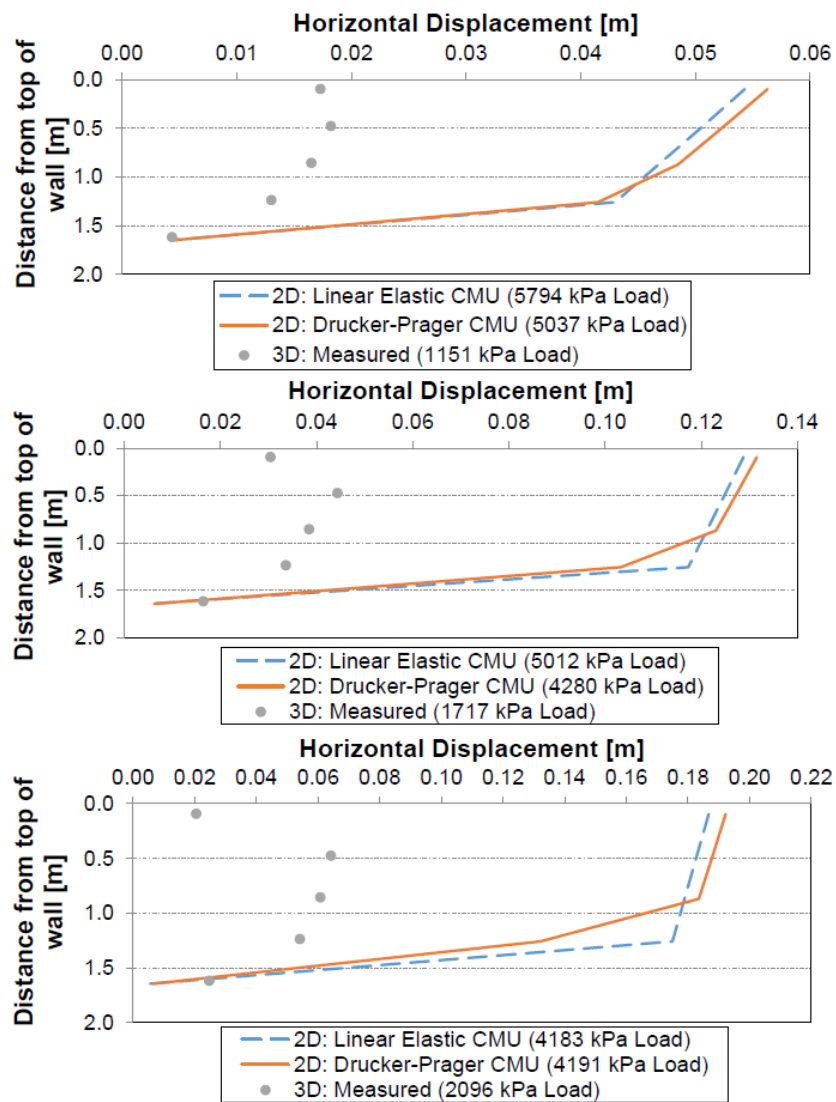


Figure 2-14 The effect of the facing's constitutive model on lateral displacement of TF-6 at 4, 8, and 12 inches of settlement. (Kaya, 2016)

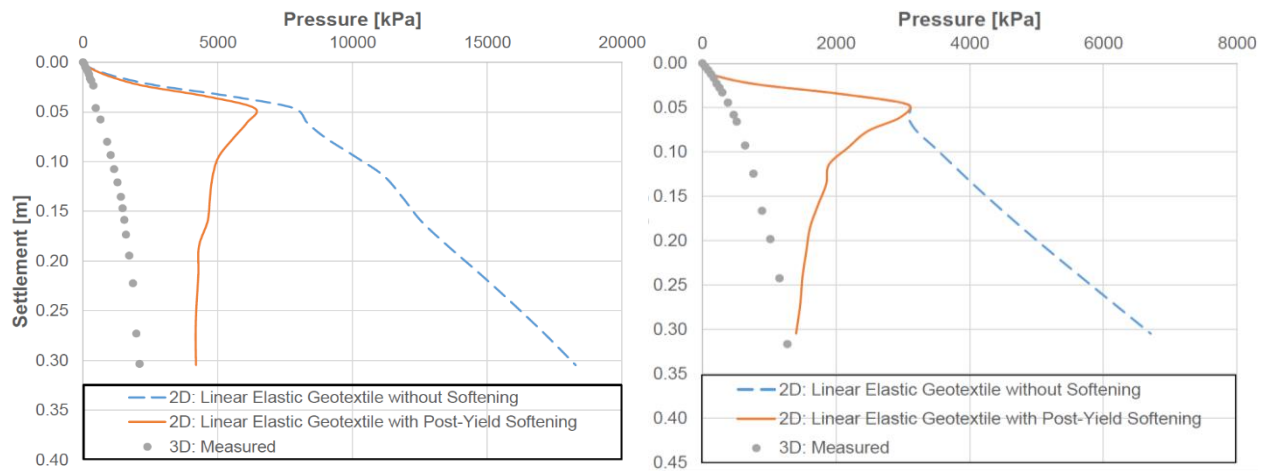


Figure 2-15 The effect of geosynthetic constitutive model on the load-settlement curve of TF-6 (left) and TF-7 (right). (Kaya, 2016)

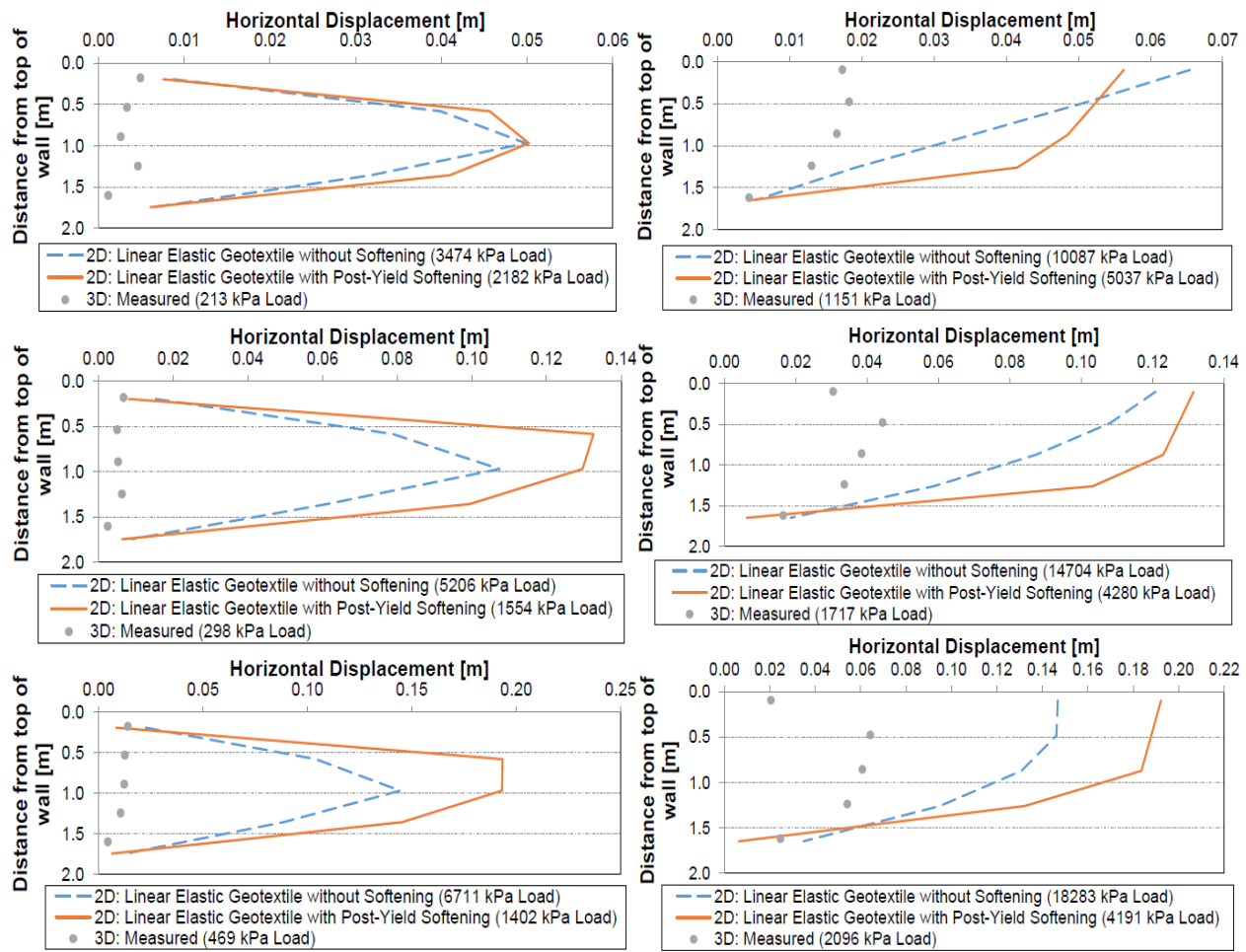


Figure 2-16 The effect of the geosynthetic constitutive model on lateral displacement of TF-6(right) and TF-7(left) at 4, 8, and 12 inches of settlement. (Kaya, 2016)

To generate model parameters, Kaya (2016) first analyzed an isotropic consolidation test and four consolidated-drained triaxial tests provided by FHWA. This testing regime was performed in addition to the testing reported in Nicks et al. (2013) as part of the load testing conducted by the FHWA. Kaya (2016) derived consolidation parameters using the isotropic consolidation test results while the remaining parameters were derived using the triaxial test results. Kaya (2016) performed a best-fit analysis by investigating the effects of varying two parameters: the density parameter a , and the yield function shape parameter β . The best fit analysis was performed on the triaxial test data using the element simulation software “Subloading_Tij.exe”. Kaya (2016) indicated that one of the triaxial tests failed to reach critical state. Kaya (2016) concluded that the triaxial test performed at a confining stress (σ_3) of 20 psi (138 kPa) should be excluded. Figure 2-17 below shows the result of Kaya’s best-fit analysis.

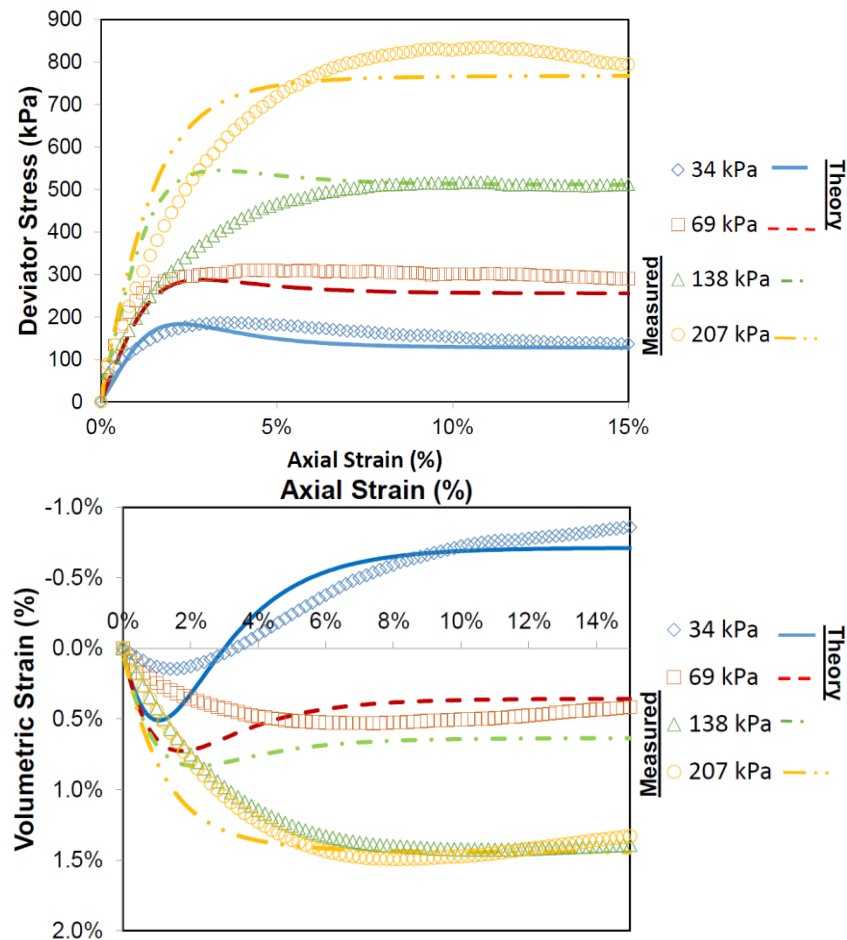


Figure 2-17 The results of Subloading t_{ij} best fit using triaxial test results. (Kaya, 2016)

Shen et al. (2019) performed a three-dimensional finite difference analysis (FLAC3D) of load tests TF-6 and TF-9. Shen et al. (2019) modeled the granular fill using the Mohr-Coulomb model. Additionally, Shen et al. (2019) utilized a linear elastic model to simulate the facing and geotextile. The primary focus of Shen et al.’s (2019) study was to perform a 3D and 2D parametric study on the effect of geosynthetic stiffness, reinforcement spacing, and their combined effects. To perform the parametric study, Shen et al. (2019) first numerically modeled TF-6 and TF-9 mini pier load tests in order to calibrate simulation parameters to the testing results. The geosynthetic reinforcement spacing of TF-6 and TF-9 are

7.5 in (0.19 m) and 15 in (0.38 m), respectively. Results of the calibration numerical modeling are shown below in Figure 2-18 and Figure 2-19.

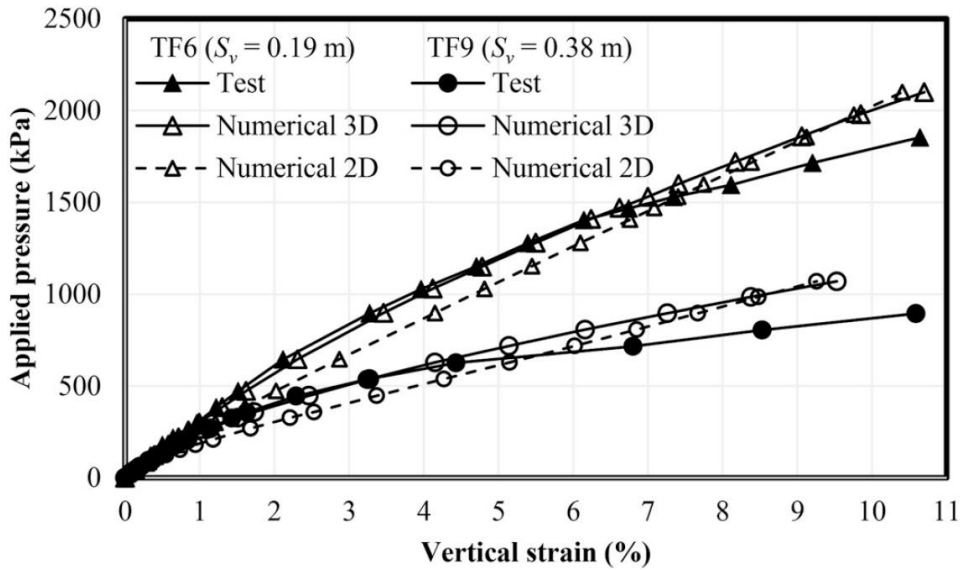


Figure 2-18 Vertical load-displacement curve for mini piers TF-6 and TF-9. (Shen, et al., 2019)

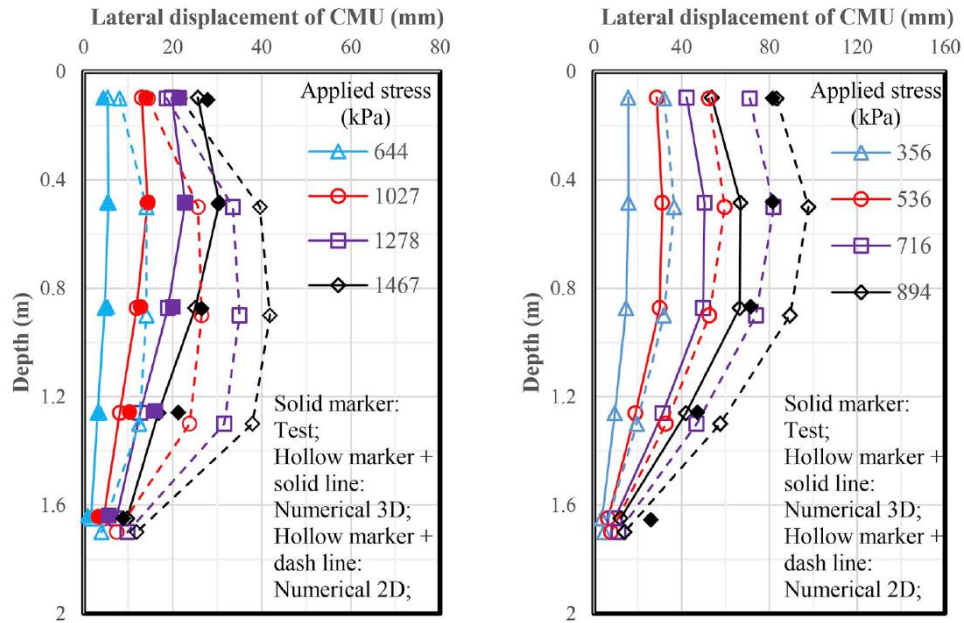


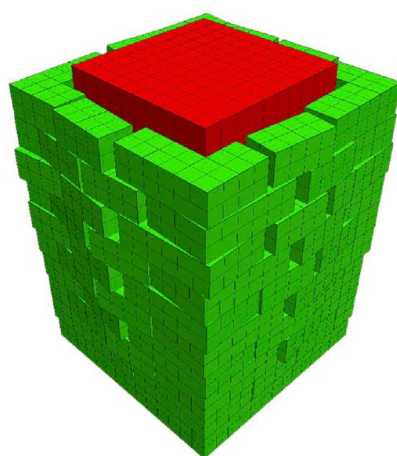
Figure 2-19 Lateral load-displacement curve for mini piers TF-6 (left) and TF-9 (right). (Shen, et al., 2019)

The 3D model of piers TF-6 and TF-9 outperformed the 2D plain strain model and as such, discussion herein will be limited to the 3D model. Model agreement with test results is fairly good for the vertical load-displacement curves. Lateral displacement agreement was less than that of the vertical displacement. Lateral displacements tended to be underpredicted overall but seemed less so for TF-6. The model results of TF-6 outperformed those of TF-9, indicative of a failure to fully capture the soil-structure interaction at play with geosynthetic spacing. The vertical load-displace curves for TF-9 (Figure 2-18)

indicate an underestimation of vertical strains below 5% and an overestimation of strains over 5%. TF-9 has better agreement at lower vertical loads, with the difference in model and test results increasing with increasing load.

An aspect of note in Shen et al.'s (2019) analysis is the generation of model parameters. Shen et al. (2019) utilized various sources to generate parameters to model the material behavior in their finite difference simulation. The first parameter selections of mention are the peak friction angle and corresponding cohesion from Nicks et al. (2013) to describe the Mohr-Coulomb yield criterion. The reported peak friction angle and corresponding cohesion are from large-scale direct shear tests. The elastic modulus and Poisson's ratio are explicitly listed as fitted parameters. Dilation angle was based on the Bolton (1986) correlation for quartz sands. The elastic modulus and Poisson's ratio for the facing were presented without any reported basis. The geotextiles were modeled as isotropic instead of with orthotropic moduli as indicated by testing and the manufacturer. In general, parameters were varied to derive a good fit with the test data.

Despite the limitations described above, several observations of note were enumerated by Shen et al. (2019). First, the general displaced shape of the faced mini piers involves horizontal bulging that typifies the test condition. This displaced shaped can be seen in Figure 2-20 and Figure 2-21. Second, two-dimensional simulation results in significantly more conservative model behavior with a smaller composite stiffness of the mini pier, larger lateral displacements, higher maximum tension in the geosynthetic, and larger normalized lateral earth pressure coefficient. Third, a larger geosynthetic stiffness results predictably, in smaller lateral displacements and larger composite stiffness, however, it does not result in a higher maximum tension in the geosynthetic. Finally, geosynthetic spacing has the largest effect on mini-pier performance. Closer spacing of geosynthetic reinforcement results in larger composite stiffness of the mini pier, smaller lateral displacements and volumetric change of the pier, lower maximum tension in the geosynthetic, and larger normalized lateral earth pressure coefficient independent of geosynthetic stiffness.



(a) Deformed 3D numerical mesh

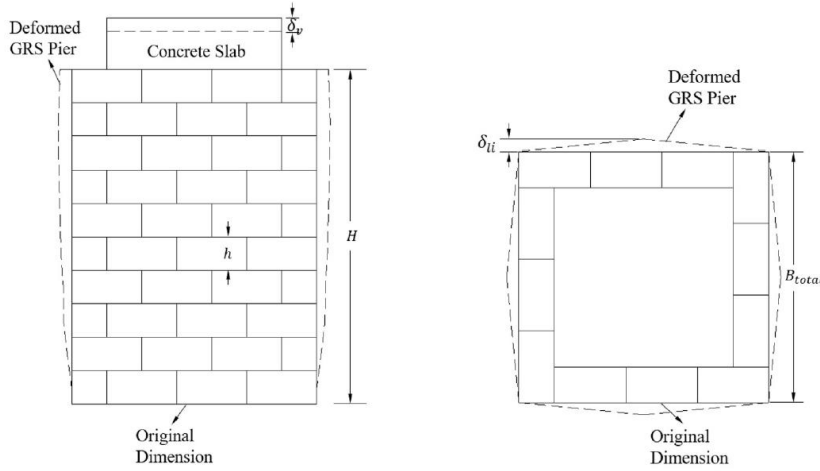
(Magnified 2 times)



(b) Photo of the GRS pier after test

(Nicks et al., 2013)

Figure 2-20 The resulting displaced shape of the finite difference analysis vs the resulting shape of the load testing for TF-6. (Shen, et al., 2019)



(a) Side view of the deformed 2D or 3D GRS pier (b) Plan view of the deformed 3D GRS pier

Figure 2-21 General description of deformed shape for faced GRS mini piers. (Shen, et al., 2019)

2.4 Optimization with Machine Learning

The use of Markov chain Monte Carlo (MCMC) optimization is an established practice for multi-variable optimization problems (Foreman-Mackey et al., 2013). The process is a fundamental application of Bayesian inference, computing and utilizing the posterior probability density function (PDF) for the model parameters. Because of the sampling regime of MCMC algorithms, it is possible to approximate the posterior PDF efficiently despite parameter spaces with high dimensionality. This study makes use of an affine invariant MCMC nicknamed “emcee”. The emcee algorithm is particularly appropriate for the Subloading t_{ij} model as its affine invariance results in performance independent of highly anisotropic posterior PDFs (Goodman & Weare, 2010). Results presented in 4.1.4 below indicates a high initial modality of the posterior PDF with a highly anisotropic PDF emerging under further constraint of parameter bounds.

The basis of the emcee algorithm is the earlier Metropolis-Hastings(M-H) algorithm with an affine invariant process added allowing for equal performance under all linear transformations. The general goal, as is true with all MCMC algorithms, is to compute N samples (steps) $\{\Theta_i\}$ from the posterior PDF (Foreman-Mackey et al., 2013):

$$p(\Theta, \alpha | D) = \frac{1}{Z} p(\Theta, \alpha) p(D|\Theta, \alpha) \quad (\text{Eq. 2.69})$$

where

Θ is the set of model parameters

α is the set of nuisance parameters

D is the set of observations

$p(\Theta, \alpha)$ is the prior distribution

$p(D|\Theta, \alpha)$ is the likelihood function computed for any particular value of (Θ_i, α_i)

$Z = p(D)$ is the normalization and is independent of Θ and α

Because the algorithm at its core is an application of Bayesian inference, it marginalizes over nuisance parameters. These parameters are required to make the model function but are not of significant interest to the user. Marginalizing over nuisance parameters requires integration over all possible values resulting in the propagation of the effects of uncertainty surrounding their value into the result. The result of marginalization over the set of nuisance parameters is (Foreman-Mackey et al., 2013):

$$p(\Theta|D) = \int p(\Theta, \alpha|D) d\alpha \quad (\text{Eq. 2.70})$$

Once the sampling produced by Eq. 2.69 marginalization of Θ is found by projecting the histogram of samples into the parameter subspace spanned by Θ . The result is that the expected value of the function of model parameters $f(\Theta)$ is (Foreman-Mackey et al., 2013):

$$\langle f(\Theta) \rangle = \int p(\Theta|D)f(\Theta)d\Theta \approx \frac{1}{N} \sum_{i=1}^N f(\Theta_i) \quad (\text{Eq. 2.71})$$

The MCMC process generates a random walk in the parameter space where each step in the random walk $X(t_i) = [\Theta_i, \alpha_i]$ depends only on the previous step $X(t_{i-1})$, allowing a representative set of samples to be produced from the distribution.

The emcee algorithm improves on the M-H algorithm using several tactics. The first of which is that the emcee algorithm specifies the use of a simultaneously evolving ensemble of K “walkers” $S = \{X_k\}$. The proposal distribution for one walker k is based on the current positions of the $K - 1$ walkers in the complementary ensemble $S[k] = \{X_j, \forall j \neq k\}$. Each position is a vector in the N -dimensional, real-valued parameter space where N is the parameter space dimension. The position of a walker X_k is updated by drawing a random walker X_j from the ensemble $S[k]$ with a new position proposed (Goodman & Weare, 2010):

$$X_k(t) \rightarrow Y = X_j + Z[X_k(t) - X_j] \quad (\text{Eq. 2.72})$$

where Z is a random variable drawn from $g(Z=z)$.

To determine whether the walk in Eq. 2.72 is symmetric the following equation for g must be true (Goodman & Weare, 2010):

$$g(z^{-1}) = zg(z) \quad (\text{Eq. 2.73})$$

$$g(z) \propto \begin{cases} \frac{1}{\sqrt{z}} & \text{if } z \in \left[\frac{1}{a}, a\right] \\ 0 & \text{otherwise} \end{cases} \quad (\text{Eq. 2.74})$$

where a is a scale parameter with a suggested value $a > 1$ (often set to 2).

Similar to M-H the acceptance probability q is defined as (Goodman & Weare, 2010):

$$q = \min\left(1, Z^{N-1} \frac{p(Y)}{p(X_k(t))}\right) \quad (\text{Eq. 2.75})$$

The detailed balance of the chain will satisfy under the else for the step acceptance conditional (Foreman-Mackey et al., 2013):

```

if  $r \leq q$  then
 $X_k(t+1) \leftarrow Y$ 
else
 $X_k(t+1) \leftarrow X_k(t)$ 
endif

```

where r is a random sample from a uniform distribution $r \sim U[0, 1]$.

The process is repeated such that $k = 1, \dots, K$ resulting in one “move”. The move is analogous to one step in the traditional M-H algorithm.

The emcee algorithm offers improvement on the above affine-invariant MCMC by allowing for parallelization of the move. Parallelizing the process can create significantly increased efficiency, splitting the expensive calculation of q while allowing for a simultaneous solution that does not violate detailed balance. To allow for parallelization the ensemble can be divided into two subsets $S^{(0)} = \{X_k, \forall k = 1, \dots, K/2\}$ and $S^{(1)} = \{X_k, \forall k = K/2, \dots, K\}$. By updating walkers in $S^{(0)}$ using the above procedure but based only on the position of walkers in $S^{(1)}$, all the walkers in $S^{(0)}$ can be updated simultaneously as opposed to in series. The updated walkers in $S^{(0)}$ are then used to perform the same calculation on the walkers in $S^{(1)}$ (Foreman-Mackey et al., 2013). The original affine invariant MCMC step (Goodman & Weare, 2010) and the emcee algorithm steps (Foreman-Mackey et al., 2013) are shown in Figure 2-22 and Figure 2-23 below. The algorithmic step is repeated until a sufficient sampling density of the posterior PDF is reached. Generally, the amount of sampling required can be quantified by the autocorrelation time (Foreman-Mackey et al., 2013):

$$C_f(T) = \lim_{t \rightarrow \infty} \text{cov}[f(X(t+T)), f(X(t))] \quad (\text{Eq. 2.76})$$

$$\tau_f = \sum_{T=-\infty}^{\infty} \frac{C_f(T)}{C_f(0)} = 1 + 2 \sum_{T=1}^{\infty} \frac{C_f(T)}{C_f(0)} \quad (\text{Eq. 2.77})$$

$$C_f(T) \approx \frac{1}{M-T} \sum_{m=1}^{M-T} [f(X(T+m)) - \langle f \rangle] [f(X(m)) - \langle f \rangle] \quad (\text{Eq. 2.78})$$

where

$C_f(T) \rightarrow 0$ such that T is the number of samples to ensure independence

M is the number of samples in the chain (number of steps taken)

Algorithm 2 A single stretch move update step from GW10

```
1: for  $k = 1, \dots, K$  do
2:   Draw a walker  $X_j$  at random from the complementary ensemble  $S_{[k]}(t)$ 
3:    $z \leftarrow Z \sim g(z)$ , Equation (10)
4:    $Y \leftarrow X_j + z [X_k(t) - X_j]$ 
5:    $q \leftarrow z^{N-1} p(Y)/p(X_k(t))$  // This line is generally expensive
6:    $r \leftarrow R \sim [0, 1]$ 
7:   if  $r \leq q$ , Equation (9) then
8:      $X_k(t+1) \leftarrow Y$ 
9:   else
10:     $X_k(t+1) \leftarrow X_k(t)$ 
11:  end if
12: end for
```

Figure 2-22 Affine-invariant MCMC algorithm step. (Foreman-Mackey et al., 2013)

Algorithm 3 The parallel stretch move update step

```
1: for  $i \in \{0, 1\}$  do
2:   for  $k = 1, \dots, K/2$  do
3:     // This loop can now be done in parallel for all k
4:     Draw a walker  $X_j$  at random from the complementary ensemble  $S^{(\sim i)}(t)$ 
5:      $X_k \leftarrow S_k^{(i)}$ 
6:      $z \leftarrow Z \sim g(z)$ , Equation (10)
7:      $Y \leftarrow X_j + z [X_k(t) - X_j]$ 
8:      $q \leftarrow z^{n-1} p(Y)/p(X_k(t))$ 
9:      $r \leftarrow R \sim [0, 1]$ 
10:    if  $r \leq q$ , Equation (9) then
11:       $X_k(t + \frac{1}{2}) \leftarrow Y$ 
12:    else
13:       $X_k(t + \frac{1}{2}) \leftarrow X_k(t)$ 
14:    end if
15:   end for
16:    $t \leftarrow t + \frac{1}{2}$ 
17: end for
```

Figure 2-23 The emcee algorithm step. (Foreman-Mackey et al., 2013)

This study utilizes the emcee algorithm to generate the maximum likelihood parameters for triaxial testing conducted on the granular fill in the FHWA GRS mini piers (Nicks et al., 2013). In the course of this study, the author also utilized the differential evolution algorithm to generate initial parameter values. While this paper does not include an extensive description of the differential evolution algorithm a brief description is included here.

The algorithm attempts to minimize a fitness function $f: \mathbb{R}^n \rightarrow \mathbb{R}$ such that a solution \mathbf{m} is found where $f(\mathbf{m}) \leq f(\mathbf{p})$ for all \mathbf{p} in the search space. Letting $\mathbf{x} \in \mathbb{R}^n$ be a candidate solution from a population of candidate solutions $\mathbf{NP} \geq 4$ (typically $10n$). $\mathbf{CR} \in [0, 1]$ and $F \in [0, 2]$ are the crossover probability and differential weight, respectively. They are both control variables and are set by the user. The population \mathbf{NP} is initialized with random positions in the search space. Until a specified termination criterion is met that is specified by the user, the following iteration is performed for each candidate \mathbf{x} (Storn & Price, 1997):

1. Three agents \mathbf{a} , \mathbf{b} , and \mathbf{c} are chosen from \mathbf{NP} such that \mathbf{a} , \mathbf{b} , \mathbf{c} , and \mathbf{x} are distinct
2. A random index is selected $R \in \{1, \dots, n\}$ where n is the dimension f
3. The agent's potentially new position $\mathbf{y} = [y_1, \dots, y_n]$ is defined as:

- a. For each $i \in \{1, \dots, n\}$, pick a uniformly distributed random number $r_i \sim U[0, 1]$
 - b. If $r_i < CR$ or $i = R$ then $y_i = a_i + F \times (b_i - c_i)$ otherwise set $y_i = x_i$
4. If $f(\mathbf{x}) \leq f(\mathbf{y})$, then \mathbf{x} is replaced with \mathbf{y}

The agent \mathbf{x} from the population \mathbf{NP} with the best fitness is returned as the candidate solution. This candidate solution was utilized by the author as the initialization value for the emcee algorithm discussed above.

3. Mini-pier Performance Testing

3.1 Test Setup

Between 2011 and 2012, 14 GRS mini piers were constructed, instrumented, and load tested at FHWA Turner-Fairbank Highway Research Center (TFHRC) in McLean, Virginia. These load tests were labeled as TF. The main objectives of the testing were: (1) add to the database of GRS material properties utilized by designers, (2) evaluate the relationship between geosynthetic strength and spacing, (3) quantify the frictional connection of facing elements at service limit and strength limit states, (4) assess the design method proposed by Adams et al. (2011), and (5) perform reliability analysis of a proposed soil-geosynthetic capacity equation for LRFD design (Nicks et al., 2013). Of particular interest to this study are the last eight test setups analyzed by Iwamoto (2014). TF-6 through TF-14 represent a parametric study of geosynthetic strength, spacing, and facing conditions. Table 3-1 below summarizes the various geosynthetic/fill/facing configurations employed during load testing.

Table 3-1 Summary of mini pier load test conditions. (Nicks et al., 2013)

Test No.	Backfill				Reinforcement			Facing
	Type	ϕ (°)	c (psf)	d_{max} (inch)	T_f^{\wedge} (lb/ft)	S_v (inch)	T_f/S_v (lb/ft ²)	
DC-1	8	54	0	½	4,800	7½**	7,600	CMU
DC-2	8P*	46	0	¾	4,800	7½**	7,600	CMU
DC-3	57	52	0	1	4,800	7½**	7,600	CMU
DC-4	9	49	0	¾	4,800	7½**	7,600	CMU
DC-5	8***	54	0	½	4,800	7½**	7,600	CMU
TF-1 ⁺⁺	8	55	0	½	2,400	7½	3,800	CMU
TF-2	21A	53	115	1	2,400	7½	3,800	CMU
TF-3	21A	53	115	1	2,400	7½	3,800	no CMU
TF-4 ⁺	21A	53	115	1	4,800	7½	7,600	no CMU
TF-5 ⁺⁺	21A	53	115	1	4,800	7½	7,600	no CMU
TF-6 ⁺⁺	21A	53	115	1	4,800	7½	7,600	CMU
TF-7	21A	53	115	1	4,800	7½	7,600	no CMU
TF-8	21A	53	115	1	4,800	7½**	7,600	no CMU
TF-9	21A	53	115	1	4,800	15¼	3,800	CMU
TF-10	21A	53	115	1	4,800	15¼	3,800	no CMU
TF-11	21A	53	115	1	1,400	3 ¹³ / ₁₆	4,400	no CMU
TF-12	21A	53	115	1	1,400	3 ¹³ / ₁₆	4,400	CMU
TF-13	21A	53	115	1	3,600	11¼	3,800	no CMU
TF-14	21A	53	115	1	3,600	11¼	3,800	CMU

ϕ = the peak friction angle, c = the cohesion at peak strength, d_{max} = the maximum aggregate size, T_f = the ultimate reinforcement strength, expressed as the minimum average roll value (MARV) from ASTM D4595 testing,⁽¹⁾ and S_v = the reinforcement spacing.

⁺ MARV value.

*Rounded pea-gravel angularity.

**Two courses of bearing bed reinforcement placed at the top of the PT.

***Uncompacted sample, +technical difficulties required termination during testing.

++Technical difficulties resulted in unloading/reloading of the composite.

The test setup can broadly be described as an approximately 3.26 ft. by 3.26 ft. by 6.5 ft. composite soil column with alternating layers of granular fill and geosynthetic. The facing material employed is mortarless dry stacked CMUs. Both the faced and un-faced load tests were constructed using the same general procedure with the un-faced having the facing removed as a final step. The construction sequence is described below in 3.2.1 with the constructed piers shown in Figure 1-2 and Figure 1-3 prior

to loading. All mini piers loaded during the TFHRC round of testing were constructed using a 2:1 height-to-width ratio to mimic triaxial testing conditions (Nicks et al., 2013). Figure 3-1 and Figure 3-2 below show the general elevation and plan views of the constructed mini piers.

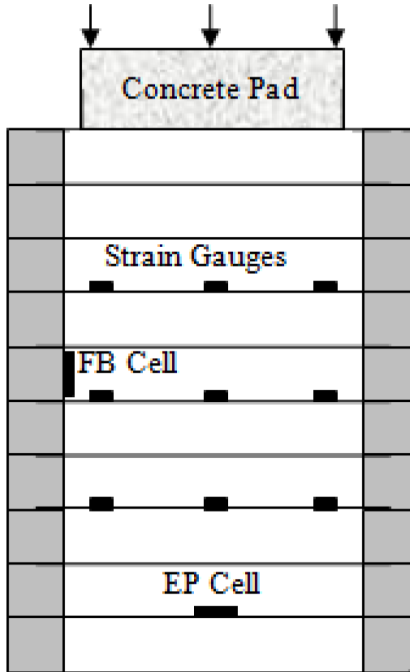


Figure 3-1 Typical GRS mini pier elevation view with instrumentation. (Nicks et al., 2013)

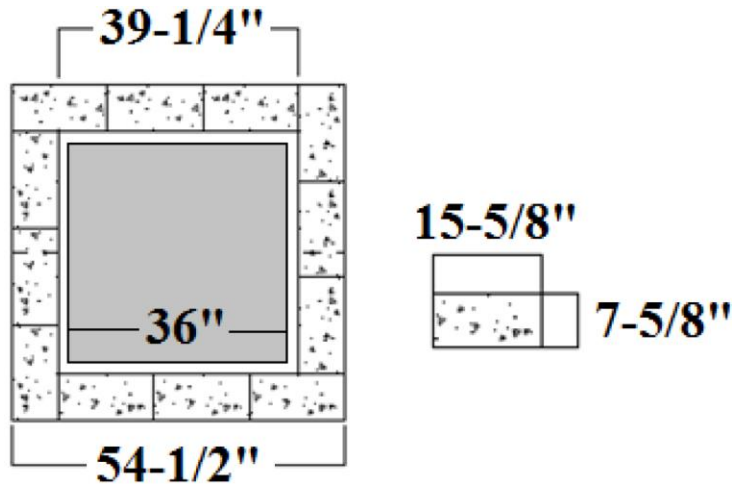


Figure 3-2 Typical Cross section (top view) and CMU facing dimensions for GRS mini pier. (Nicks et al., 2013)

The focus of this study is to model the behavior of two of the eight piers analyzed by Iwamoto (2014). The piers of interest are the two unfaced, TF-7 and TF-10. Both test piers have the same general soil column dimensions, aggregate backfill, and geosynthetic reinforcement material properties. Reinforcement spacing is the primary variable of concern in this paper.

3.2 Aggregate, Geosynthetic, and Facing

3.2.1 Aggregate Backfill

The aggregate backfill utilized to construct the GRS piers was a well-graded gravel with silt (GW-GM) from Lucky Stone quarry in Leesburg, VA. The backfill met the Virginia Department of Transportation (VDOT) 21A base course specifications as well as the FHWA's GRS-IBS backfill requirements (Iwamoto, 2014). A sieve analysis was performed in accordance with ASTM D422. The gradation of the VDOT21A is shown in Figure 3-3 (Nicks et al., 2013).

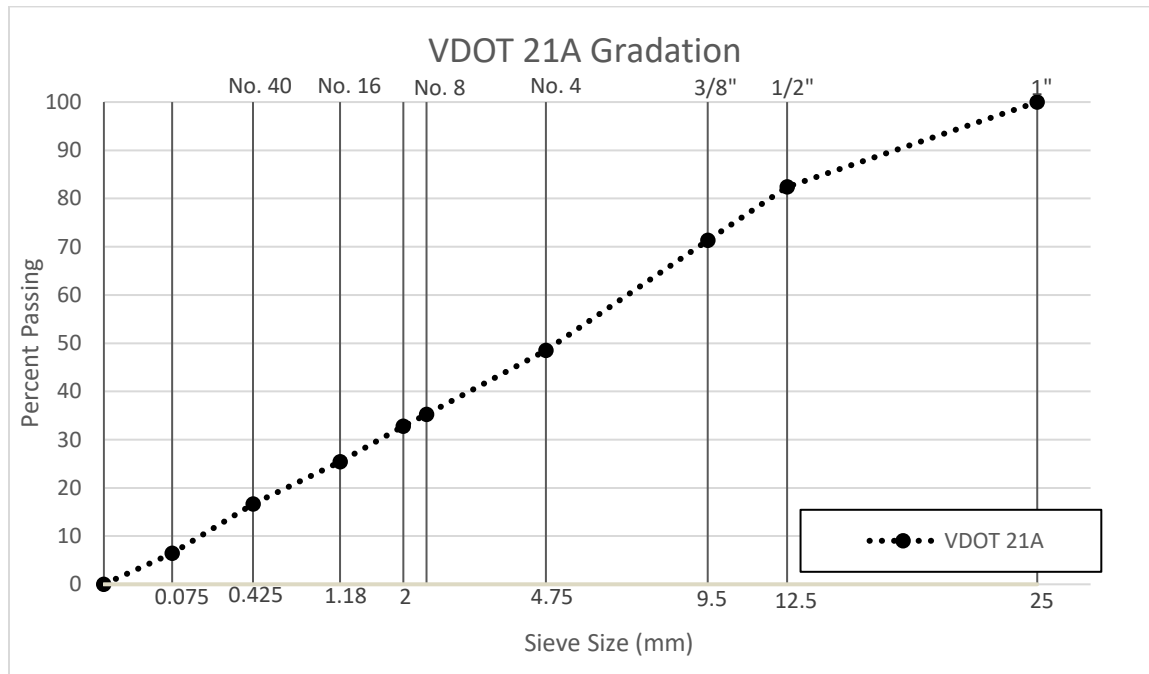


Figure 3-3 VDOT 21A aggregate backfill aggregate. (Nicks et al., 2013)

To determine compaction requirements for construction of the piers, a standard Proctor compaction test was conducted according to Method D of AASHTO T99 for the VDOT 21A material. The proctor test results (maximum dry unit weight, $\gamma_D = 148.90$ pcf, and optimum moisture content, $\omega = 7.7\%$) are shown in Figure 3-4.

8 large-scale direct shear samples were prepared at approximately optimum conditions ($\gamma_D = 147$ pcf and $\omega = 7.5\%$). 4 were then soaked and tested in a saturated state while the other 4 were tested without soaking. Shear testing was performed at saturation and dry to capture non-linear soil behavior in the Mohr-Coulomb cohesion and friction angle (Nicks et al., 2013). The 12 in. by 12 in. by 8 in. samples were subjected to 5, 10, 20, and 30 psi normal confining stresses. The samples were sheared at a rate of 0.015 inches/min with a box gap of 0.57 inches based on the D_{85} of VDOT21A. Figure 3-5 shows the results of the large-scale direct shear testing. The derived Mohr-Coulomb failure envelope for the optimum moisture content testing resulted in a peak friction angle of 53° and a cohesion of 1563 psf. The results for the saturated sample are similar, with a peak friction angle of 54° and a cohesion of approximately 115 psf (Nicks et al., 2013).

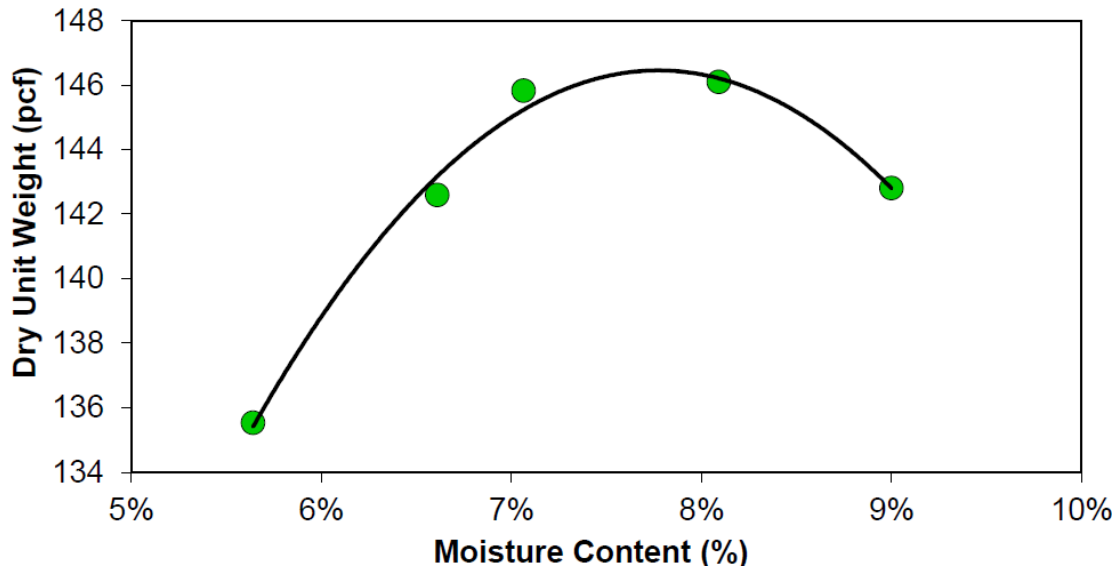


Figure 3-4 Results of standard Proctor test on the aggregate backfill, VDOT 21A. (Nicks et al., 2013)

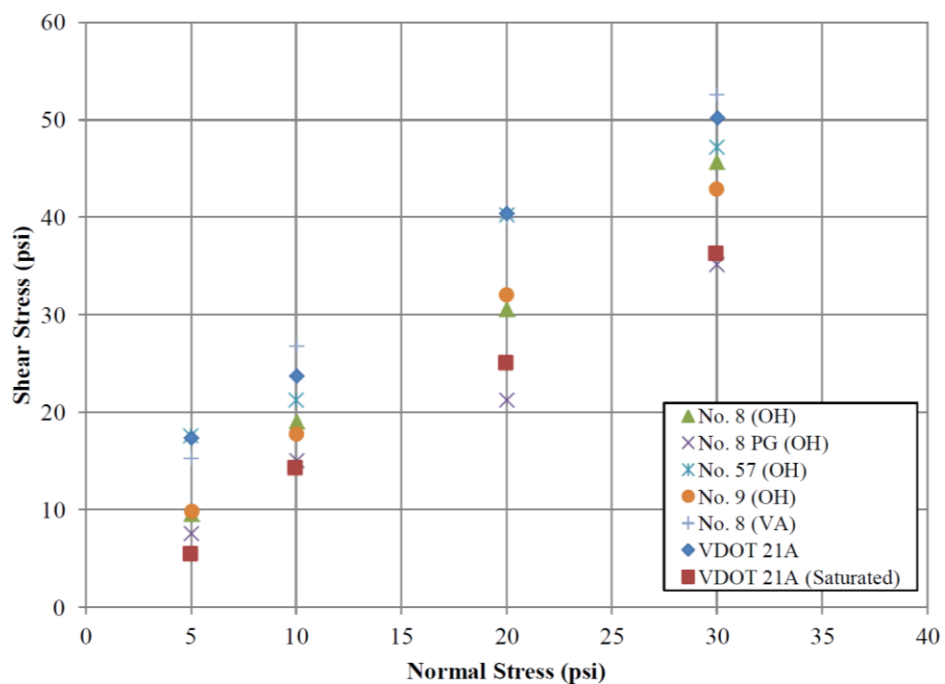


Figure 3-5 Results of large-scale direct shear testing conducted on various backfill materials. (Nicks et al., 2013)

Iwamoto (2014) includes a discussion of the validity of the use of peak friction angle for predicting GRS composite strength. Iwamoto (2014) and Iwamoto et al. (2013) suggest that different magnitudes of movement are required to fully mobilize the strength of the aggregate versus the reinforcement. Testing indicates that "...strong reinforcement strengthens the soil considerably causing the GRS/GMSE to experience large strains ($> 10\%$) prior to failure whereas the peak strengths of the soils utilized in these load tests were mobilized at relatively small shear strains ($\approx 2\text{-}5\%$) in large scale direct shear or triaxial tests." (Iwamoto, 2014). Figure 3-6 shows a comparison of the resulting linear failure Mohr-Coulomb failure envelopes obtained when mobilized at peak and fully softened states. The result is

a comparable friction angle with the peak strength case having a higher cohesion. Difficulty in capturing fully non-linear behavior leads to the adoption of the saturated test results by Nicks et al. (2013), Iwamoto (2014), Kaya (2016) and Shen et al. (2019). It should be noted that the Subloading t_{ij} model does not require estimation of the peak friction angle. The critical state friction angle is implied in the parameter M .

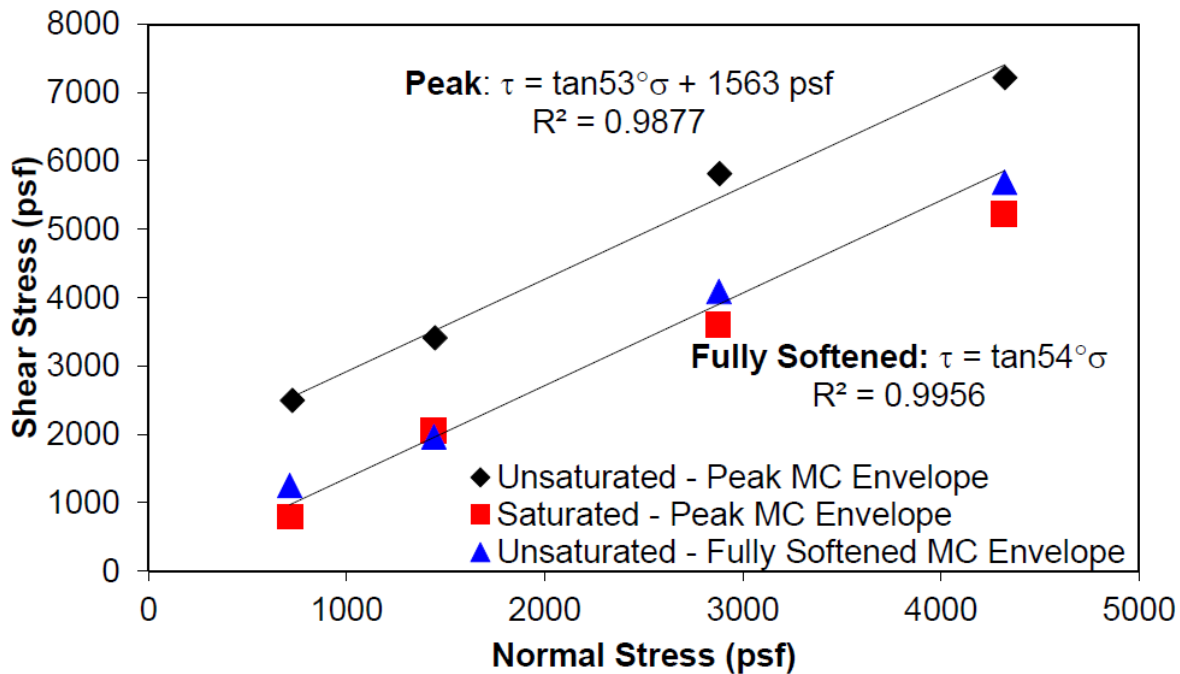


Figure 3-6 Comparison of saturated, unsaturated, and fully softened Mohr-Coulomb envelopes. (Iwamoto, 2014)

During construction of the GRS piers, compaction occurred in approximately 4-inch-thick lifts with the aid of a Vibco Patchman PM1012 plate compactor. To provide sufficient confinement and to prevent the CMU facing from bulging, the top two rows of CMUs were held in place using ratchet straps with 2x4 lumber sandwiched between the facing and the ratchet straps to evenly distribute the lateral forces. Application of this approach is demonstrated in Figure 3-7. After compaction of each lift, a nuclear densitometer was employed to ensure that 100% relative compaction compared to the standard Proctor was reached as well as confirm that the water content was within $\pm 2\%$ of optimum. To create the unfaced conditions in the specified piers, the CMU blocks were removed and the geosynthetic was trimmed to the dimension of the soil column. Figure 3-13 and Figure 3-14 in Section 3.3 are schematics of the TF-6, -7, -9, and -10 GRS piers as constructed with instrumentation.



Figure 3-7 Staged construction employed to construct FHWA GRS test piers. (Iwamoto, 2014)

3.2.2 Geotextile Reinforcement

Geosynthetic reinforcements were all biaxial, woven polypropylene Propex Geotex 4X4HF geotextile. Figure 3-9 shows the wide width tensile strength and stiffness characteristics such as the wide width anisotropic elongation. To prevent preferential failure along a weaker axis, an alternating pattern with each successive reinforcement layer rotated in-plane 90° was adopted during construction. T_f will from hereon be used to refer to reinforcement strength while S_v will refer to reinforcement spacing.

Test	Geotextile Manufacturer	Wide Width Tensile Strength (lb/ft)	Wide width tensile strength at 5% strain (lb/ft)	Tensile Strength (Grab) (lb)	Wide Width Elongation (%)
TF-6, -7, TF-9, -10	Propex	4800 x 4800	660 x 1500	600 x 500	(10 x 8%)

Figure 3-8 Schedule of geosynthetic properties utilized during GRS pier load tests. (Iwamoto, 2014)

3.2.3 CMU Facing



Figure 3-9 CMU block dimensions. (Iwamoto, 2014)

The CMU block facing was dry-cast and split-faced with nominal dimensions of 7.625 in. high by 15.625 in. long by 7.625 in. wide, each weighing an average of 42 lbs. Facing was frictionally connected to geotextile reinforcement and dry-stacked with a coverage ratio of 85% as specified by Adams et al. (2011).

3.3 Load Testing and Instrumentation

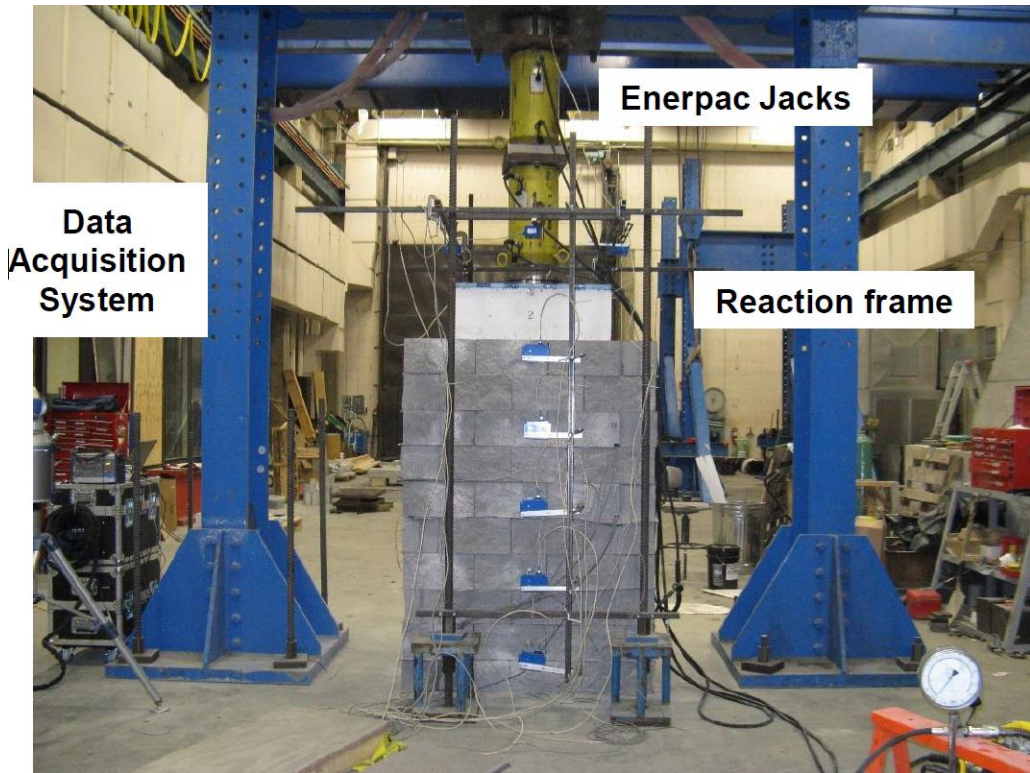


Figure 3-10 FHWA TFHRC GRS mini pier load testing set up. (Iwamoto, 2014)

Load testing of the GRS mini piers was conducted using the load frame shown above in Figure 3-10. The loading mechanism is a pair of 600-kip Enerpac 12-in stroke hydraulic jacks in series resulting in a 24-in total stroke length. The load jacks were fixed to a steel wide-flange reaction frame that was bolted to a solid floor slab. A spherical bearing (Figure 3-11) served as the interface between the load jack and the footing, maintaining a normal load while preventing induced moments. Load increments were applied manually using a solenoid valve hydraulic pump with a constant load maintained by a strain

indicator calibrated to a load cell within the reaction assembly. Load increments were held until there was no significant change in displacement (< 0.003 inches) between any two recording times. Each load increment was held for a minimum of 5 minutes and a maximum of 30 minutes. Settlement was recorded by the data acquisition system at 1-, 3-, 5-, 7-, 15-, 20-, 25-, and 30-minute intervals after the start of each load increment. Deflections were recorded during load testing but not during construction. Each load test typically took approximately 6 hours to complete (Nicks et al., 2013).



Figure 3-11 Spherical bearing interface between hydraulic jack and footing. (Nicks et al., 2013)

During load testing: string potentiometers were utilized to monitor vertical deflection of the footing at the top of the mini pier and horizontal displacement along the height of the faced mini pier, linear variable differential transformers (LVDT) were utilized to measure lateral displacement along the height of the unfaced mini piers, earth pressure cells were used to measure vertical and horizontal earth pressures within the GRS column and, strain gauges were attached directly to the geosynthetic reinforcement to measure in-plane strains. The instrumentation installed in and on TF-6, -7, -9, and -10 is shown below in Figure 3-13 and Figure 3-14 (Nicks et al., 2013).

Lateral earth pressure was measured a 6-in diameter “fatback” cell, Geokon model 4810, which is designed to measure earth pressure against structural faces. Vertical earth pressure was measured one block height above the bottom of the pier using a 9-in diameter Geokon model 4815. EP-08-250BG-120 strain gauges manufactured by Vishay Measurements Group, Inc. were glued to a 1-in by 3-in patch before being attached to the geotextile using the University of Colorado at Denver method. The 5 strain gauges were set in an L-shaped pattern so as to capture strains orthogonally. External LVDTs and string potentiometers (POT) were clamped to fixed reference beams erected adjacent to the mini pier. Figure 3-12 shows the installed LVDTs and POTs.

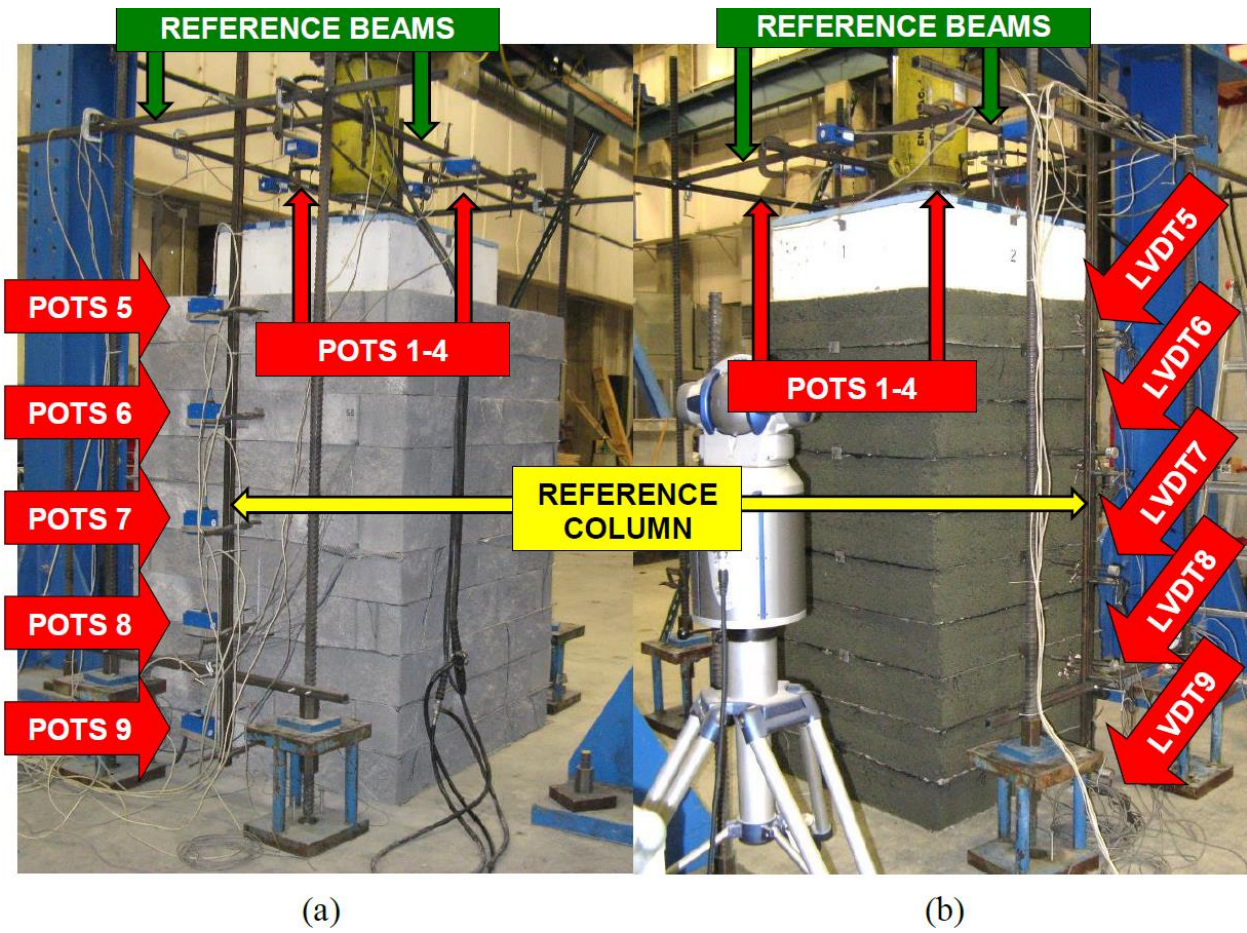


Figure 3-12 Schematics of deflection instrumentation for mini piers (a) with facing and (b) without facing. (Iwamoto, 2014)

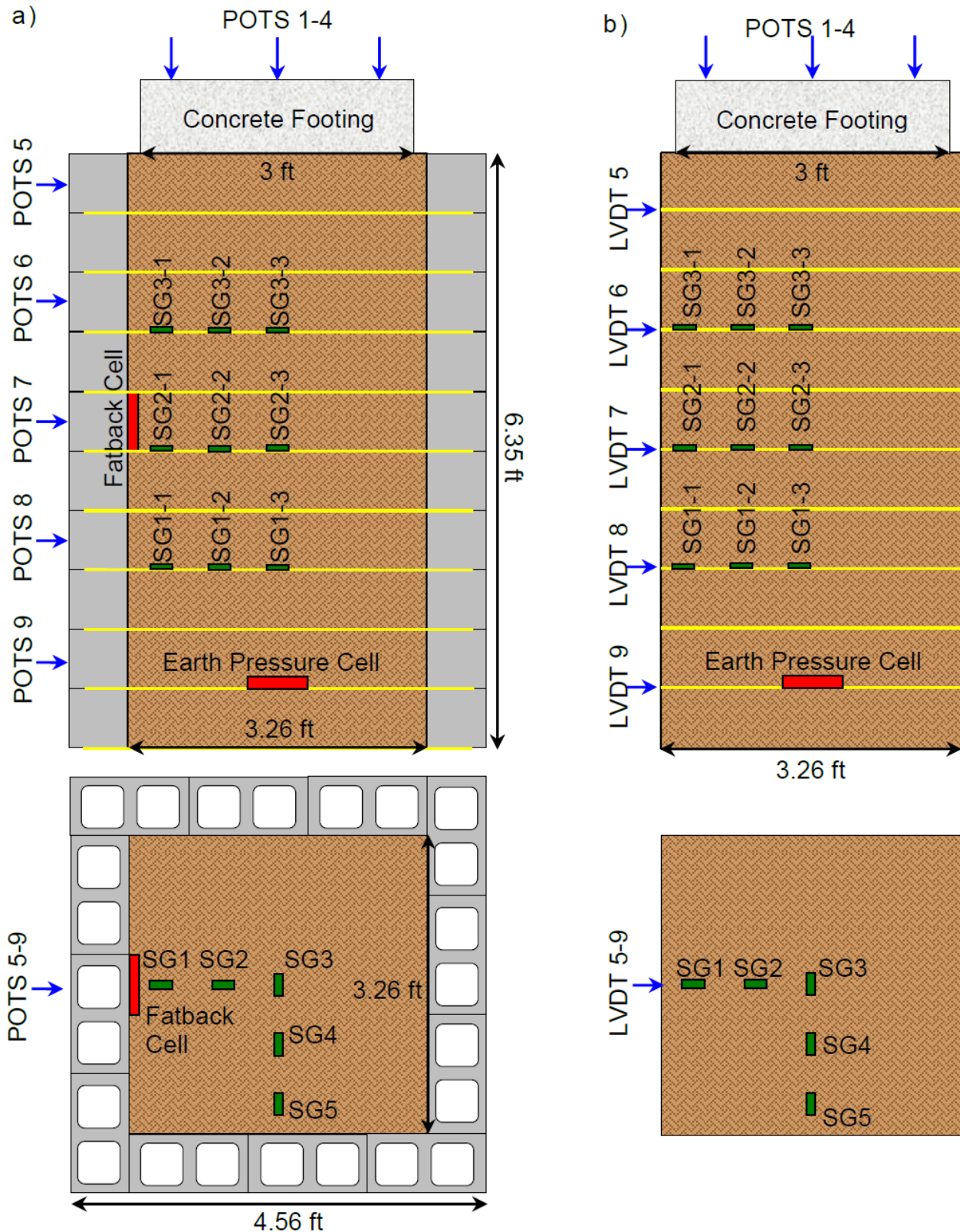


Figure 3-13 Instrumentation and schematic for a) plan and profile of TF-6 and b) plan and profile of TF-7. (Iwamoto, 2014)

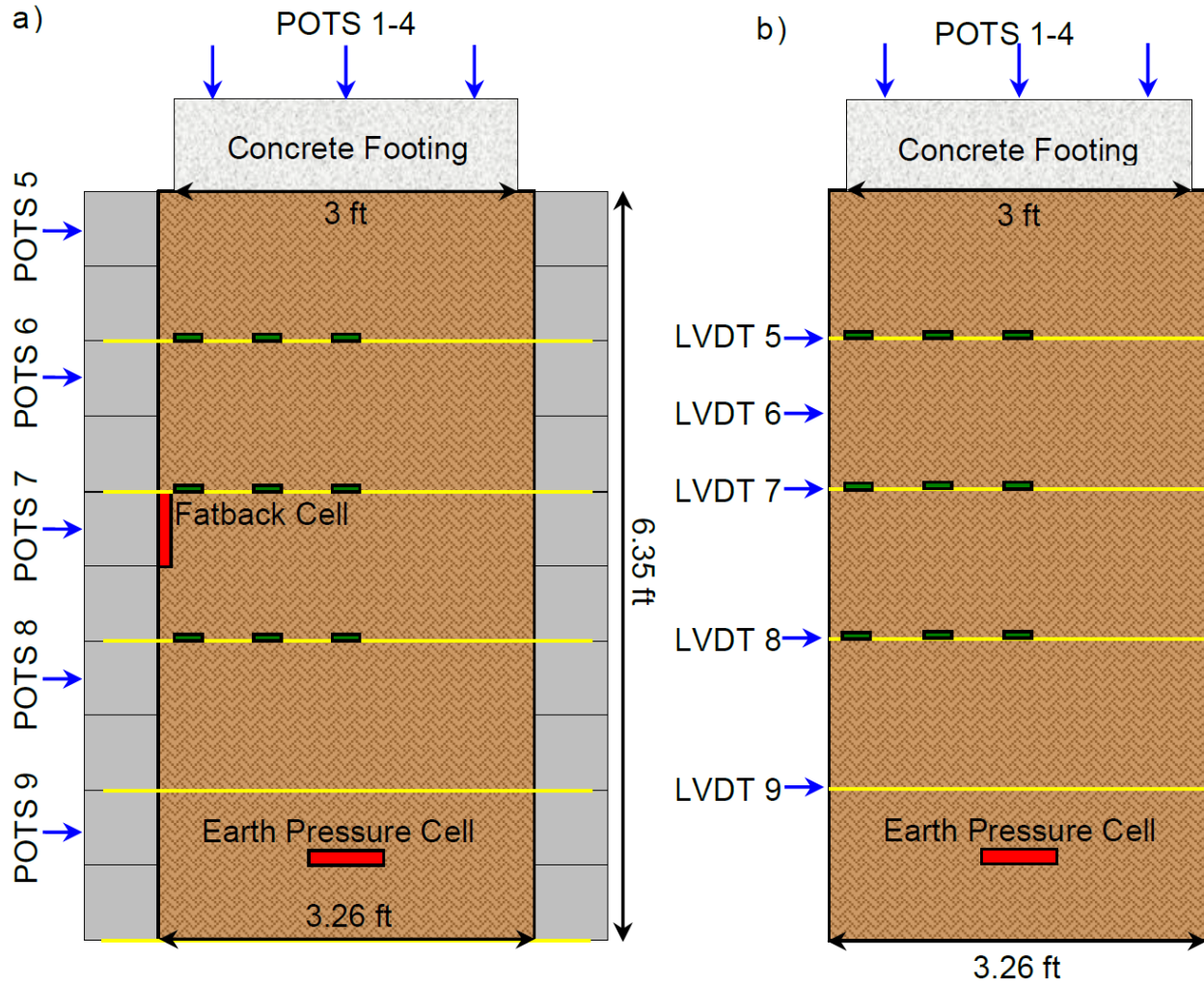


Figure 3-14 Instrumentation and schematic for a) plan and profile of TF-9 and b) plan and profile of TF-10. (Iwamoto, 2014)

3.4 Results

Ultimate bearing capacity q_{\max} and ultimate strain ε_{\max} are summarized in Table 3-2 for all the mini-pier tests conducted by FHWA. Iwamoto (2014) used the results shown in Table 3-3 Summary of failure strain and load capacity with key pier aspects. (Iwamoto, 2014)Table 3-3 and made three key conclusions. First, CMU-faced tests yielded greater load capacity due to the confining pressure they offer than un-faced tests. Second, reinforcement spacing has a greater influence on capacity than reinforcement strength. This fact has been confirmed and reinforced by several sources, including Shen et al. (2019) discussed in Section 2.3. Third, the ratio of ultimate capacity with and without CMU facing increased with increasing in reinforcement spacing and tensile strength. The corollary is that the resulting contribution of the CMU facing to capacity increases with increased reinforcement spacing and strength or as Iwamoto (2014) put it, "...the smaller the reinforcing spacing and the weaker the reinforcing, the smaller will be the effect of the CMU blocks on the capacity."

Table 3-2 Summary of FHWA GRS mini pier load testing results. (Nicks et al., 2013)

Test No.	Maximum Tested		Strength Limit	Design Limit		Service Limit
	q _{max} (psf)	ε _{max} (%)	q _{ult,emp} (psf)	q _{@ε=5%} (psf)	V _{allow,emp} = q _{@ε=5%} /3.5 (psf)	q _{@ε=0.5%} (psf)
DC-1	23,310	7.95	23,310	19,983	5,709	3,065
DC-2	22,709	7.07	22,709	19,399	5,543	2,171
DC-3	18,447	5.82	N/A	16,182	4,623	1,324
DC-4	26,730	7.64	N/A	17,350	4,957	2,212
DC-5	21,539	10.42	21,539	11,761	3,360	316
TF-1	20,487	10.9	20,487	13,409	3,831	2,075
TF-2	25,260	11.46	25,260	18,711	5,346	4,759
TF-3	17,491	13.8	17,491	12,120	3,463	3,417
TF-4	14,240	4.4	N/A	N/A ¹	N/A ¹	3,705
TF-5	25,920	17.9	25,920	15,581	4,452	1,815
TF-6	43,828	15.7	43,828	22,007	6,288	3,704
TF-7	26,546	12.5	26,546	13,684	3,910	2,224
TF-8	29,134	17.8	29,134	13,797	3,942	1,753
TF-9	22,310	15.6	22,310	13,527	3,865	2,955
TF-10	10,330	14.27	10,330	7,374	2,107	1,586
TF-11	23,249	12.79	23,249	13,316	3,805	2,839
TF-12	29,030	13.37	29,030	18,573	5,307	4,028
TF-13	12,960	12.32	12,960	8,641	2,469	2,398
TF-14	23,562	12.69	23,562	16,748	4,785	2,037

q_{max} = the maximum applied pressure during testing, ε_{max} = the maximum recorded vertical strain, q_{ult,emp} is the measured failure pressure, q_{@ε=5%} = the applied stress at 5 percent vertical strain, V_{allow,emp} is the total allowable pressure on the GRS,⁽¹⁾ q_{@ε=0.5%} = the applied stress at 0.5 percent vertical strain.

N/A = Not applicable, did not fail composite. N/A¹ = Not applicable, composite did not reach 5-percent vertical strain before it was terminated.

Table 3-3 Summary of failure strain and load capacity with key pier aspects. (Iwamoto, 2014)

Test	T _f ¹ (lb/ft)	S _v ² (in)	T _f /S _v (ksf)	Height (ft)	Facing Type	q _{ult,emp} ³ (ksf)	q _{ult,CMU} ⁴ / q _{ult,No CMU} ⁵	ε _f ⁶ %
TF-6	4800	7.63	7.55	6.35	CMU	43.8	1.65	15.7
TF-7	4800	7.63	7.55	6.35	None	26.5		12.5
TF-9	4800	15.3	3.78	6.35	CMU	22.3	2.17	15.6
TF-10	4800	15.3	3.78	6.35	None	10.3		14.3
TF-11	1400	3.81	4.41	6.35	None	23.2	1.25	12.8
TF-12	1400	3.81	4.41	6.35	CMU	29.0		13.4
TF-13	3600	11.3	3.84	6.56	None	13.0	1.82	12.3
TF-14	3600	11.3	3.84	6.56	CMU	23.6		12.7

Notes:

1. T_f = wide width tensile strength (all geotextiles have identical wide width tensile strengths in the machine and cross machine directions)

2. S_v = reinforcement spacing

3. q_{ult,emp} = ultimate bearing capacity of mini-pier

4. q_{ult,CMU} = ultimate bearing capacity of mini-pier with CMU

5. q_{ult,No CMU} = ultimate bearing capacity of mini-pier without CMU

6. ε_f = strain of load test at failure

Table 3-2 shows the resulting load-settlement curves for all FHWA TFHRC GRS mini pier load tests. A clear standout is TF-6 which had the highest reinforcement strength-to-spacing ratio and a backfill most likely to generate the highest capacity (well-graded gravel). Another distinction is the differential between otherwise identical GRS piers with the only difference being faced vs. unfaced. Pairs of faced and unfaced piers are generally indicated by the same symbology with faced piers having solid markers and lines while unfaced piers have dashed lines and empty markers. In general, Figure 3-15 demonstrates that faced piers provided higher ultimate capacities as indicated by Iwamoto (2014). Facing provides confining pressure as well as prevents spalling as shown in Figure 3-16. Normalized load-settlement curves shown in Figure 3-17 follow a general trend and are confined to within a fairly narrow range.

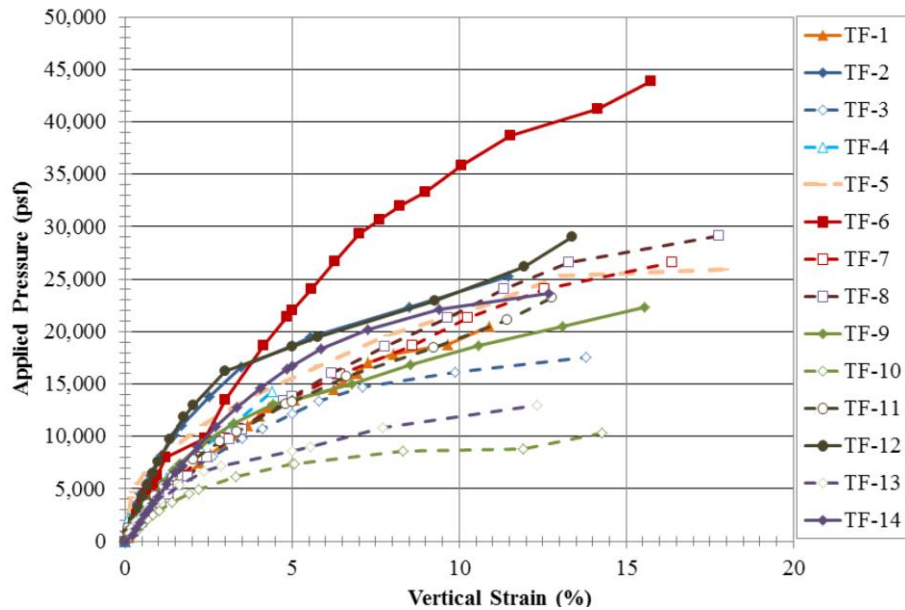


Figure 3-15 Vertical load-displacement curves for all of the TFHRC load tests. (Nicks et al., 2013)



Figure 3-16 TF-10 at failure with $S_v = 15\frac{1}{4}$ inches, $T_f = 4,800 \text{ lb}/\text{ft}$, and VDOT 21A material. (Nicks et al., 2013)

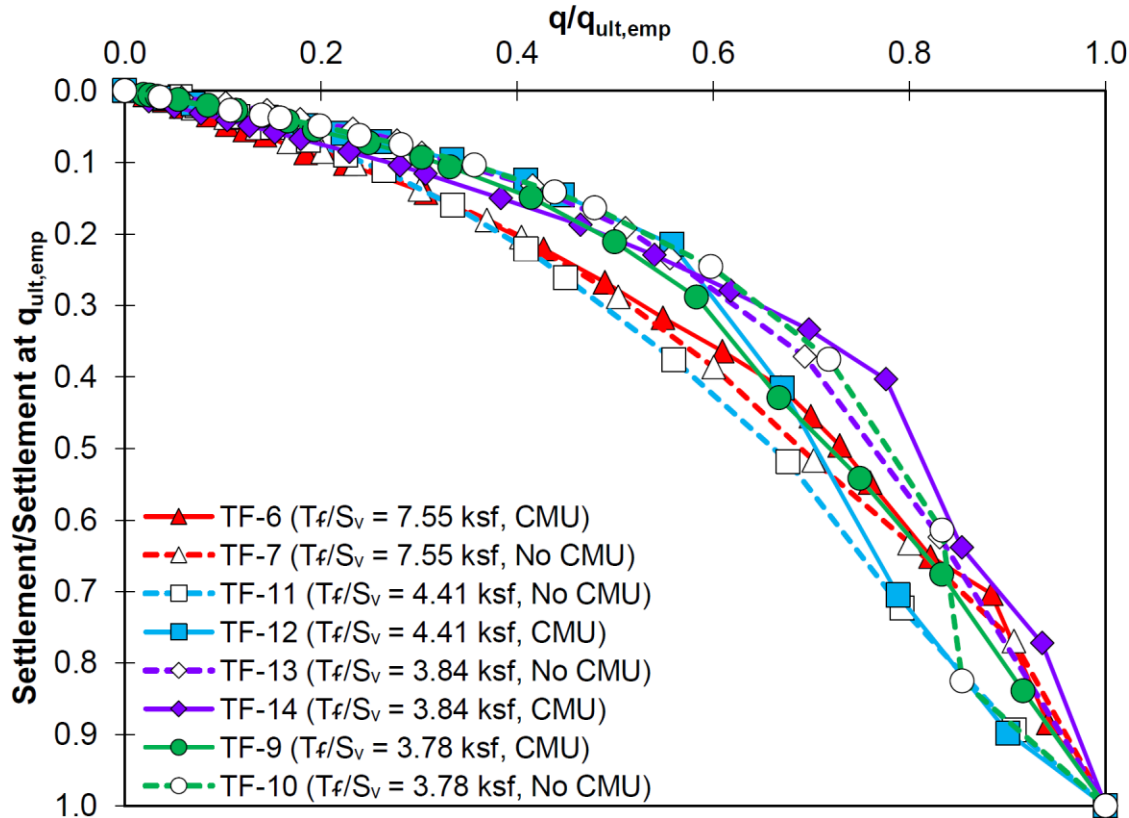


Figure 3-17 Normalized load-settlement curves for selected TFHRC GRS mini pier load tests. (Iwamoto, 2014)

The failure modes of closely spaced (<12 inches) reinforcement piers resulted in geosynthetic rupture along a fairly well-defined shear plane as seen in Figure 3-18. In addition, rupture of the geosynthetic at the soil-geosynthetic-facing interface can also be seen. The frictional connection between the geosynthetic and the CMU facing was sufficient to provide a 'clamping' force, generating localized excess stress as the central portion of the geosynthetic and the aggregate backfill settled while the facing did not. This can be most clearly seen in the second through seventh layer of reinforcement in Figure 3-18. Nicks et al. (2013) explained that the well-defined shear plane did not appear in piers with >12 inches of reinforcement spacing. Instead, failure occurred in the intermediate aggregate backfill without obvious geosynthetic rupture. TF-10 in Figure 3-16 above is a notable example of this failure type. Finally, crushing and cracking of the CMU facing occurred in TF-6 seen in Figure 3-19.

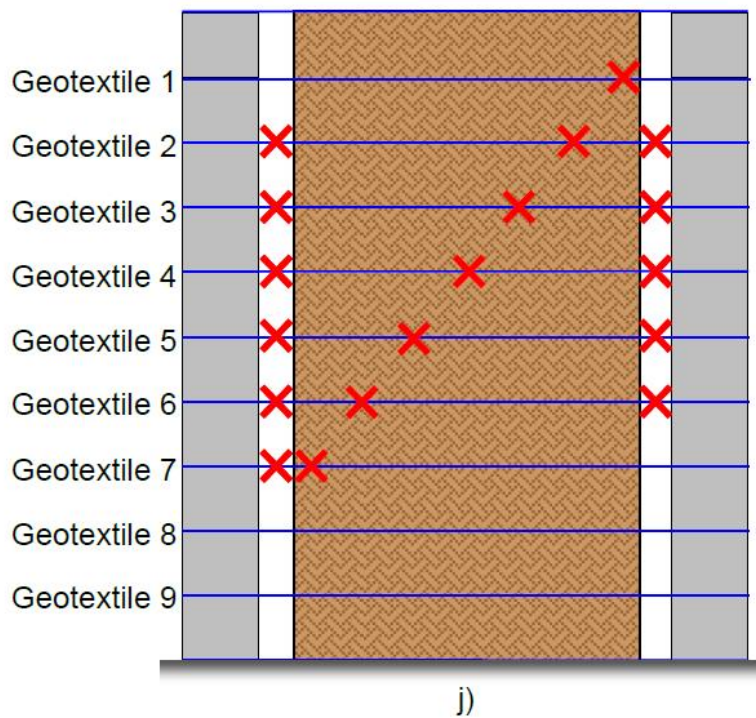
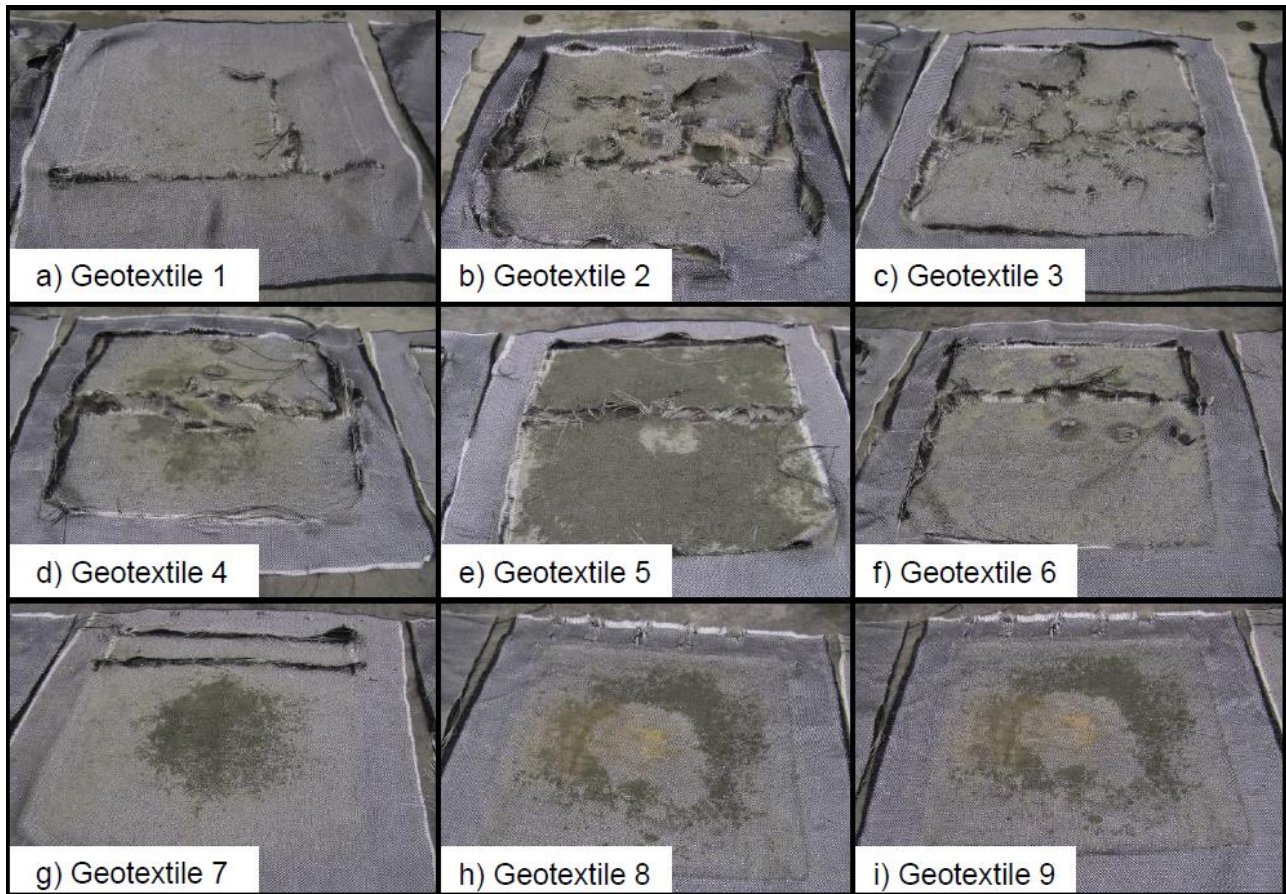


Figure 3-18 For TF-6: a) through i) images of individual reinforcement rupture; j) elevation view of reinforcement rupture.
(Iwamoto, 2014)



Figure 3-19 TF-6 ($S_v = 7\frac{1}{8}$ inches, $T_f = 4,800 \text{ lb}/\text{ft}$) facing cracking and crushing post load testing. (Nicks et al., 2013)

Lateral deflections of the mini-piers are presented in Figure 3-20, Figure 3-21, Figure 3-22, Figure 3-23, and Figure 3-24. Iwamoto (2014) pointed out that based on the behavior of TF-12 and TF-14 (Figure 3-20), lateral pressure increased gradually to a maximum that fell on the line representing the coefficient of active earth pressure before decreasing abruptly. Iwamoto (2014) explained that settlement caused tension development in the reinforcement, thereby pulling the facing laterally towards the soil resulting in an increase in confining pressure. This occurred until the reinforcing tensile strength was reached, leading to rupture and load shedding to other reinforcement layers. This process repeats until the confining stress induced by the facing became negligible, and the pier behavior resembled that of an unfaced test where the GRS composite structure sheared along a failure plane. This behavior can be seen in Figure 3-20 with TF-6's stress path. Unfortunately, the fatback cells recording lateral earth pressure in TF-6 and TF-12 failed during testing and so a complete history is unavailable (Iwamoto, 2014).

The lateral deflections shown in Figure 3-21, Figure 3-22, Figure 3-23, and Figure 3-24 back up the conclusions made by Iwamoto (2014). The lateral deflection of TF-6 shows a reversal that occurred at the 269-psi loading step in the top POTs reading. This decrease in deflection is likely due to the rupture of the reinforcement at or near mid-height first resulting in a redistribution of load to the adjacent geosynthetic layers. Additionally, the results reinforce the fact that the CMU facing increases the load capacity of the GRS piers and reduces the lateral deflection, thereby improving serviceability. The ratio of lateral deflection at failure in the faced vs unfaced piers decreased with decreasing reinforcement spacing (TF-6:TF-7 < TF-9:TF-10), indicating that reinforcement spacing has a more significant effect on serviceability than T_f .

The maximum lateral deflection in piers where $S_v < 12$ in. occurred approximately in the middle third of the pier. Maximum lateral deflections in TF-9 and TF-10, in which S_v was approximately $15\frac{1}{4}$ in.,

occurred in the top third of the piers, distinctly different from those exhibited in piers with closer reinforcement spacing. Iwamoto (2014) indicated that the case in which there is less reinforcement results in greater deformation due to less locked-in stresses. Iwamoto (2014) further pointed out that when comparing faced vs unfaced cases, the point of maximum deflection is shifted upwards. This can be seen in Figure 3-21 and Figure 3-22 with a shift of the maximum from 35 in. from the top of the pier (TF-7) to 18.75 in. from the top of the pier (TF-6).

A final note, due to excessive raveling of TF-10 and TF-13 around the LVDT reaction plates, the LVDTs were removed prior to pier failure. Reliable readings were therefore only available up to 83% of the ultimate load (Iwamoto, 2014). Figure 3-25 below shows the resulting deflection profiles when considering lateral deflections at approximately 83% of the ultimate load capacity.

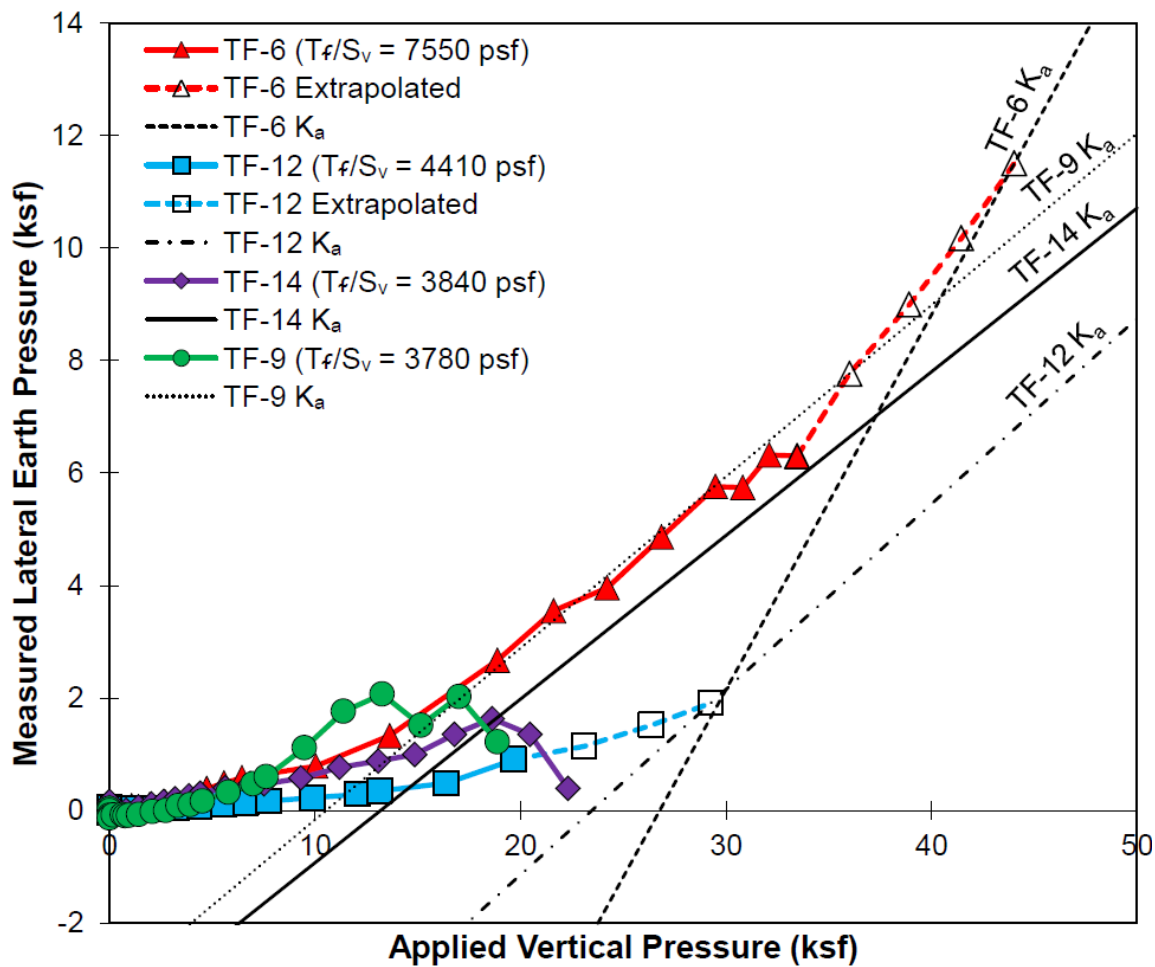


Figure 3-20 Fatback cell measured lateral pressures during load testing of TF-6, -9, -12, and -14. (Iwamoto, 2014)

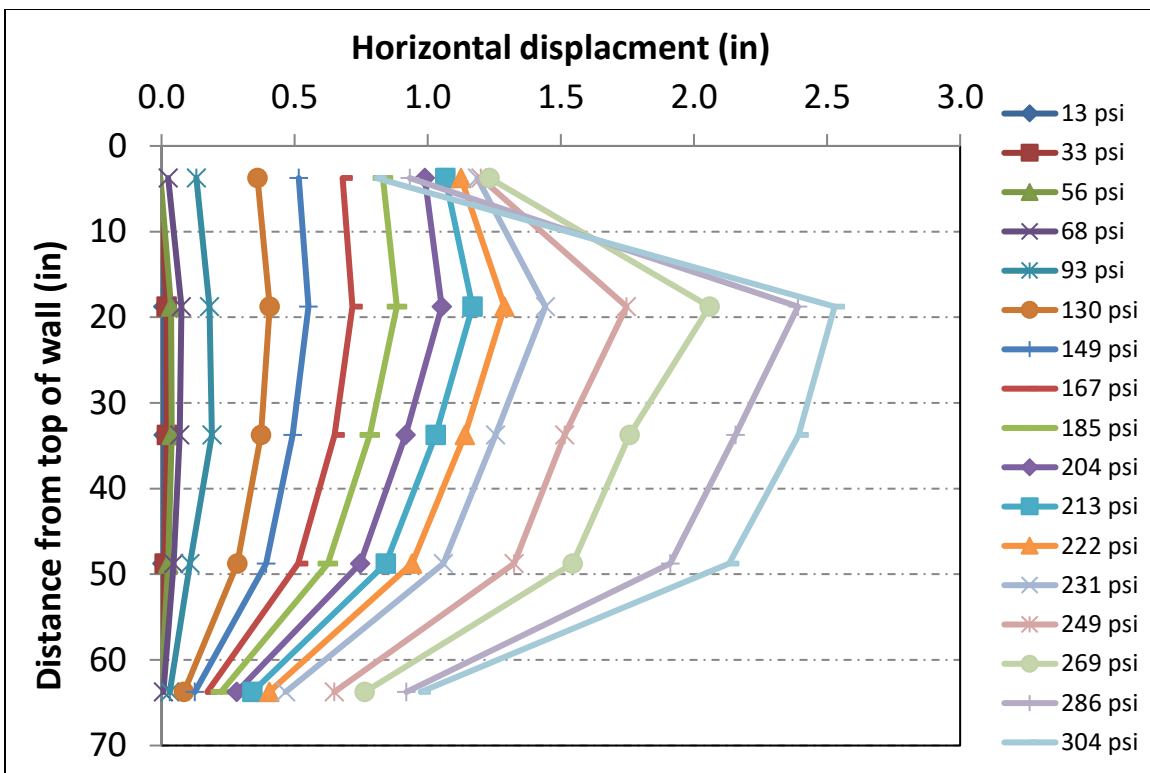


Figure 3-21 Lateral deflections along GRS pier height for TF-6.

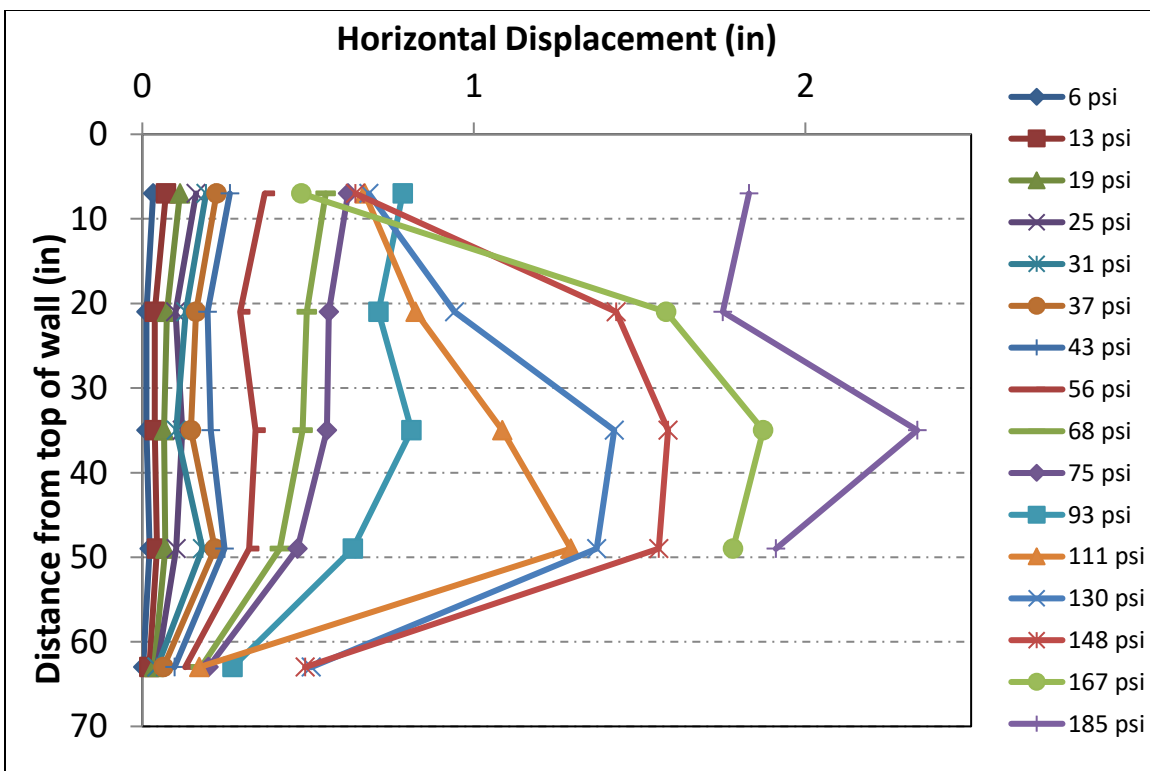


Figure 3-22 Lateral deflections along GRS pier height for TF-7.

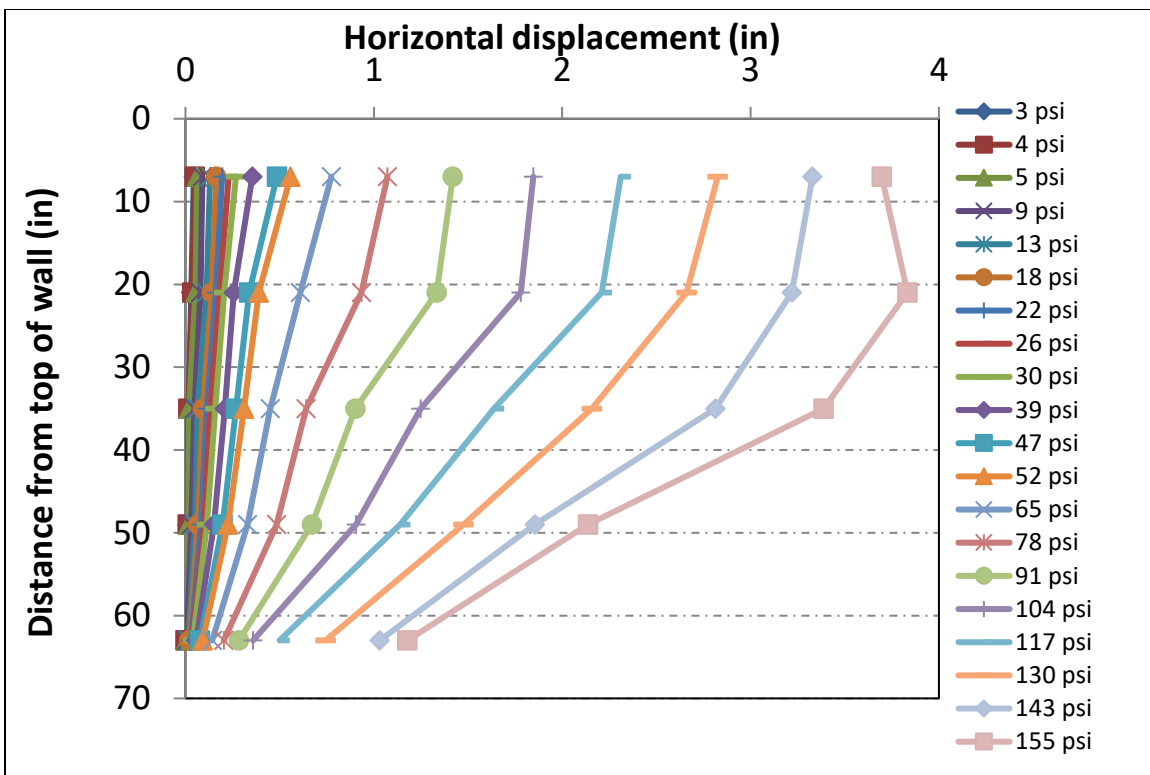


Figure 3-23 Lateral deflections along GRS pier height for TF-9.

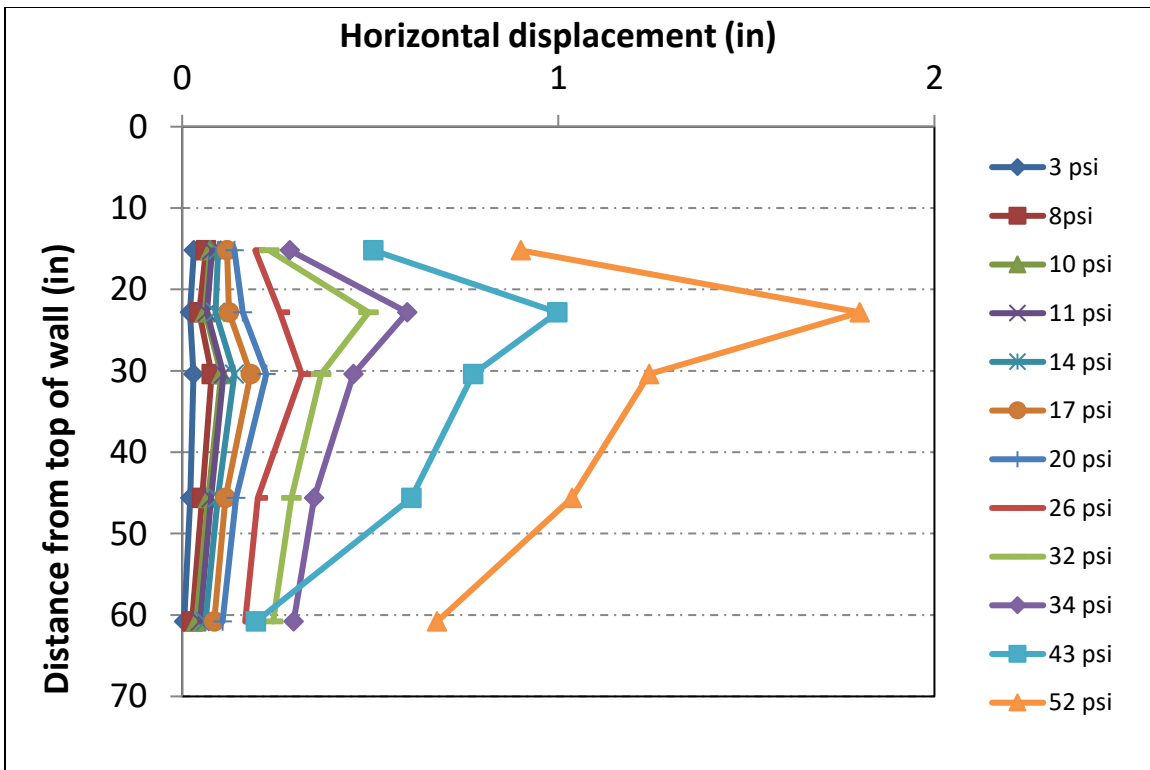


Figure 3-24 Lateral deflections along GRS pier height for TF-10.

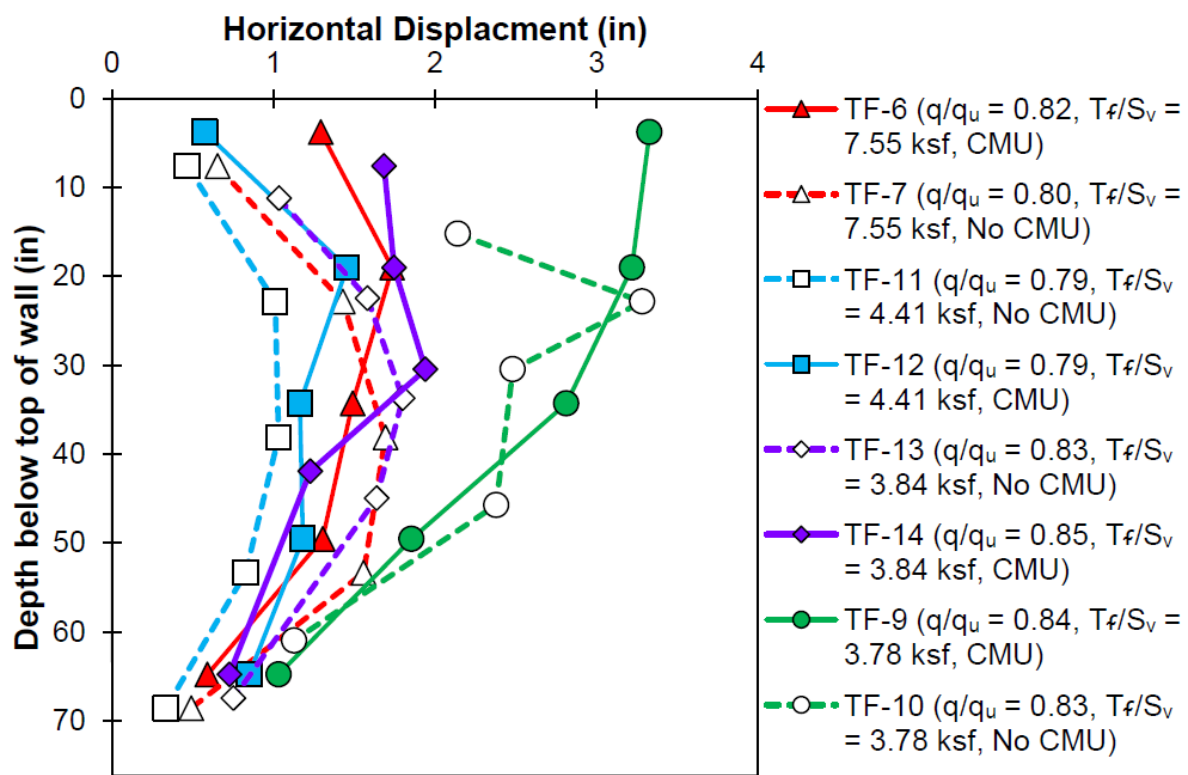


Figure 3-25 Lateral deformation profiles of GRS piers at approximately 83% of ultimate load capacity. (Iwamoto, 2014)

4. Model Input Parameters

4.1 Aggregate

Four consolidated drained (CD) triaxial tests and one isotropic consolidation (IC) test were performed by FHWA on the VDOT 21A aggregate backfill. The modeling performed in this study was conducted using Subloading t_{ij} parameters derived from these five tests. In addition, the suction estimation employed by Kaya (2016) was adopted for this study. The derivation and estimation of parameters is described below.

4.1.1 Test Results

4.1.1.1 Isotropic Consolidation

λ and κ are critical volume change parameters. They both can be obtained from an isotropic consolidation's virgin compression/normal consolidation line and unload-reload curve, respectively. The isotropic consolidation test of the aggregate backfill began with an initial mean consolidation stress of 5 psi. The isotropic stress was increased to 50 psi followed by unloading to 5 psi. This was followed by three cycles of reloading to 50 psi and unloading to 5 psi. In order to generate an e -log p graph, the volumetric strains measured during the isotropic consolidation test needed to be converted to void ratio. To calculate void ratio the following equation was employed:

$$\Delta e_v = -\frac{\Delta e}{1+e_0} \quad (\text{Eq. 4.1})$$

The calculated void ratios are plotted against the logarithm of mean stress in Figure 4-1 below. A feature of isotropic consolidation testing when conducted using a triaxial testing setup is membrane compliance (membrane penetration into the test specimen). The Newland and Allely (1959) approach was utilized to calculate membrane volumetric strain ($\epsilon_{vm} = \epsilon_T - 3\epsilon_a$). A correlation of membrane volumetric strain to horizontal stress was developed to perform the correction calculation (Figure 4-2). The results presented in Figure 4-1 are corrected values.

The calculated slope of the recompression lines (2.303κ) is 3.71E-3 resulting in $\kappa = 0.0016$. Calculation of λ was significantly less certain as the length of the normally consolidated line was quite short. The uncertainty of this value also results in a range of possible values for N (Reference void ratio at 1 atm). The values initially adopted for these parameters are those presented by Kaya (2016), $\lambda = 0.022$ and $N = 0.355$. These values are not adopted permanently but are used as initial guesses for optimization discussed in the following sections.

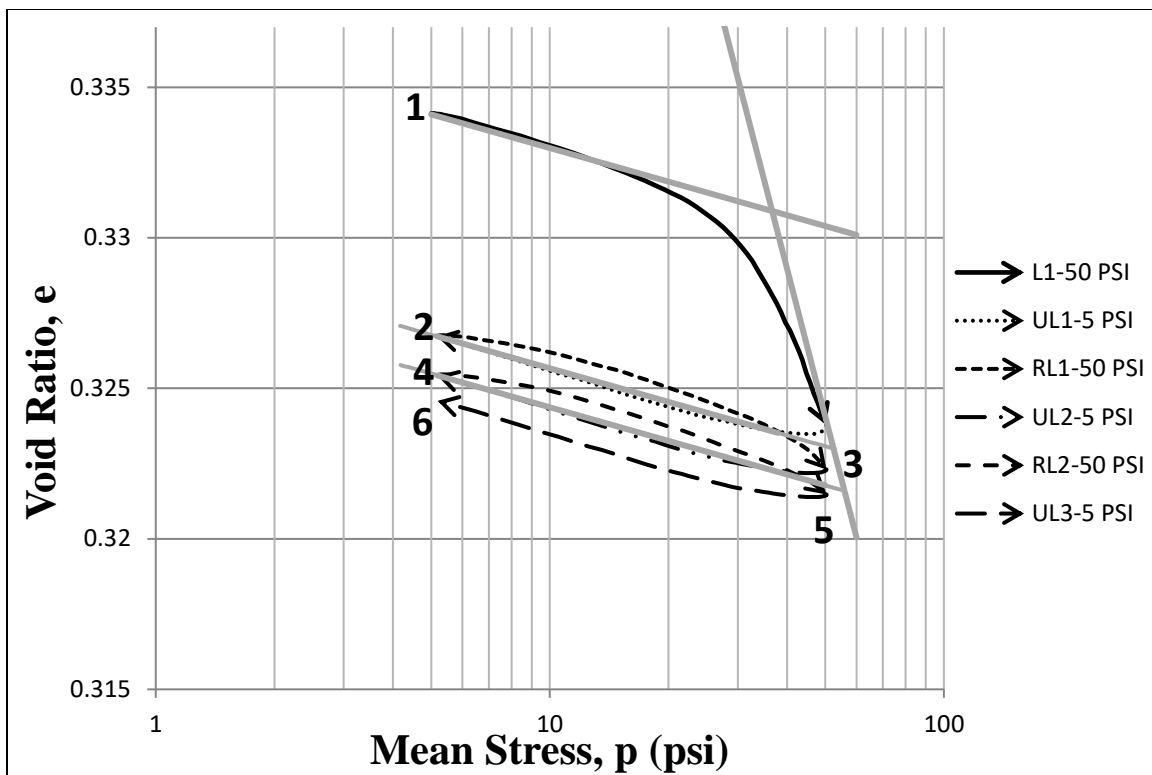


Figure 4-1 Results of isotropic consolidation testing, e - $\log p$ curve.

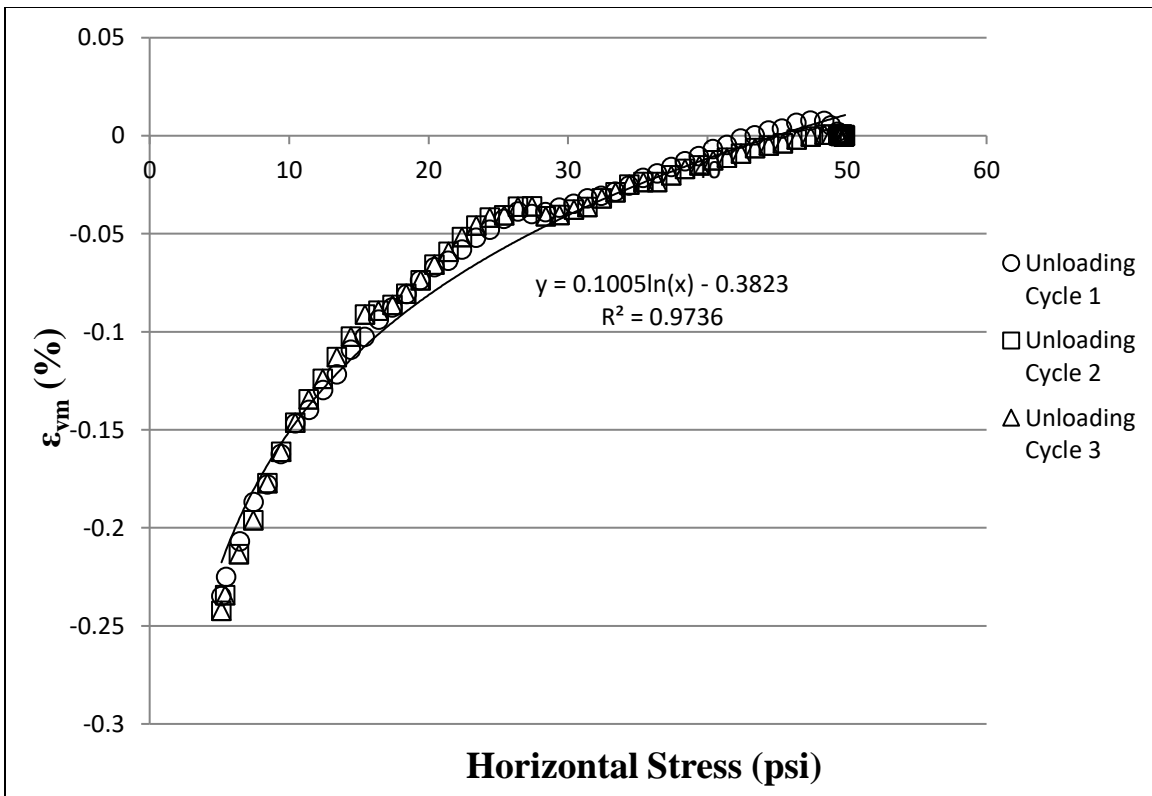


Figure 4-2 Membrane volumetric strain correlation with horizontal stress.

4.1.1.2 Drained Triaxial Testing

Four consolidated drained (CD) triaxial compression tests were conducted on the VDOT 21A aggregate backfill by FHWA at confining stresses (σ_3) of 5, 10, 20, and 30 psi (~34.5, 69, 138, and 207 kPa). Figure 4-3, Figure 4-4, and Figure 4-5 are deviator stress vs. axial strain, volumetric strain vs. axial strain, and stress ratio vs. axial strain, respectively.

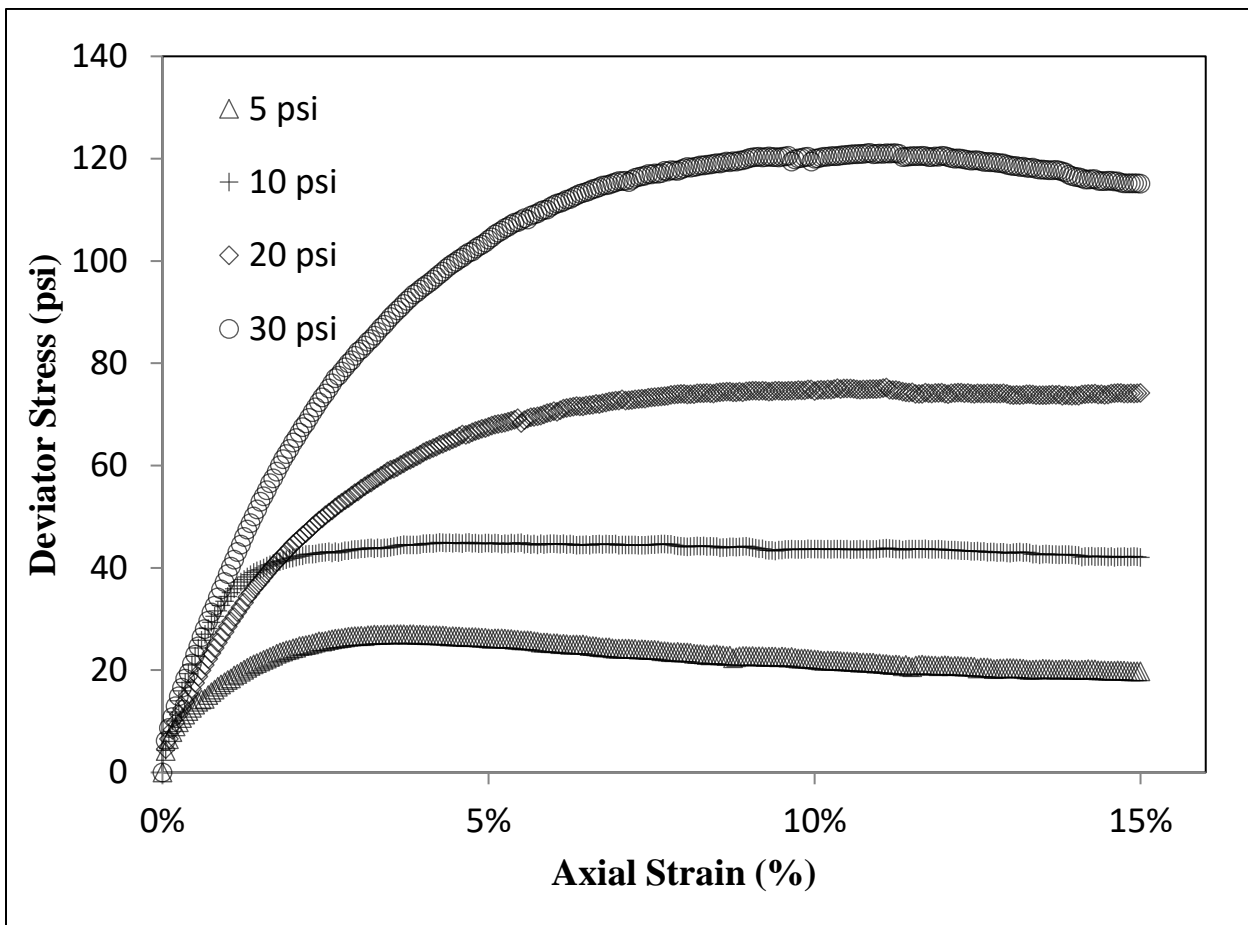


Figure 4-3 Deviator stress vs. axial strain from consolidated drained triaxial tests with $\sigma_3 = 5, 10, 20$, and 30 psi.

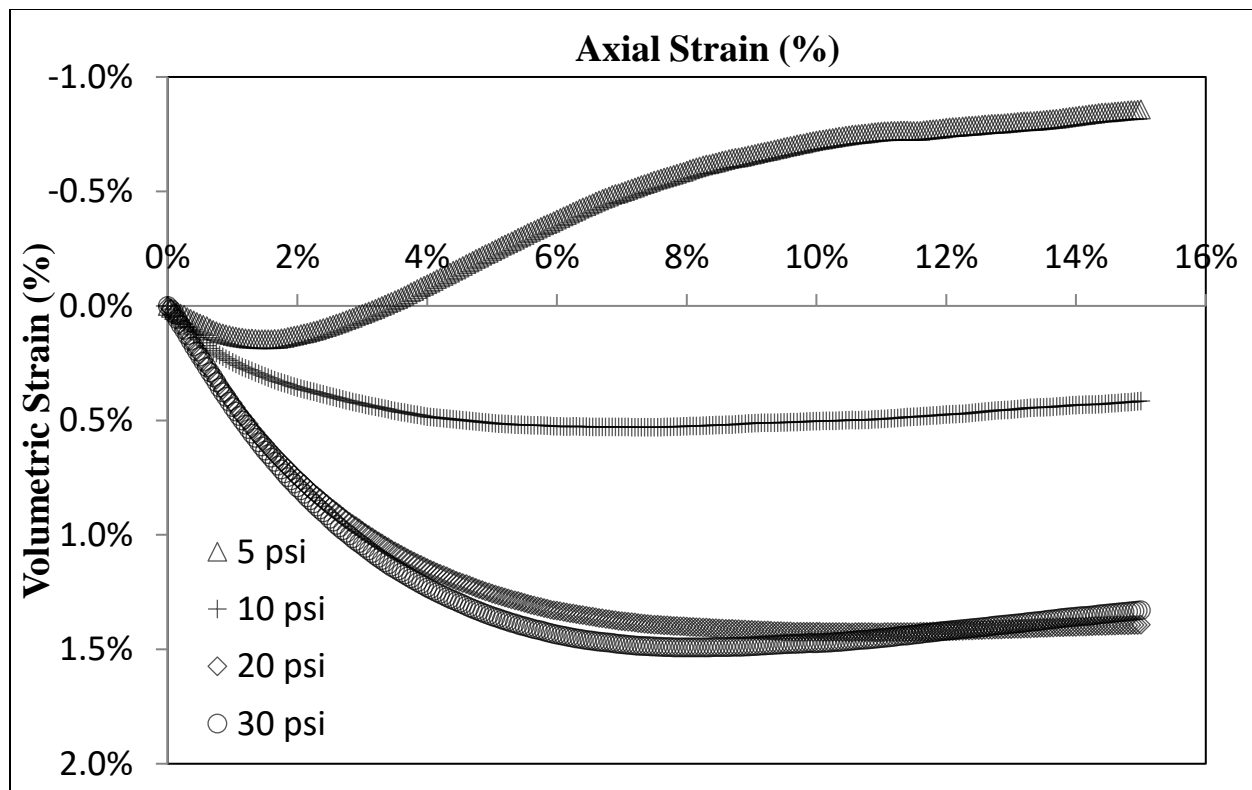


Figure 4-4 Volume change curves for consolidated drained triaxial tests.

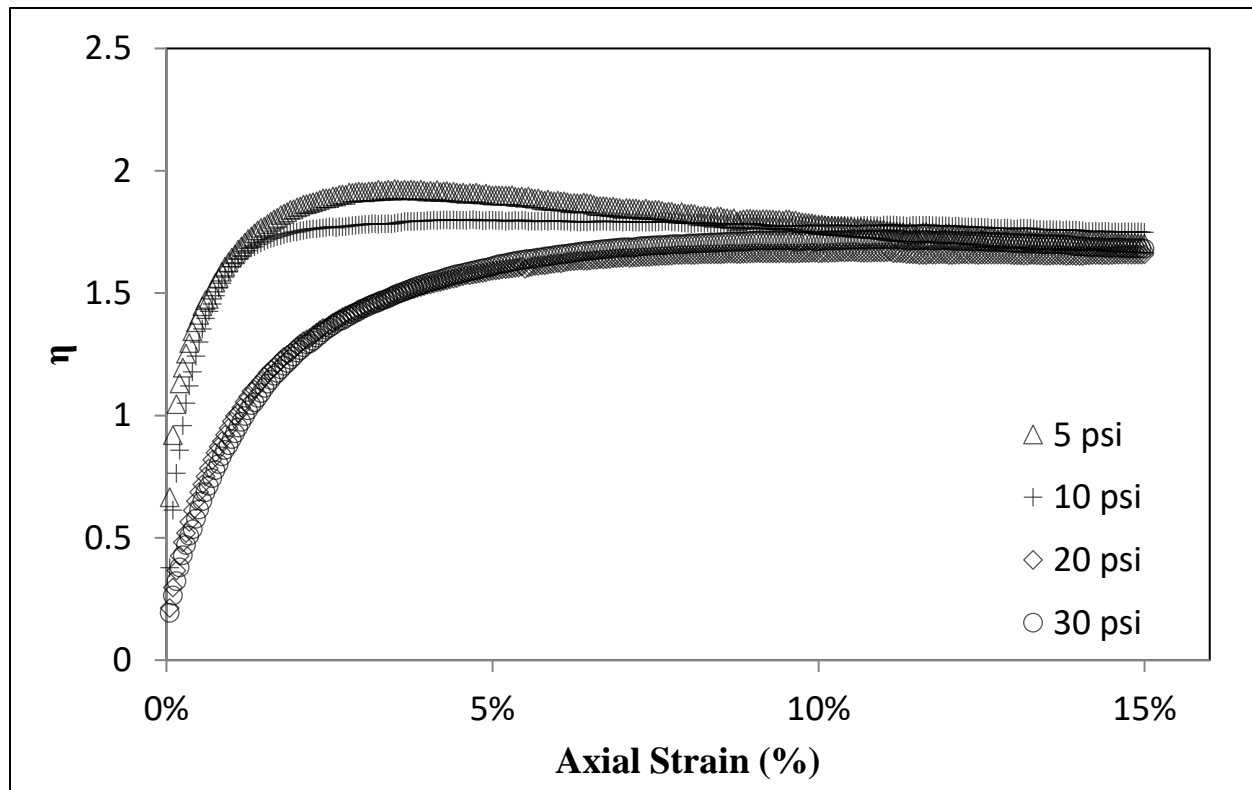


Figure 4-5 Stress ratio vs. axial strain curves for CD triaxial tests.

Figure 4-5 appears to show the stress ratios coalescing at approximately 15% axial strain, suggesting critical state has been reached or is close to being reached. $R_{cs} = \sigma_1 / \sigma_3$ vs. axial strain is shown in Figure 4-6 and is estimated to be 4.919 ± 0.2079 . By plotting void ratio vs normalized mean stress, we can see that the CD test with $\sigma_3 = 20$ psi (138 kPa) does not appear to reach critical state (Figure 4-7). We can also plot the critical state line using the final points of the CD testing results. The critical state line (CSL) in the e-log p state will take the form of (Roscoe & Burland, 1968):

$$e_{cs} = N - (\lambda - \kappa) \ln(2) - \lambda \ln\left(\frac{p_{cs}}{p_{ref}}\right) \quad (\text{Eq. 4-2})$$

where

e_{cs} is the critical state void ratio

p_{cs} is the critical state mean stress

p_{ref} is the reference (atmospheric) pressure

λ is the compression index and slope of the CSL

κ is the recompression index

Regression allows us to estimate the value of N and λ as 0.355 and 0.022, respectively. These values are taken to be initial estimates for these parameters as further optimization is described in the following sections. Because Figure 4-7 appears to imply that the CD test performed at $\sigma_3 = 20$ psi (138 kPa) did not reach critical state, the values of N and λ were estimated without considering the results from $\sigma_3 = 20$ psi. The value of R_{cs} when not considering the 20-psi test also deviates slightly, 4.990 ± 0.1866 . One final item of note regarding the CD triaxial testing was that testing was conducted at approximately 95% relative compaction (95% of the Proctor maximum dry density). A consequence of which, is a slight variation in the density (e_0) between tests. This is in contrast with the FHWA GRS pier tests which were conducted at 100% relative compaction.

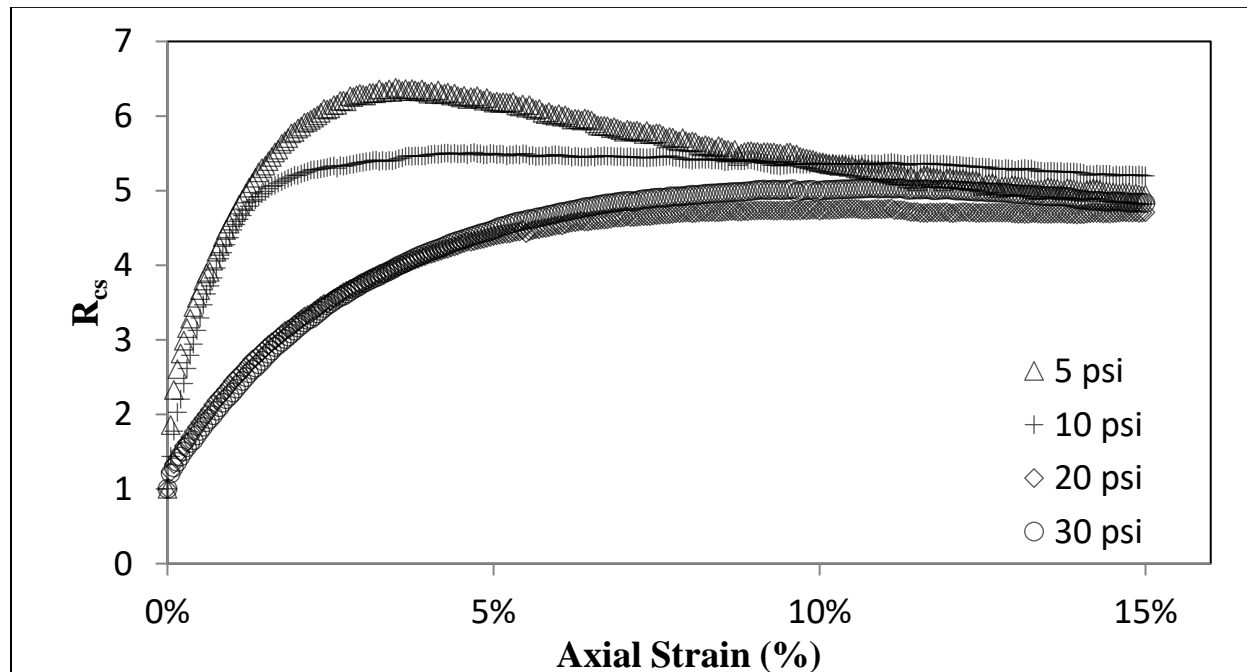


Figure 4-6 R_{cs} vs axial strain curves for CD triaxial tests.

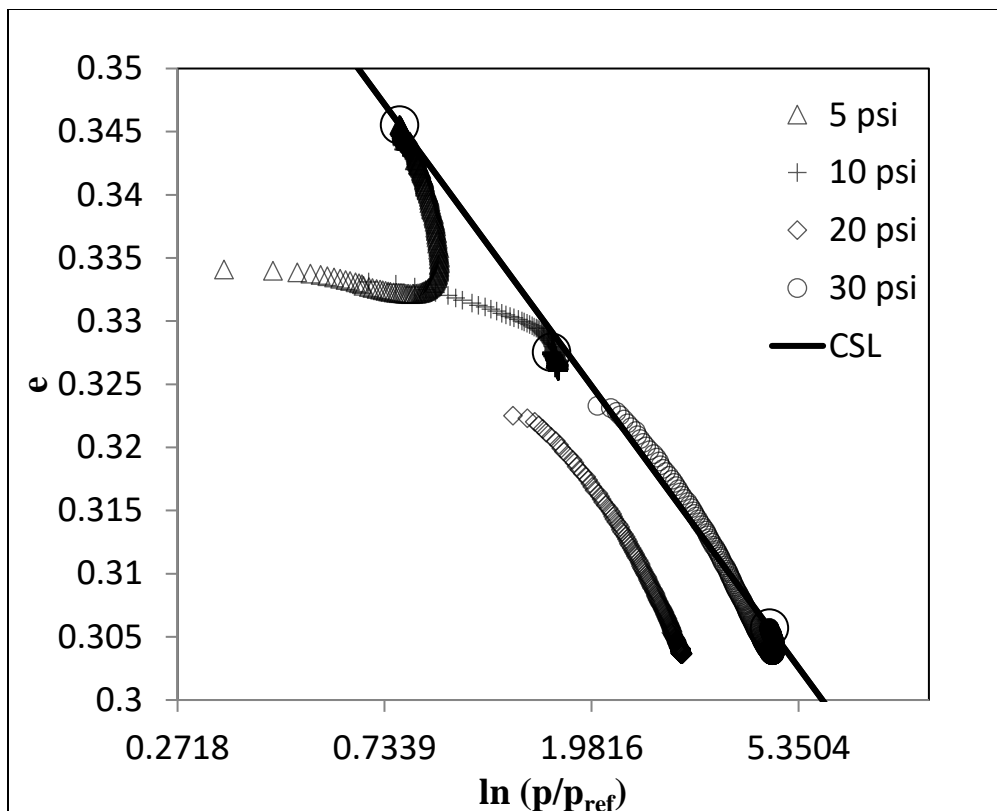


Figure 4-7 e - $\log p$ (volume change curves) for CD triaxial tests.

4.1.2 Subloading t_{ij} Model Parameters

Derivation of the Subloading t_{ij} model parameters followed 4 steps: (1) derivation of all relevant parameters possible from existing testing data using traditional means (2) create Python script to optimize “Subloading_Tij.exe” output to CD triaxial and isotropic consolidation testing data (3) attempt optimization using various combinations of iterable variables, error weighting, and selection of testing data (4) select optimization results based on observed results and statistical output. The first step has already been discussed in the preceding sections, but initial assumed values are tabulated here:

Table 4-1 Initial values of Subloading t_{ij} parameters derived directly from testing.

Parameter	Value	Source
λ	0.022	Consolidated Drained Triaxial Compression tests
	0.0016	Isotropic Consolidation test
R_{cs}	4.99	Consolidated Drained Triaxial Compression tests
	0.355	Consolidated Drained Triaxial Compression tests

Several parameter values required by the Subloading t_{ij} model are also assumed based on reasonable values. The majority of these are not iterated on and are kept constant during the optimization procedure. The values assumed to be constant during optimization are tabulated here:

Table 4-2 Constants assumed for Subloading t_{ij} model during optimization.

Parameter	Value	Description
ν	0.2	Poisson's Ratio
P_a	14.7 / 100	Atmospheric Pressure (psi / kPa)
e_{max}	0.551	Maximum Void Ratio
l_p	1.0	Power of Density Function
$powerIC$	2.0	Power of Function Determining Proportion of (IC) Components
wgt_{IC}	1.0	Proportion of the (IC) Component
$h^{p(soft)}$	1.0	Minimum Value of h^p in Softening Term
$Q_{\omega 0}, b_{\omega}, k_b$	0.0	Structured Behavior Parameters

With the exception of the Poisson's ratio and maximum void ratio, the values presented in Table 4-2 are constants assumed for Subloading t_{ij} model during optimization are adopted from Nakai (2013). These values are typical and are determined largely based on model selection. Poisson's ratio is taken to be 0.2 as this value is fairly consistent with the literature (Nakai, 2013; Kaya, 2016; Shen et al., 2019) and testing data. e_{max} is estimated to be 0.551. This estimate was obtained by considering several sources and estimates including Youd (1973), Pires-Sturm et al. (2022), and Cubrinovski and Ishihara (1999). e_0 values were supplied along with testing data.

There are six primary parameters that were iterated on during optimization: N , λ , β , a , k_a , and R_{cs} . Due to the uncertainty of N and λ when considering the isotropic consolidation behavior, an optimized value is also considered. β and a are the shape and density parameters discussed in Section 2.1 and require iteration to be estimated. k_a is the parameter that controls shear in the density evolution rule, appearing as a constant multiplier of X . Based on modeling experience and discussion with Dr. Nakai, a_{IC} and a_{AF} are assumed to be equal and are thus treated as one iterable parameter. R_{cs} is included as an optimization parameter due to the uncertainty presented when calculated using the CD triaxial test results discussed above. Several other combinations of iterable model parameters were explored with optimization results explored. Ultimately iteration of other parameters was dismissed due to concerns over whether the results were physically realistic. A short discussion of this concern is included in Section 4.1.4.

4.1.3 Machine Learning Implementation

The original framework utilized to perform the optimization was Scipy's optimization function. Early attempts quickly indicated that due to the limitations of the function, the Scipy implementation would be insufficient. The lmfit package was found as an alternative that would be able to handle the high dimensionality of the parameter vector and modality of the parameter space (Matt Newville, et al., 2023).

The lmfit package allows for the creation of a Model and Parameter class. Included in the Model class is an optimization function that allows for selection of an algorithm from a variety of local and global optimizers. Input data in the form of an array is optimized against using the defined Model and Parameter classes. The Parameter class contains variables and can be explored or held constant during

fitting. The variables can contain upper and lower bounds as well as be related to each other through algebraic expression. The Python code can generally be described using the following outline:

```
Import packages

*Error checking function converts model results to floats*

def SubloadingTijfn(parameter vector)

    with open('Para.txt', 'w') as para:
        para.write(Model Selection)
        para.write(parameters)
    para.close()

    with open('Path.txt', 'w') as path:
        path.write(stress path for first confining stress)
    path.close()

    os.system('r', 'C:\...\SubloadingTij_a.exe')

    temp = pd.read_fwf(calculation results)

    *Error checking*

    Results Array = temp
    *Repeat the above for all confining stresses and isotropic
    consolidation*

    Results = Results Array.flatten()

    Return Results

data = np.loadtxt("Triaxial and Consolidation Test Data.txt")

weights = np.loadtxt('weightsforfitting.txt')

parameters = ['parameter1', ..., 'parametern']

tijmodel = Model(SubloadingTijfn, param_names = parameters)

paramsin = tijmodel.make_params
(parameter1 = dict(value=initialvalue, max=maximum, min=minimum),
..., parametern = dict(value=initialvalue, max=maximum,
min=minimum))

emcee_kws = dict(algorithm keyword arguments)

Parameter_optimization = tijmodel.fit(data=data, params=paramsin,
method='emcee', fit_kws=emcee_kws)

print(Parameter_optimization.fit_report())
```

The emcee algorithm described in Section 2.4 is used to perform the optimization described by the code described herein. As the emcee algorithm is fairly sensitive to initial conditions, initial parameter values were found using the same code above but with the optimization performed by the differential evolution algorithm described in Section 2.4. This initial optimization allows for the second initialization approach described by Foreman-Mackey et al. (2013). By using partially optimized parameters as initial values we begin the walkers as a tight N -dimensional ball in parameter space near the point of maximum probability.

The emcee optimization requires a “burn-in” period specified by a number of algorithm walks during which shorter chains are sampled. During “burn-in”, hyperparameters are varied in order to create the fastest increase in the posterior function’s density while maintaining an acceptable sampling (Foreman-Mackey et al., 2013). The emcee algorithm produces a posterior density function that can be graphed as a series of joint probability distributions. The acceptance fraction of the walks during the specified “burn-in” is recorded and graphed for the distribution of walkers.

The number of walkers, the burn-in period, the number of walks (steps), and the weight of the error calculations were all varied manually. Several rules of thumb are provided by Foreman-Mackey et al. (2013) were utilized as a starting point including the number of walkers $\geq N^*10$ where N is the dimension of the posterior distribution, and burn-in $\geq 1/2$ of steps. Manual variation of these hyperparameters indicated that beyond a threshold value, further increases in these values (more walkers, longer chain, more burn-in) appeared to have a negligible effect.

Several error weighting schemes were considered as a clear issue regarding differential magnitude appears when considering multiple confining stresses. The results generated by the model will on average exhibit greater absolute error under the higher confining stresses. The larger stresses attained during testing will, by virtue of being larger, tend to result in larger model error. The result can be a false convergence of the higher confining stress and overfitting (i.e., finding a local minima). While global optimization algorithms (e.g., emcee and differential evolution) have built-in mechanisms that resist this tendency, the problem becomes two- and three-fold when considering the triaxial volume change curves and isotropic consolidation volume change curve. The difference between the modeled stresses and the isotropic consolidation void change is an order of magnitude while the difference between the modeled stresses and the triaxial volumetric strains is two orders of magnitude. This difference compounds the same issue occurring between the higher and lower confining stresses. There is an increased likelihood of overfitting parameters to the stress behavior while the volume change behavior is suppressed.

The Model class has a built-in weight function that can be employed during fitting. Employing data and error weighting has the possibility of mitigating the effects of large-magnitude overfitting. A logarithmic weighing scheme, a min-max normalization scheme, and a reverse sequential weighing scheme were employed. A description of each is included here:

- Logarithmic weighing scheme:

$$w_i = \begin{cases} \frac{1}{\log x_i} & \text{for } x_i \geq 1 \\ \frac{1}{|\log(1000 * x_i)|} & \text{for } x_i \leq 1 \end{cases}$$

(Eq. 4-3)

- Min-max normalization scheme:

$$w_i = 0.01 + \frac{x_i - \min(x)}{\max(x) - \min(x)} \quad (\text{Eq. 4-4})$$

- Reverse Sequential weighing scheme:

$$w_i = \frac{i}{\text{count}(x)} * (\max(x) - \min(x)) \quad (\text{Eq. 4-5})$$

where

x is the set of values for one testing metric (e.g., q , ε_v , or e) from a given test/confining stress

x_i is a given value in x

w_i is the weight of x_i

The input data (testing results) was imported using a .txt file. The document consisted of columns of testing data that was read into an array. The weights for each data point were calculated using a spreadsheet, exported as a .txt, and imported using the same methodology as the testing data. A copy of the Python code utilized to perform the optimization is available on [GitHub](#) for download and can be fairly easily modified to calculate Subloading t_{ij} model parameters for a given set of testing data. A copy of the Python code is also included in Appendix A below.

4.1.4 Parameter Optimization Results

The parameters that produced the statistically most probable result when compared to the CD triaxial and isotropic consolidation are listed here:

Table 4-3 Parameter Values from Optimization

Parameter	Value	Description
N	0.3576	Void ratio at reference pressure (1 atm)
λ	0.0207	Virgin compression index (slope of NC line)
β	1.0515	Yield function shape parameter
a	103.32	Density function parameter
k_a	1.0	Shear control parameter for density function
R_{cs}	5.0852	Principal stress ratio at critical state in triaxial compression

The optimized parameters in Table 4-3 and the values reported in Table 4-2 result in the following modeled CD triaxial and IC testing results:

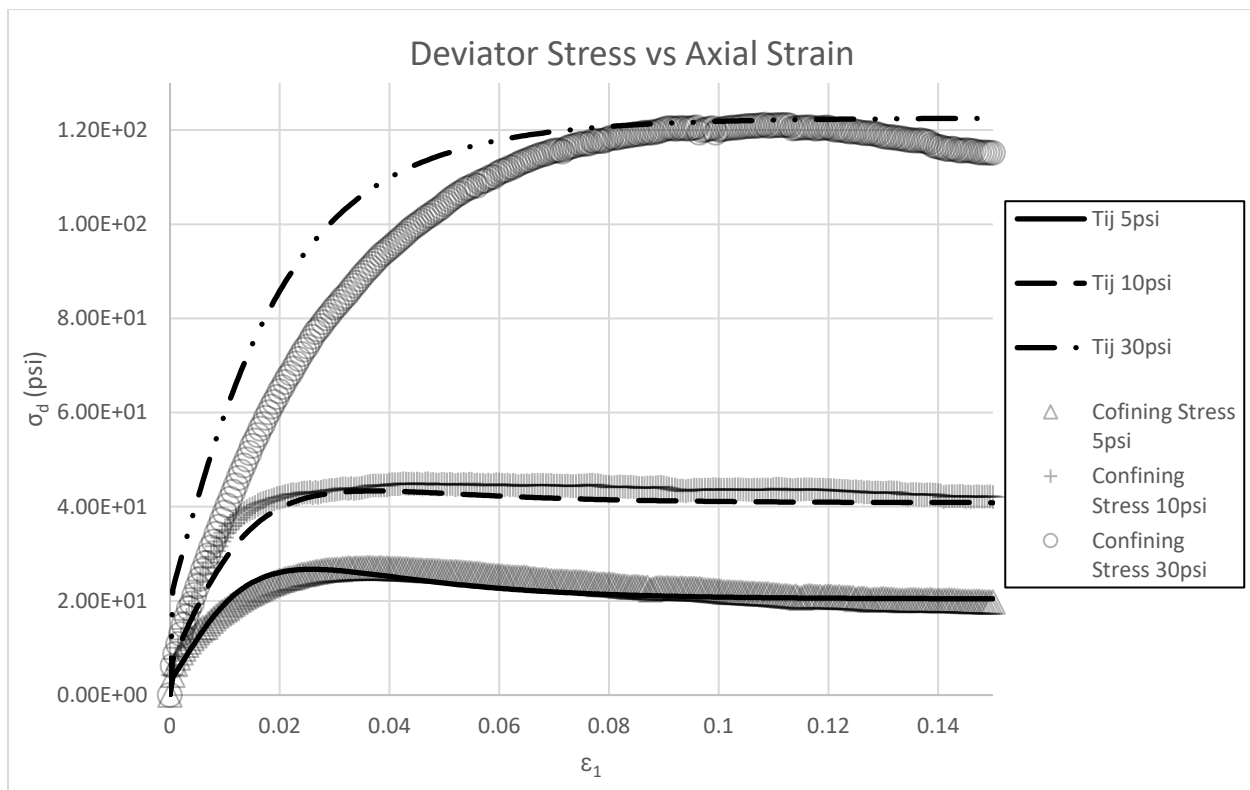


Figure 4-8 Stress-strain curves for triaxial tests from CD testing vs model simulation.

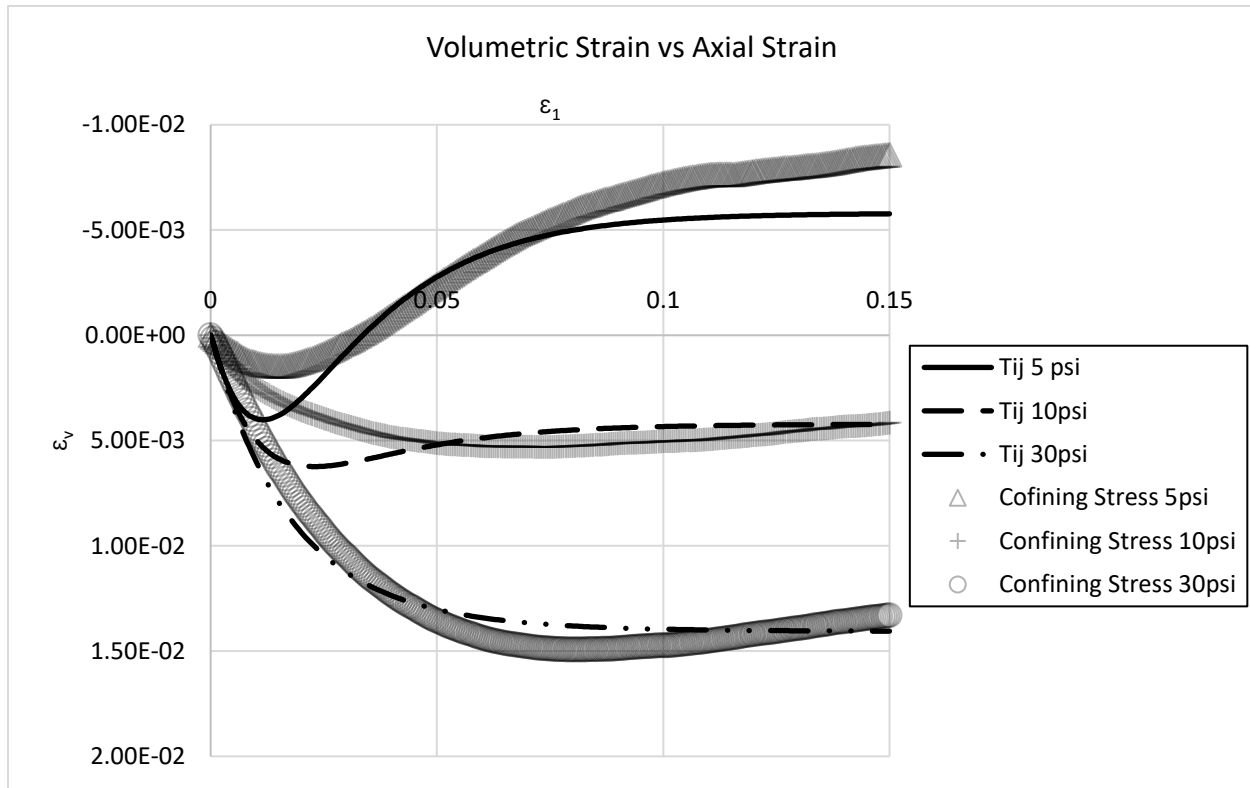


Figure 4-9 Triaxial volume change curves from CD testing vs model simulation.

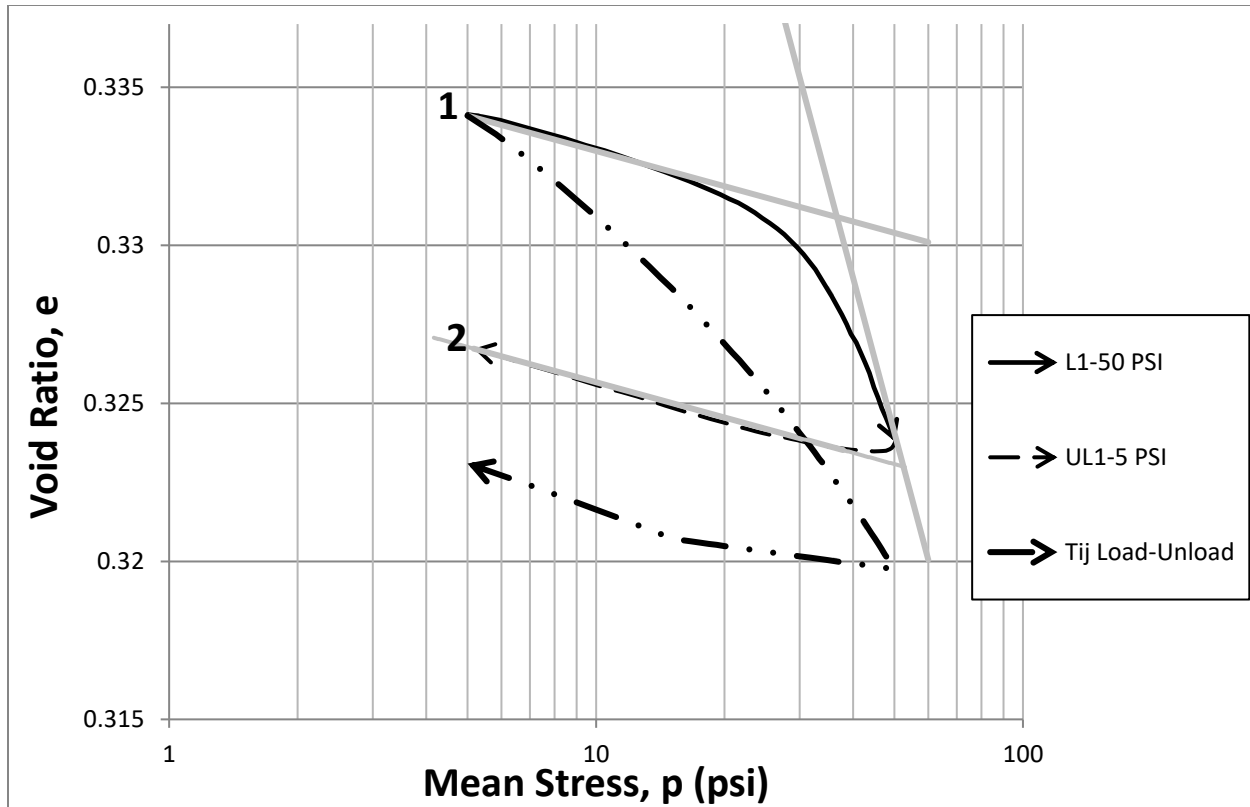


Figure 4-10 e - log p curve from IC testing vs model simulation.

The following descriptive statistics for each test metric (q , ε_v , and e) were generated along with the model results:

Table 4-4 Descriptive statistics for Subloading t_{ij} model optimization results.

Metric	R ²	R	CoV	RSS	C _v	RSS/CoV
$q (\sigma_3 = 5 \text{ psi})$	0.87149	0.93353	13.2681	776.467	0.16267	58.5215
$q (\sigma_3 = 10 \text{ psi})$	0.97273	0.98627	41.5877	1930.47	0.15394	46.4191
$q (\sigma_3 = 30 \text{ psi})$	0.96990	0.98483	667.609	37600.4	0.25723	56.3210
$\varepsilon_v (\sigma_3 = 5 \text{ psi})$	0.91773	0.95798	1.12E-05	8.19E-04	-0.77546	73.1438
$\varepsilon_v (\sigma_3 = 10 \text{ psi})$	0.11306	0.33625	3.22E-05	67.7767	1.26982	2104572
$\varepsilon_v (\sigma_3 = 30 \text{ psi})$	0.96699	0.98335	1.09E-05	2.26E-04	0.26772	20.6589
e	0.90187	0.94967	1.32E-05	0.10652	0.01109	8082.67
Average	0.82695	0.88519				
Average (w/o ε_v [$\sigma_3 = 10 \text{ psi}$])	0.92894	0.96362				

The first six rows are descriptive statistics for the CD triaxial results while the seventh row is for the IC results. The R² and R values of the modeled results imply fairly good agreement with the test results. The outlier is the volumetric strain under a confining stress of 10 psi. The difference in the average R² values when considering all test metrics versus when excluding volumetric strain at $\sigma_3 = 10$ psi, demonstrates that R² for ε_v ($\sigma_3 = 10$ psi) is the most significant outlier.

Visual inspection of the $\sigma_3 = 10$ psi triaxial volume change curves seems to indicate that the likely cause of the very low correlation is a combination of two factors. The first factor is the larger relative error of small axial strain ($<5\%$) range behavior. The second is the difference in the apparent concavity of the larger axial strain ($>5\%$) range. The testing results appear to be concave down in the large axial strain range while, because of slightly dilatant behavior, the modeled results appear to be concave up in the large axial strain range. If we solely consider the portion of ε_v corresponding to $\varepsilon_1 < 5\%$ when $\sigma_3 = 10$ psi, the resulting value of R^2 is 0.631. Considering $\varepsilon_1 > 5\%$ yields an R^2 of 0.443. This discrepancy makes sense as R^2 is a measure of correlation. For regions of data that have different concavities, the correlation is very low and even possibly negative. This is contrasted with the small strain region, in which the general shape of the modeled and test results is fairly consistent, but the error is relatively significant. This can be seen in the residual sum of squares (RSS) and the coefficient of variation (C_v) for the small strain range versus the large strain range. The small strain range has an RSS of 28.9332 and a C_v of 0.0471. This can be compared to the RSS and C_v for the large strain range, with values of 39.1094 and 0.0109, respectively. The smaller coefficient of variation for the large strain range indicates that there is less absolute variation between the modeled and testing results. Additionally, as the large strain range has twice as many data points as the small strain range, a large strain RSS that is only 135% of its small strain RSS results in a smaller average error per data point (0.19457 vs. 0.28647, respectively).

Optimization using the parameters above occurred after multiple iterations of optimizer configurations. Both the bounds (min-max) of the Subloading t_{ij} parameters as well as which parameters were optimized on, were considered during iteration. The largest and smallest values (within the bounds of physical feasibility) were chosen for the max and min values. This was done in an effort to ensure true global optimization. However, the unintended consequence was a tendency to find numerical quirks in the model and optimization algorithm, resulting in parameter values that either made little physical sense for the material (e.g., a Poisson's ratio of 0.45) or exhibited stress-strain behavior with very good agreement (a large resulting R^2 value) but had unrealistic volume change behavior that significantly differed from the testing results. The inclusion of additional parameters as variable during optimization tended to exacerbate this effect. Additionally, this tendency generally resulted in either an artificially inflated correlation or a significantly worse correlation. The final consequence of the optimization of additional parameters is an increase in χ^2 , the Akaike information criterion, and the Bayesian information criterion. The increase in the Akaike information criterion and the Bayesian information criterion reflect the tendency for inflated correlation and are indicative of an overfitting tendency. The increase in χ^2 reflects an overall increase in "error" and is indicative of the significant failure to capture volume change behavior despite slightly better modeling of stress-strain curves.

Correlation plots below visualize the correlation for each metric described in Table 4-4 above. In addition, the corner plot below projects the posterior distribution onto a series of bivariate distributions allowing the posterior correlations to be visualized. The following plots were generated from the optimization process and using optimized modeled results:

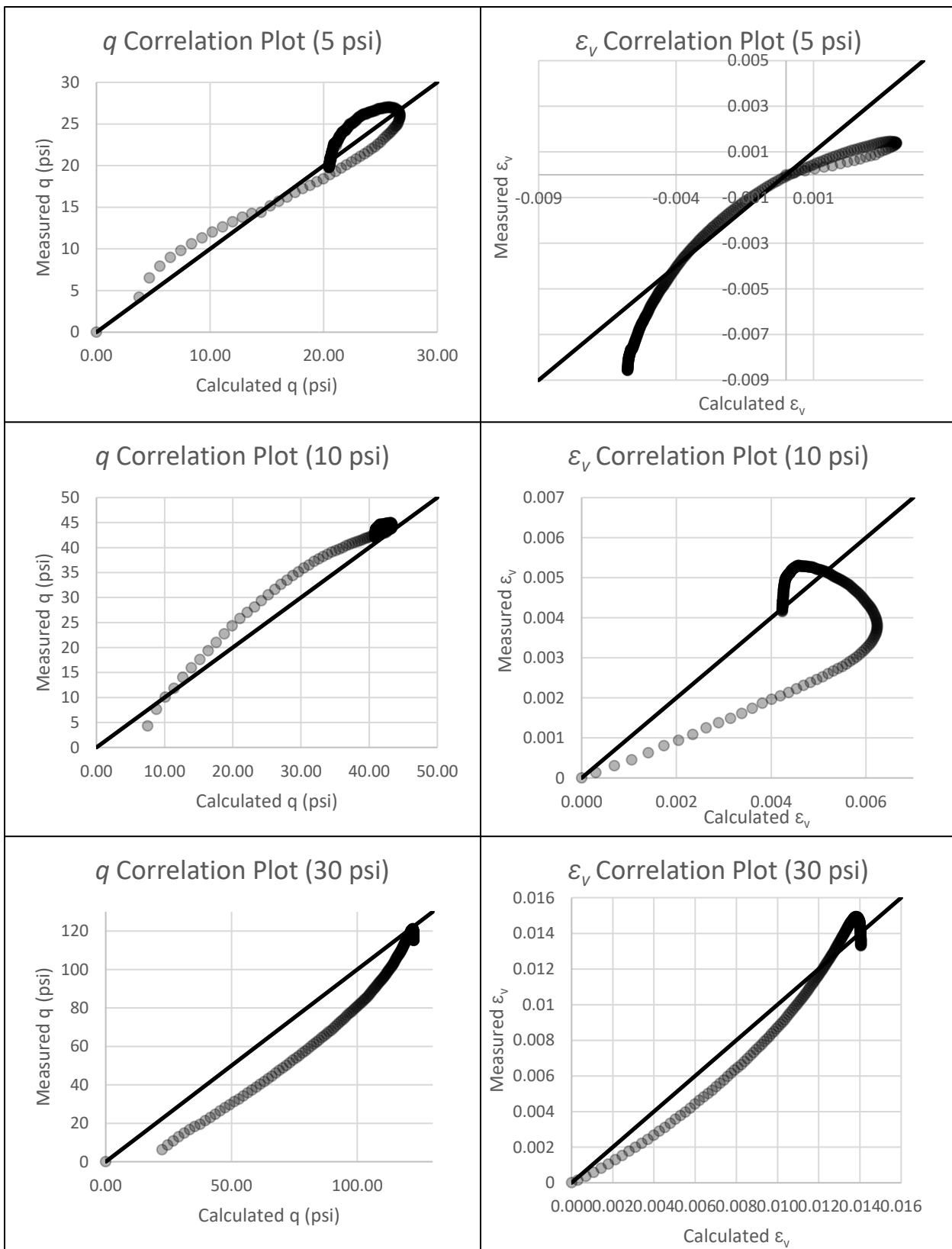


Figure 4-11 Correlation plots for triaxial tests: Top Left - q at $\sigma_3 = 5$ psi; Top Right - ε_v at $\sigma_3 = 5$ psi; Center Left - q at $\sigma_3 = 10$ psi; Center Right - ε_v at $\sigma_3 = 10$ psi; Bottom Left - q at $\sigma_3 = 30$ psi; Bottom Right - ε_v at $\sigma_3 = 30$ psi

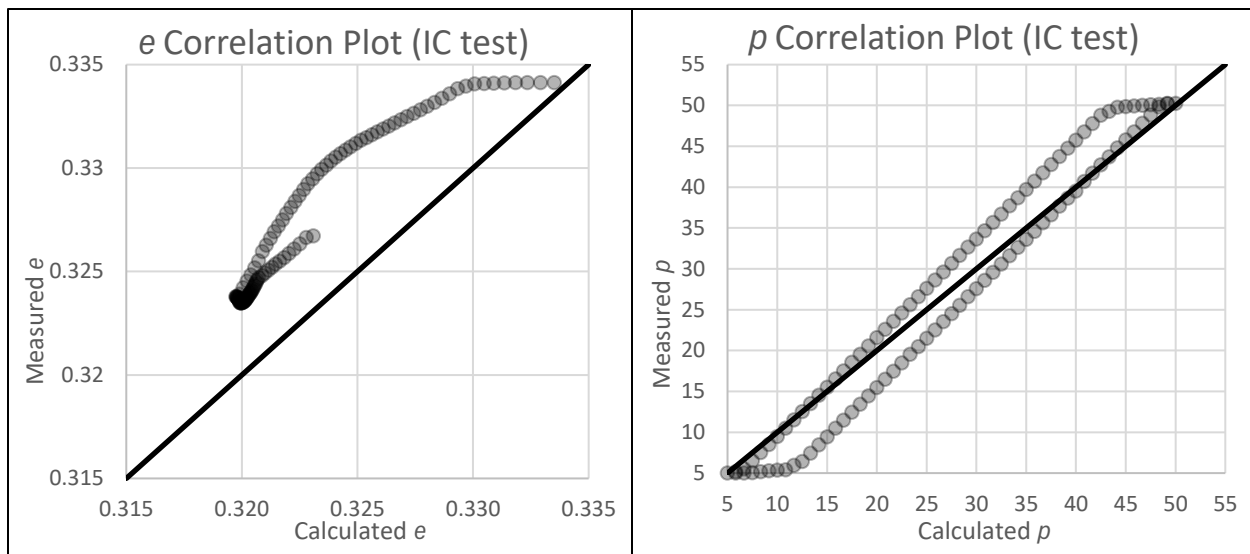


Figure 4-12 Correlation plot for IC test: Left - e; Right - p

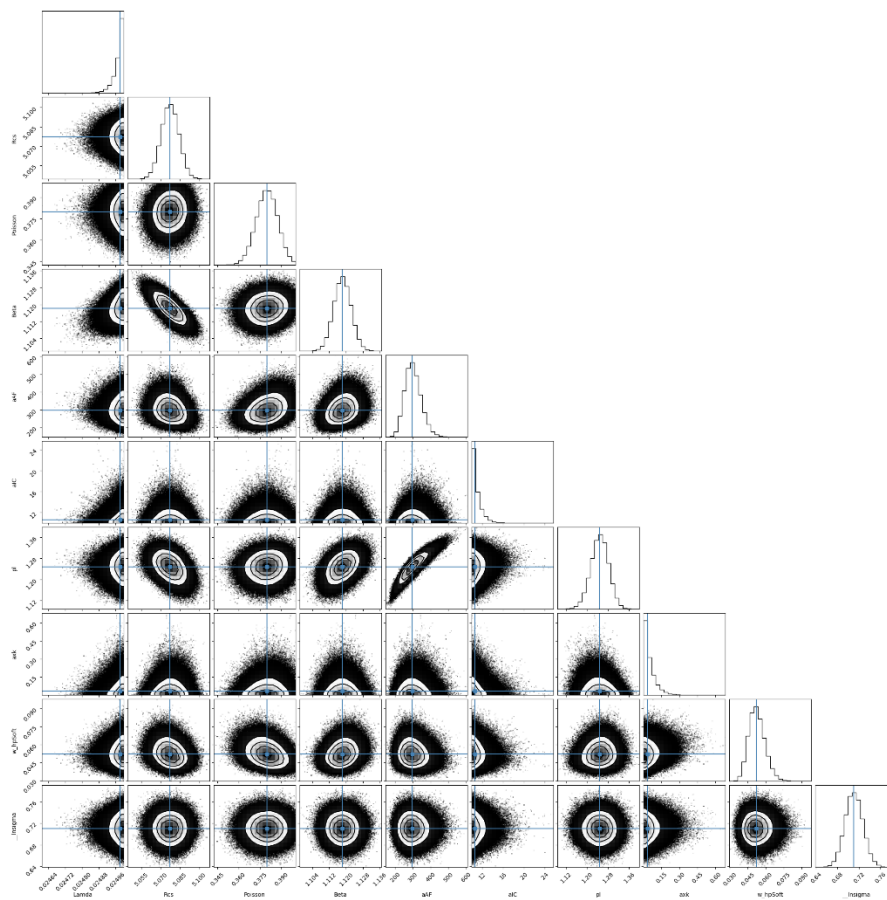


Figure 4-13 Simplified corner plot for optimization using just volumetric testing data.

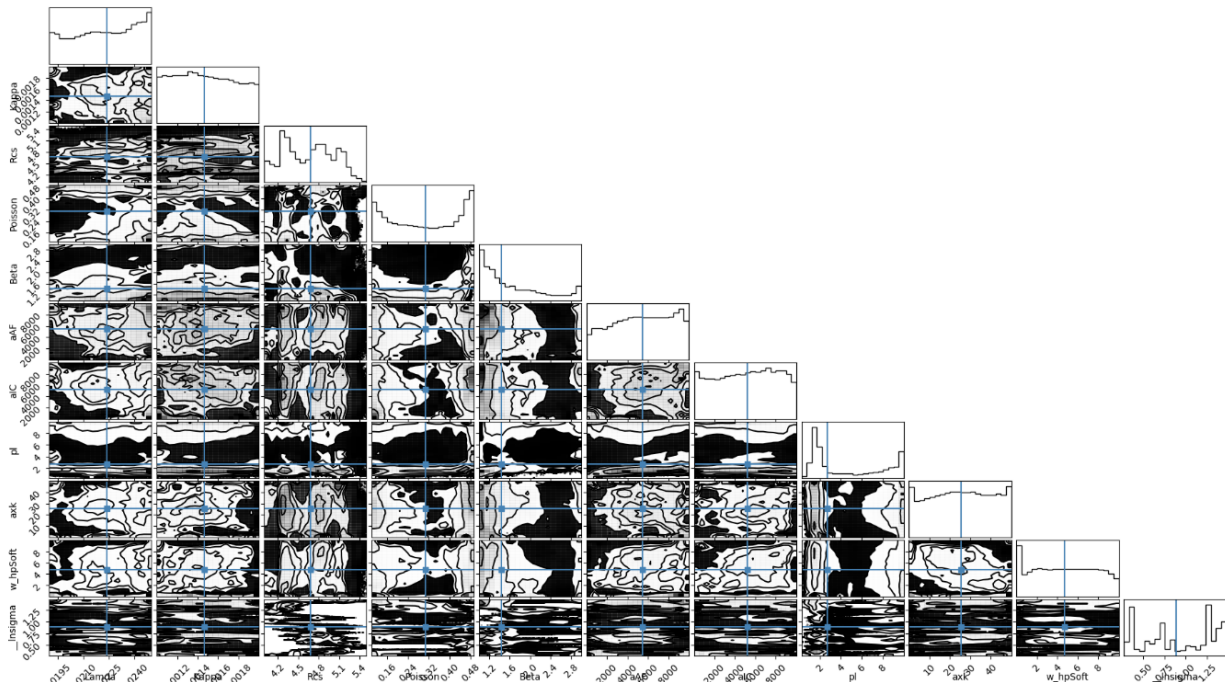


Figure 4-14 corner plot for optimization using triaxial testing data.

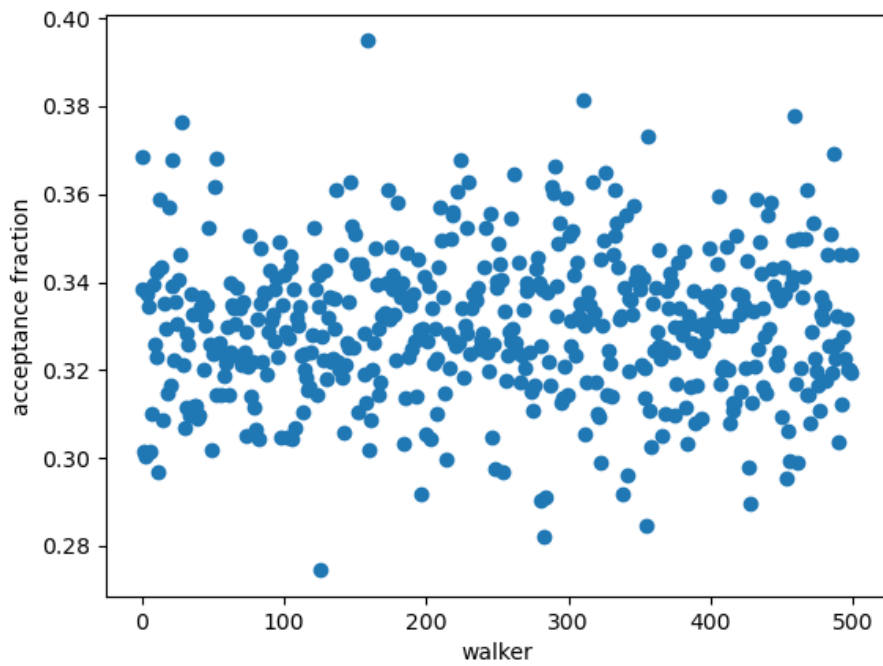


Figure 4-15 Acceptance fraction for the emcee optimization procedure.

Figure 4-11 above shows the correlation plots for the triaxial testing optimization while Figure 4-12 shows the plots for the isotropic consolidation test. Calculated (modeled) results are on the horizontal axes while the measured (testing) results are on the vertical axes. Figure 4-13 and Figure 4-14 are corner plots (bivariate projections of the posterior distribution) from two optimization attempts

using the same parameter iteration and initialization. Figure 4-15 plots the acceptance fraction for all the walkers in the ensemble.

The correlation plots graphically demonstrate the R^2 value, showing regions in which greater/lesser model and testing correlation exists. The plots indicate which stress states over- and underestimate the stress-strain behavior, with clear corollaries to the descriptive statistics in Table 4-4 arising. Namely, the C_v values presented appear to be consistent with the results shown in the correlation plots. Lower C_v values indicate better agreement, with the value being a measure of the orthogonal distance from the 45° diagonal (direct correlation line).

The parameter corner plots are bivariate plots of the maximum likelihood posterior distribution, i.e., bivariate plots showing the most likely model parameter values required to produce the testing results. The black portions are less likely with contour lines indicating the increasing likelihood transitioning into the white sections. These plots demonstrate the difficulty of optimizing this particular model. Both plots represent optimization attempts in which the same parameters were optimized with the same initial values, the sole difference is the quantity of testing results optimized with. The first plot (Figure 4-13) represents an optimization attempt in which only the triaxial volume change testing data was used to run the algorithm. The resulting posterior distribution, while anisotropic in locations, is fairly regular with the only apparent issue being that maximum likelihood may occur out of bounds for three of the parameters. The second plot (Figure 4-14) represents an optimization attempt in which all triaxial testing data was used to run the algorithm. The result is a highly complex, multi-model, anisotropic, and highly variable posterior distribution. Parameter space with complex behavior requires more computational resource allocation to sufficiently sample the posterior distribution.

The acceptance fraction plot displays the portion of accepted walks during the emcee algorithm for each walker in the ensemble. Foreman-Mackey et al. (2013) recommend that acceptance falls between 20 and 50% (0.2 to 0.5). The range of approximately 0.28 to 0.4 shown in Figure 4-15 falls squarely within the recommendation. The acceptance fraction falling within the recommended range indicates well-tuned hyperparameters. The acceptance fraction is a metric that indicates the quality of the running algorithm but does not however indicate the quality of the samples obtained or if sufficient sampling has occurred to properly map the posterior distribution. To judge whether a “success” condition has been reached and the posterior distribution has been sufficiently sampled, the autocorrelation time must be established. If there have been sufficient steps, the autocorrelation time (Eq. 2-76 through 2-78) will have been reached for all parameters. If the autocorrelation condition is not reached, either additional walkers can be added to the ensemble or additional steps can be performed (or some combination thereof). A truly global optimization will only be obtained if the autocorrelation condition is reached, and the acceptance fraction falls within an acceptable/sensible range.

4.2 Geosynthetics

The behavior of geosynthetics is generally assumed to be elastic/viscoelastic or elastoplastic. For this study, we have assumed elastoplastic geotextile behavior. Geosynthetics are treated as 2-D structures described by biaxial area normalized stiffness (EA_1 and EA_2) and in-plane shear stiffness. This load-deformation relationship is predicated on the fact that uniaxial tension testing is commonly expressed as load/width vs. strain. The resulting elastic moduli per unit thickness is alternatively expressed as wide-

width tensile strength, T_f , and failure strain, ε_f . The biaxial area normalized stiffness (EA) can be expressed by dividing T_f by the elongation at failure, ε_f .

The resulting EA_1 and EA_2 are based on ε_f values of 10% and 8% as listed in Figure 3-8. EA_1 and EA_2 are calculated to be approximately 876 kN/m and 701 kN/m, respectively. As the geotextiles were placed in an alternating pattern, the stiffness might be approximated as an average of the two values with EA_{avg} approximately equal to 789 kN/m. To model elastoplastic behavior, PLAXIS 3D requires the input of the wide-width tensile strength (alternately labeled $N_{p,1}$ and $N_{p,2}$) to describe the failure strength. PLAXIS 3D utilizes a custom elastic-perfectly plastic constitutive model to simulate geotextile behavior. Upon failure of a node in the mesh, stress is redistributed according to a perfectly plastic associated flow rule.

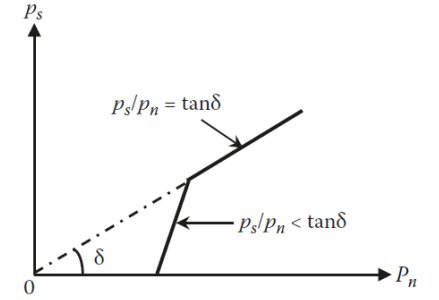
4.3 Interface Elements

There are two interfaces modeled during this study, geotextile-soil and footing-soil. The interfaces are generally modeled using a Mohr-Coulomb constitutive model. Interface behavior is largely governed by frictional interaction values, thus both a normal and a shear stiffness are defined.

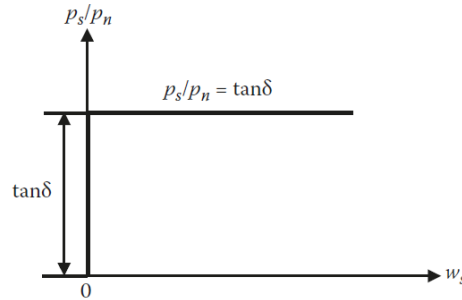
The geotextile-soil and footing-soil parameters are adopted largely from a combination of soil parameters and previous experience. Normal and shear stiffness (k_n and k_s) when employing the Subloading t_{ij} model are intended to reproduce the interface behavior described by Goodman et al. (1968) as shown in Figure 4-16 is utilized. The Geo-Research Institute, who partnered with tij地盤解析研究会, performed extensive numerical simulation using the Subloading t_{ij} model and presented recommended values for k_n and k_s (100E6 kN/m³ and 9.09E6 kN/m³, respectively). These values are intended to produce the Goodman et. al. (1968) interface behavior.

In addition to k_n and k_s , the interface model implementation in PLAXIS 3D also requires a friction angle, elastic modulus, poisons ratio, cohesion, and dilatancy angle. The cohesion and dilatancy angle are assumed to be zero as no “stickiness” or dilatant behavior is expected between unbonded surfaces. As interfaces are 2-D elements, Poisson’s ratio is assumed to be zero indicating no change in thickness. As all interfaces are assumed to be of negligible thickness, all interfaces are assigned a Poisson’s ratio of 0. When a material is assigned to an interface element in PLAXIS 3D and the **Direct** option is selected, the interface moduli (E_i and G_i) is supplanted by k_n and k_s instead of derived. A “dummy” value of 100E3 kN/m² for E_i is input to allow for a valid model but is not used during calculation. As the value isn’t used during calculation, the same dummy value is used for all interfaces in the model.

Establishing applicable friction angles is based on utilizing both the large-scale direct shear testing results (Figure 3-5) and the CD triaxial testing results (4.1.1.2). Interface reduction factors (R_{inter}) not only reduce the provided friction angle but also the elastic properties in PLAXIS 3D. To avoid this effect, a reduced friction angle is employed with an R_{inter} value of 1. The Nicks et al. (2013) reported friction angle for the large-scale direct shear test is 54°. The calculated peak friction angle for the CD triaxial tests is 40.814° based on a Mohr-Coulomb failure envelope. As the large-scale and forced failure plane nature of the GRS pier is likely the governing behavior of the soil-involved interfaces, the large-scale direct shear test value was utilized for these interfaces.



(a) Relation between normal stress (p_n) and shear stress (p_s)



(b) Relation between relative displacement (w_s) and stress ratio (p_s/p_n)

Figure 4-16 Idealized interface behavior (Nakai T., 2013).

Martin et al. (1984) indicate that geosynthetic-soil interface friction angles for sands on geotextiles range between 77% and 87% of the soil's peak friction angle. The larger grain size of the VDOT 21A material relative to a sand implies that a value on the higher end of the range or at the maximum, is appropriate. Conversely, the opposite is implied by the lower peak friction angle exhibited during triaxial testing. As these factors contradict, an approximately average value was selected at 81.5% (44°) of the soil peak friction angle. A similar approach was utilized when modeling the footing-soil interface. Typical values of the fraction of peak soil friction angle for the footing as suggested by the FHWA range between $\frac{2}{3}$ and 1 depending on the roughness of the concrete. A value of $\frac{3}{4}$ (40°) was selected based on an assumed use of wood forms (as opposed to metal) resulting in slightly rougher surfaces.

4.4 Summary

The following table is a summary of the material parameter values described above and used during modeling:

Table 4-5 Summary of material properties used during PLAXIS 3D modeling.

Aggregate Backfill		
Parameter	Value	Units
λ	0.0207	-
κ	0.0016	-
R_{cs}	5.0852	-
N	0.3576	-
β	1.0515	-

a	103.32	-
k_a	1.0	-
v	0.2	-
e_{max}	0.551	-
CMU Facing		
Parameter	Value	Unit
γ	12.51	kN/m ³
E_{ref}	21.3	GPa
ϕ	0	°
ψ	0	°
c_{ref}	10.1	MPa
f'_t	2,652	kPa
Geotextiles		
Parameter	Value	Unit
EA_1	876	kN/m
EA_2	701	kN/m
Tf	70.05	kN/m
Interface (Geotextile-Soil)		
Parameter	Value	Unit
k_n	$100.0 * 10^6$	kN/m ³
k_s	$9.09 * 10^6$	kN/m ³
v	0	-
ϕ	40	°
ψ	0	°
c_{ref}	0	kPa
Interface (Footing-Soil)		
Parameter	Value	Unit
k_n	$100.0 * 10^6$	kN/m ³
k_s	$9.09 * 10^6$	kN/m ³
v	0	-
ϕ	44	°
ψ	0	°
c_{ref}	0	kPa

5. Numerical Modeling

PLAXIS 3D and a user-defined Subloading t_{ij} .dll were utilized to model the TF-7 and TF-10 GRS piers. The .dll was supplied by tij地盤解析研究会 in collaboration with PLAXIS Japan. Shen et al. (2019) demonstrated the necessity of performing GRS modeling using 3D analysis. To that end, a strictly 3D analysis was conducted. The modeling setup is described in the following sections.

5.1 PLAXIS 3D Model Input

The domain geometry is input as solely the soil portion of the pier and does not include the construction facing. 10 layers of aggregate backfill were input into a central “borehole” using the Subloading t_{ij} parameters from Table 4-5 (Figure 5-1). The backfill is treated as a drained media with a unit weight of approximately 23.00 kN/m³. A groundwater level at the bottom of the pier was input; thus, the soil was treated as dry. The initial void ratio was taken to be 0.245 based on the iteration performed by Kaya (2016).

Calculation of the K_0 values was performed using a modified version of the optimization Python code discussed in Section 4.1.3. A copy of the code can be found on [GitHub](#) and is included in Appendix B. The code utilizes the SciPy minimize scalar function and iteratively calculates a void ratio prior to compaction based on the initial void ratio (before loading). The code utilizes the stress path of each lift of backfill during construction to optimize the void ratio input into the “Subloadingtij_a.exe” program. Once the void ratio prior to compaction is found, the code calculates a K_0 value for each lift based on their individual stress history.

Once the soil profile was input, the geotextile reinforcement was input (Figure 5-2). The geotextile layers were input under as a “geogrid” using the properties shown in Table 4-5. For TF-7, the geotextile layers were inserted between each interface between the 10 layers of aggregate backfill. For TF-10, the layers were inserted at every other interface. To create the geotextile geometry, a “surface” is inserted. The surface allows for the creation of the geotextile and the positive and negative (relative to the normal) interfaces. The interfaces were given the parameter values from Table 4-5.

“Volumes” were input during the initial stage to model the confining stress provided by the construction facing (Figure 3-7). The volumes were subsequently removed and a non-loading step was included to model the behavior of the removal of the facing and trimming of the geotextile. Between the volumes and the aggregate backfill, a horizontal and vertical confining load was placed to mimic the confinement provided by unsaturated suction (Figure 5-3). A value of 2 kPa was used based on Kaya’s (2016) estimates.

A “rigid” plate was used to model the loading footing. The plate was treated as linearly elastic and given an elastic modulus of 3.0E11 kPa and a Poisson’s ratio of 0. A negative interface was added between the footing and soil with the properties from Table 4-5 (Figure 5-2).

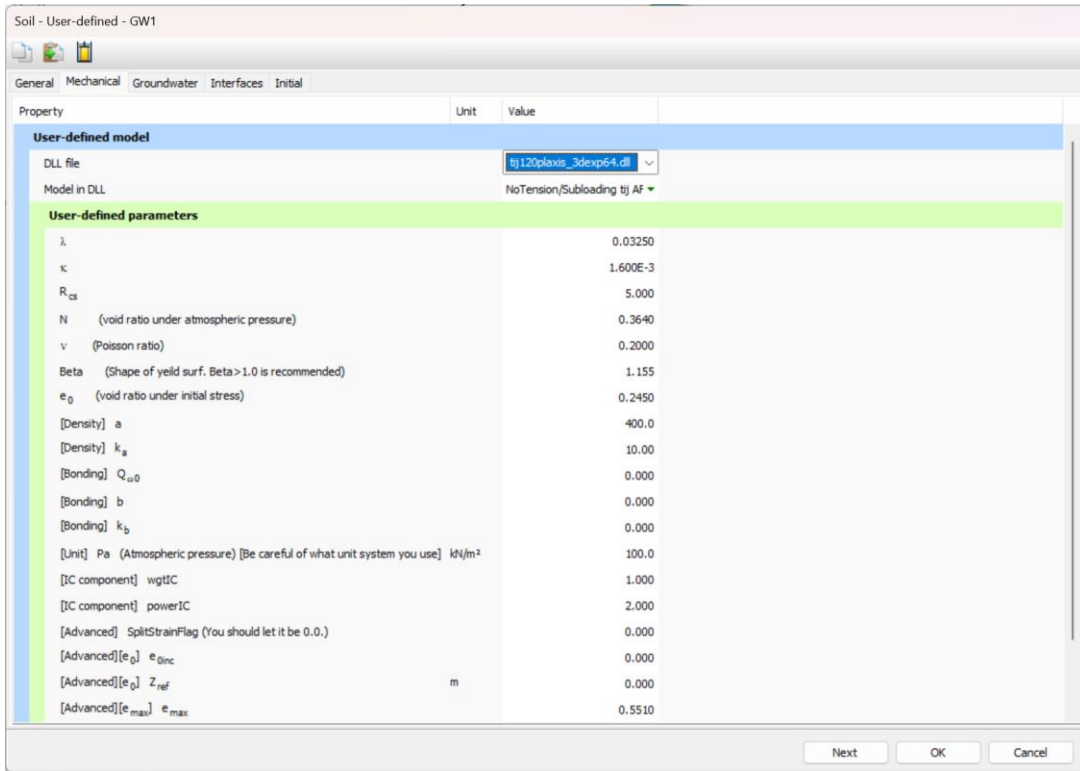


Figure 5-1 PLAXIS 3D parameter input for user-defined Subloading *tij*.dll.

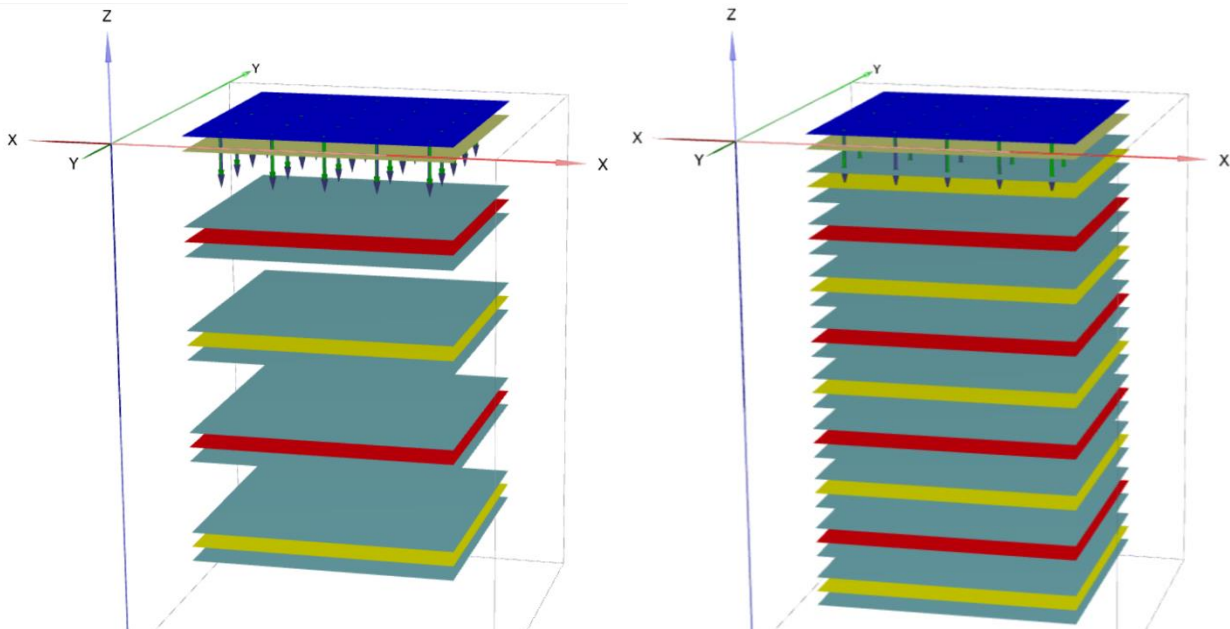


Figure 5-2 Alternating pattern geotextile layers (red-yellow) and plate (dark blue) with interfaces (turquoise):
Left - TF-10, Right - TF-7.

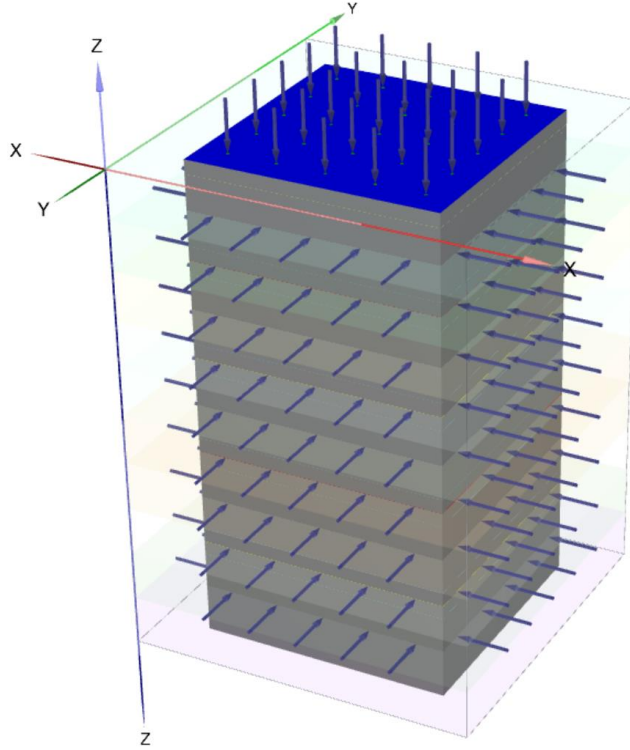


Figure 5-3 Soil after the removal of the volumes with unsaturated confining loads.

5.2 PLAXIS 3D Model Overview

The model was configured, and simulations were conducted in SI units with length in meters and force in kN. The unit weight of water was taken as 10.00 kN/m³. 10-noded elements were utilized during modeling. Mesh generation was conducted procedurally by PLAXIS 3D. The “medium” element distribution option with local refinements and coarsening was employed (Figure 5-4). The “Refine mesh” option was used to decrease the coarseness of all the interfaces in the model (command employed once). Similarly, the “Coarsen mesh” option was used to increase the coarseness of the volumes to their maximum coarseness.

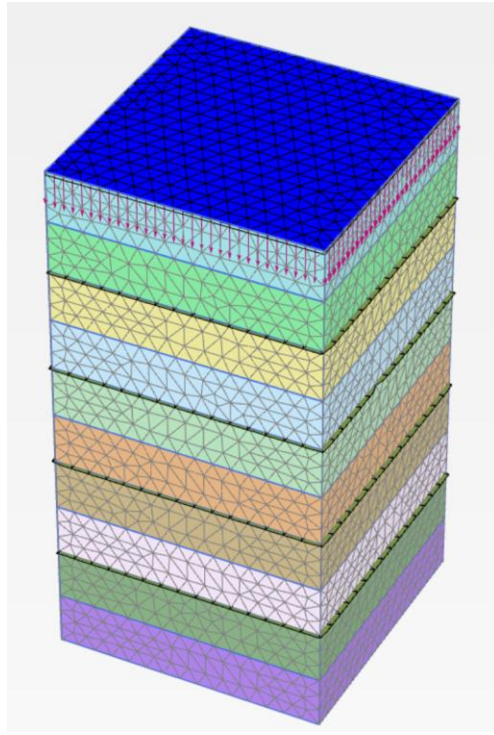


Figure 5-4 PLAXIS generated mesh using the "medium" element distribution.

The 17 load stages (including an “Initial Stage”) were used during simulation. Prescribed area displacements were applied to the top plate to model the loading. The prescribed displacements were taken from the TF-7 and TF-10 test data. The simulation solved for the resulting force. The bottom of the pier was designated as fixed with the sides and top designated as free in order to indicate to PLAXIS that the resulting force should be calculated.

Multiple user-defined model .dlls were available to perform the simulations, including an implicit formulation and explicit formulation. This study utilized three .dll files during simulation. Ultimately, the most recent explicit formulation .dll and PLAXIS’s “Paradiso” direct solver were utilized to perform the simulation. The remaining numerical control parameters are shown in Figure 5-5. One note is that the parameters shown in Figure 5-5 were generally utilized for the first 13 stages but do not necessarily represent stages 14 through 16. To combat numerical issues that appeared at later stages; the tolerated error was decreased to 0.01, the max number of iterations was increased to 250, the desired minimum number of iterations was set to 25, and the desired maximum number of iterations was set to 250. Additionally, the “Reset displacements to zero” and “Reset small strain” options were used only during the volume removal stage (stage 1).

Name	Value
General	
ID	Phase_1
Start from phase	Initial phase
Calculation type	<input checked="" type="checkbox"/> Plastic
Loading type	<input type="checkbox"/> Staged construction
ΣM_{stage}	1.000
ΣM_{weight}	1.000
Pore pressure calculation type	<input checked="" type="checkbox"/> Phreatic
Time interval	0.000 day
First step	1
Last step	100
Special option	0
Deformation control parameters	
Ignore undr. behaviour (A,B)	<input type="checkbox"/>
Reset displacements to zero	<input checked="" type="checkbox"/>
Reset small strain	<input checked="" type="checkbox"/>
Reset state variables	<input type="checkbox"/>
Reset time	<input type="checkbox"/>
Updated mesh	<input type="checkbox"/>
Ignore suction	<input checked="" type="checkbox"/>
Cavitation cut-off	<input type="checkbox"/>
Cavitation stress	100.0 kN/m ²
Numerical control parameters	
Solver type	Pardiso (multicore direct)
Max cores to use	256
Max number of steps stored	1
Use compression for result files	<input type="checkbox"/>
Use default iter parameters	<input type="checkbox"/>
Max steps	1000
Tolerated error	0.5000
Max unloading steps	5
Max load fraction per step	0.01000
Over-relaxation factor	1.200
Max number of iterations	60
Desired min number of iterations	6
Desired max number of iterations	15
Arc-length control type	Auto
Use subspace accelerator	<input type="checkbox"/>
Subspace size	3
Use line search	<input checked="" type="checkbox"/>
Use gradual error reduction	<input type="checkbox"/>

Figure 5-5 PLAXIS individual stage control parameters.

5.3 Model Runs

In general, the simulations terminated at smaller deflections/lower loads than the failure points recorded during testing. Simulation of the piers typically terminated at stage 15 with various ill-defined numerical issues arising. Typically, the numerical issues were either a cascading error development, a slow convergence error, or a complete/partial unloading error. The cause of the numerical was investigated with modification of the staging parameters, verification of the model parameters, and redrawing geometry. No universal solutions were discovered, with the hypothesis that reexamination of the optimization process/model parameter generation is necessary.

Several rounds of simulations were conducted using different .dlls provided by Dr. Teruo Nakai and tij地盤解析研究会. The initial analysis was performed using a .dll from 2018. This formulation did not incorporate the e_{max} and $h^{p(soft)}$ parameters. The simulation was then repeated using a 2019 version that incorporated the e_{max} and $h^{p(soft)}$ parameters. Finally, a .dll from 2023 that integrated a different explicit solution scheme was utilized to perform the simulation. Each formulation produced slightly different results (Figure 5-6). Ultimately, the most recent .dll (2023) was selected to perform the final simulations.

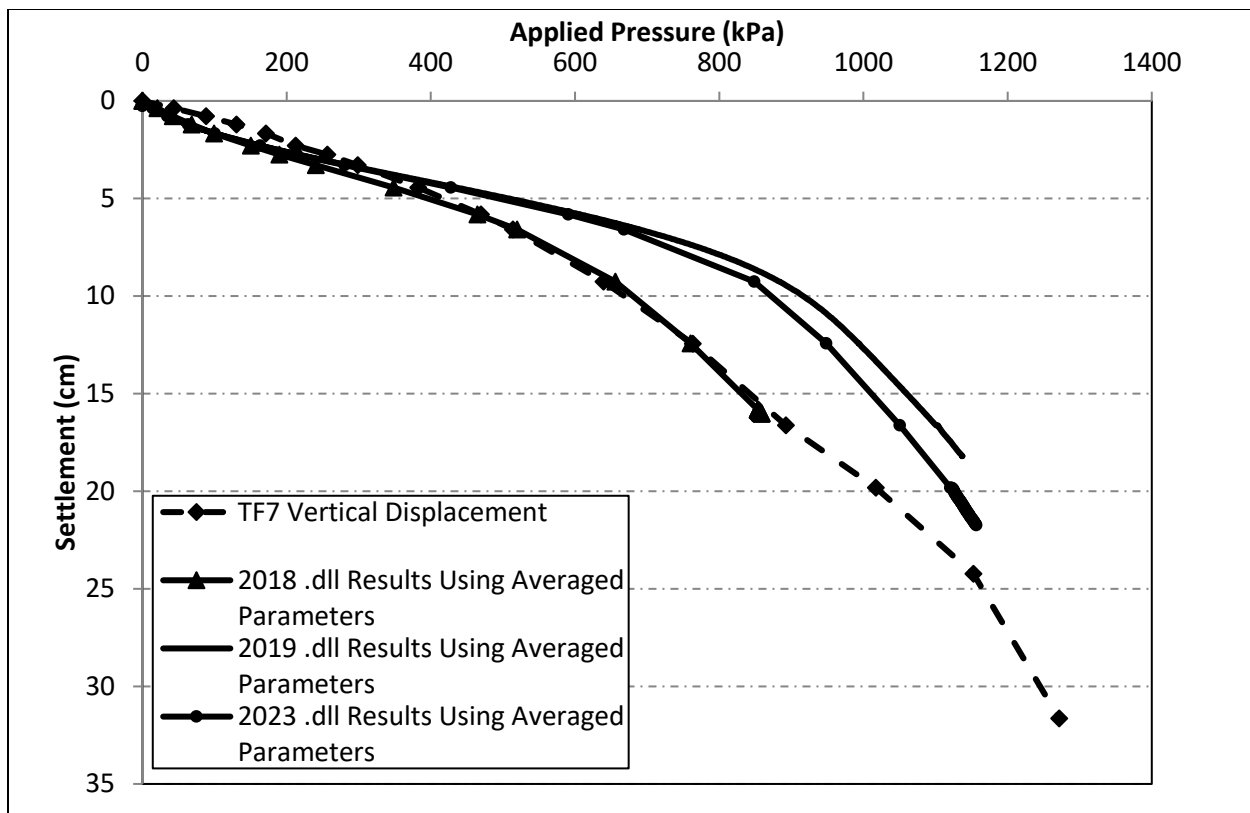


Figure 5-6 Comparison of different user-defined model .dlls using the same Subloading t_{ij} parameters.

During the course of the initial simulation, it became clear that the CD triaxial optimized parameters were failing to fully account for the geotextile-soil behavior. In general, the optimized parameters tended to produce behavior stiff of test results. The cause of this failure to capture behavior using the optimized parameters is not fully known but is theorized to be the result of a confluence of factors including possible overfitting during optimization, triaxial testing performed at a different relative compaction, or an error in assumed values for other model components. To investigate the effect of the model parameters, the simulation was performed again using the same general configuration except utilizing a set of Subloading t_{ij} parameters that were generated by Dr. Phillip S.K. Ooi during the summer of 2022. These “Dr. Ooi” parameters produced GRS pier model behavior that was softer than the test results. The results of simulation of TF-7 using this study’s optimized parameters and Dr. Ooi’s parameters are shown in Figure 5-7 (2018 .dll).

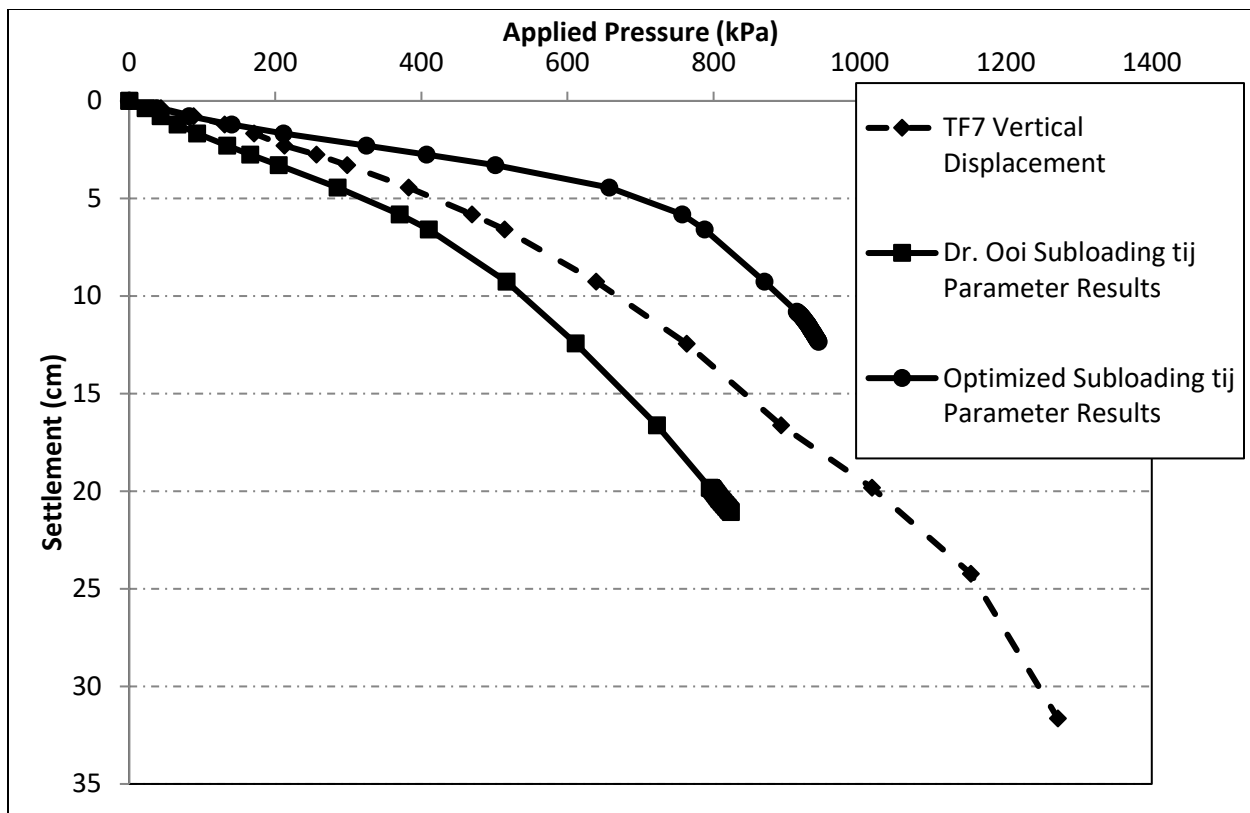


Figure 5-7 TF7 model simulation results using different Subloading t_{ij} parameters compared to test data.

The results implied that the Subloading t_{ij} parameters that would best model the test results lay somewhere between the optimized parameters and Dr. Ooi's parameters. As the test results appear to bisect the two simulation results, an approximate average of the two sets of Subloading t_{ij} parameters was attempted first. Table 5-1 lists both Dr. Ooi's parameters and the "averaged" parameters.

Table 5-1 Dr. Ooi's Parameters and the Averaged set of parameters

Parameter	Dr. Ooi's Value	Averaged Values
λ	0.04	0.0325
κ	0.0016	0.0016
R_{cs}	5	5
N	0.373	0.364
β	1.2	1.155
a	800	400
k_a	20	10
v	0.2	0.2
e_{max}	0.551	0.551

The Averaged parameters generated the results shown in Figure 5-8 (2018 .dll). The results shown in Figure 5-8 seem to show very good agreement between simulation and test results.

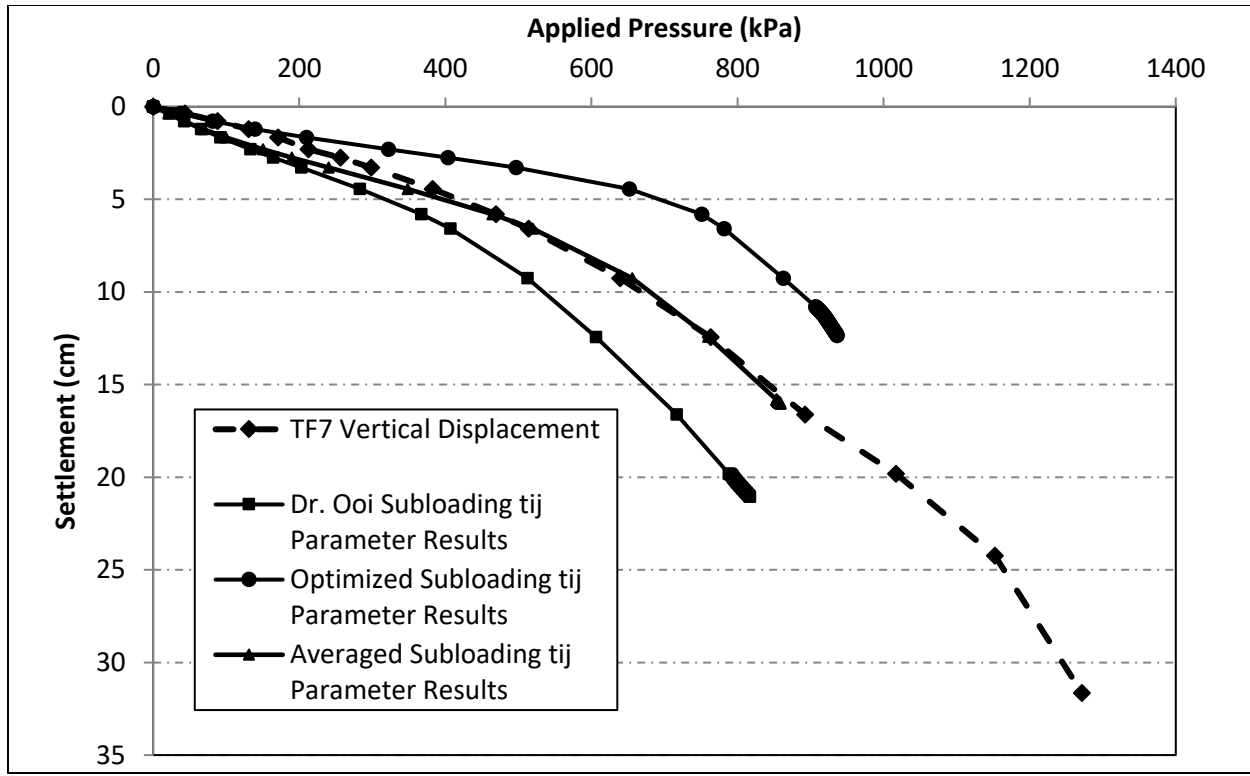


Figure 5-8 Comparison of the various Subloading t_{ij} parameter sets to testing data for TF-7.

To ensure the Averaged parameters (hereafter, “parameters”) are not a numerical abnormality and still produce sensible results, they were additionally utilized to model the triaxial and the isotropic consolidation testing data. The results shown in Figure 5-9, Figure 5-10, and Figure 5-11 were produced using the “Subloadingtij_a.exe” program employed during optimization (Section 4.1.3). The resulting R^2 and R values are 0.83466 and 0.90701. The results indicate that the parameters produced results that correlate fairly well with the test results. A visual inspection indicates that the parameter results do not match the triaxial testing data as well as the optimized results (Section 4.1.4). This is additionally indicated when comparing the overall parameter fit statistics (Table 5-2) with the optimized fit statistics (Table 4-4).

Table 5-2 Descriptive statistics for Averaged parameter modeled results.

Metric	R^2	R	CoV	RSS	C_v	RSS/CoV
$q (\sigma_3 = 5 \text{ psi})$	0.39707	0.63013	6.81273	3133.04	0.11656	459.880
$q (\sigma_3 = 10 \text{ psi})$	0.87845	0.93726	29.6866	8279.56	0.13006	278.899
$q (\sigma_3 = 30 \text{ psi})$	0.96252	0.98108	767.852	18056.6	0.27587	23.5158
$\varepsilon_v (\sigma_3 = 5 \text{ psi})$	0.83538	0.91399	8.87E-06	0.00079	-0.69013	89.3183
$\varepsilon_v (\sigma_3 = 10 \text{ psi})$	0.78685	0.88705	1.72E-04	178.899	2.93460	1.04E+06
$\varepsilon_v (\sigma_3 = 30 \text{ psi})$	0.92917	0.96394	2.57E-05	0.03539	0.41076	1376.06
e	0.98594	0.99294	1.19E-05	0.10605	0.01055	8889.70
Average	0.83466	0.90701				
Average (w/o q [$\sigma_3 = 5 \text{ psi}$])	0.89717	0.94656				

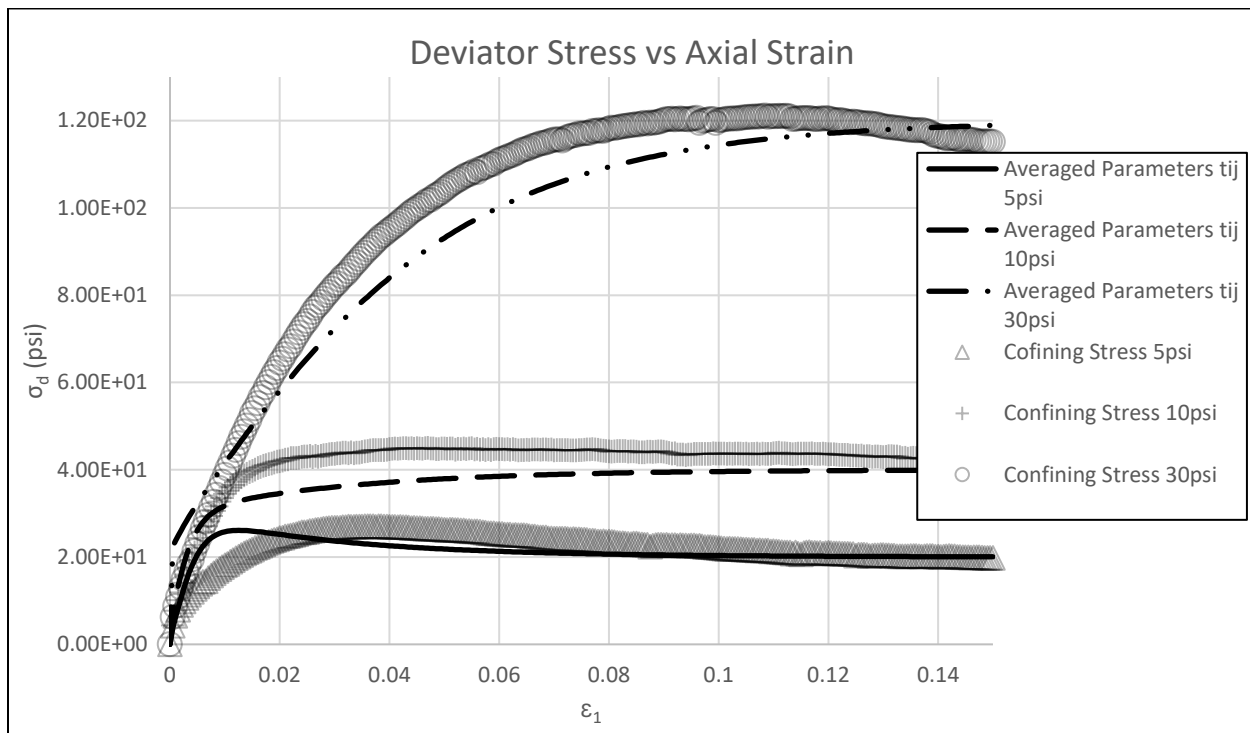


Figure 5-9 Stress-strain curve for triaxial tests from CD testing vs Averaged parameter model simulation.

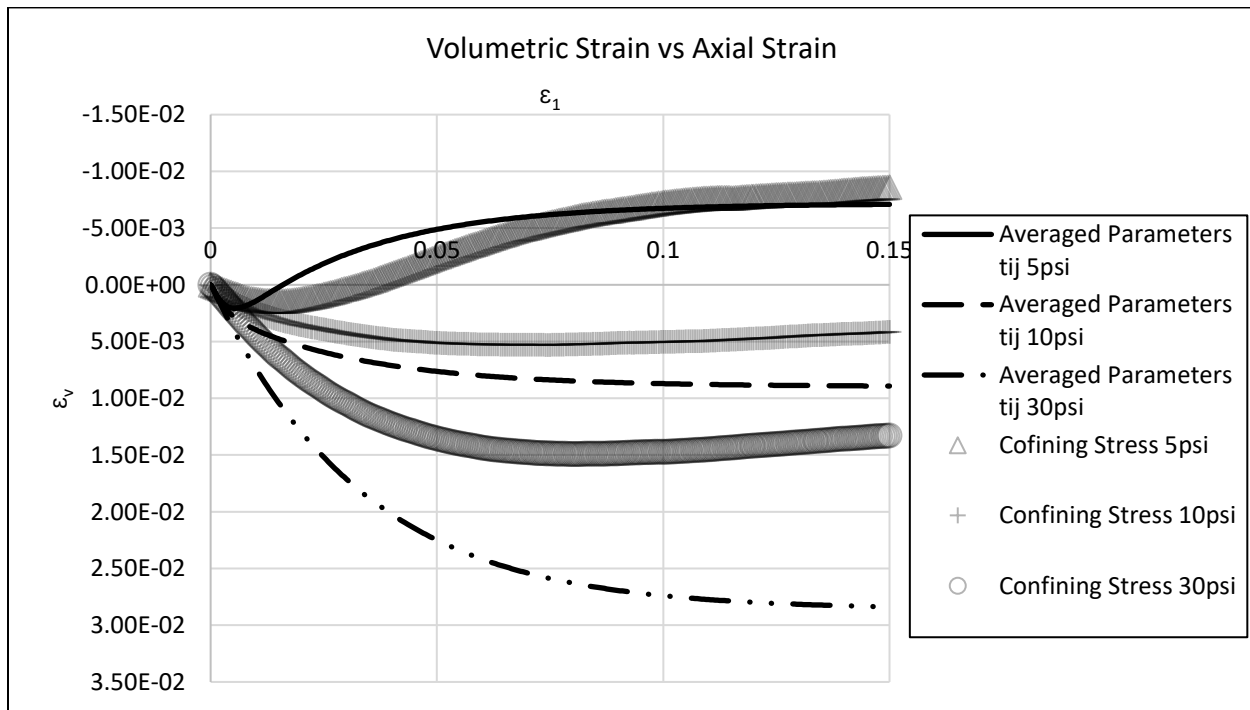


Figure 5-10 Triaxial volume change curves from CD testing vs Averaged parameter model simulation.

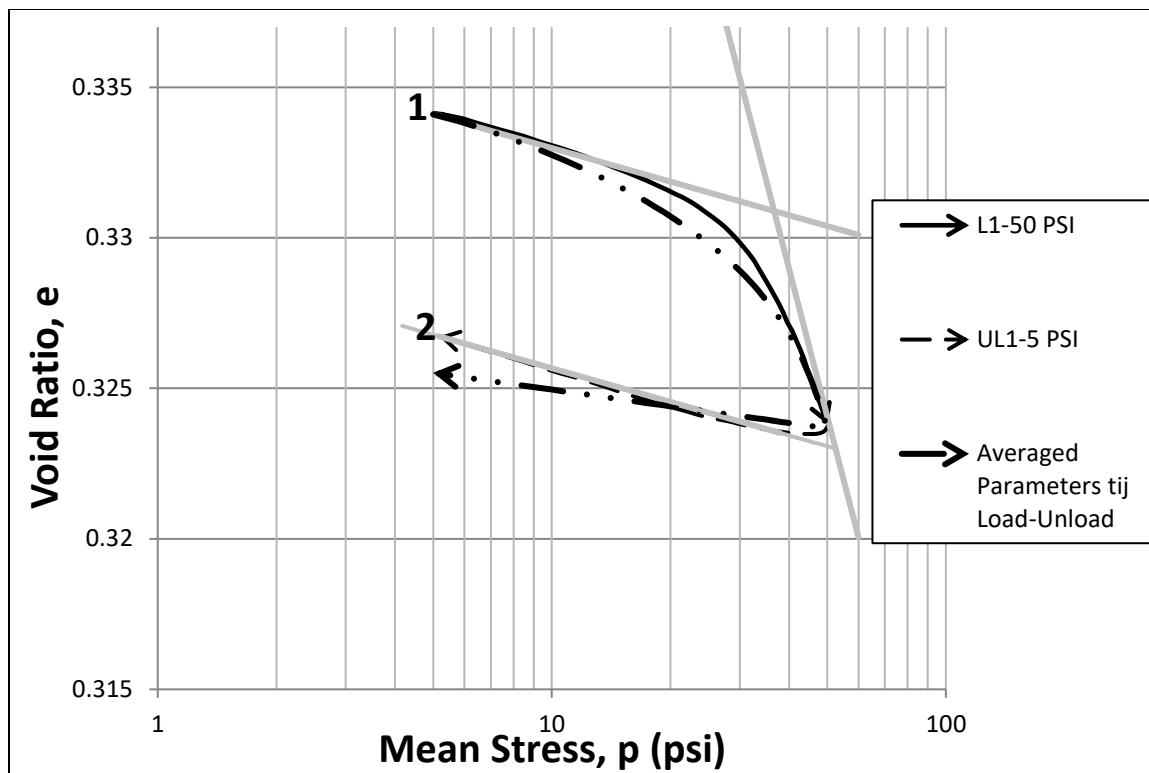


Figure 5-11 e - log p curve from IC testing vs Average parameter model simulation.

The parameter results overall describe softer material behavior when compared with the optimization results. This is consistent with PLAXIS results which indicated that the optimized results yielded stiffer behavior of the GRS pier. The parameter results did produce R^2 and R values closer to 1 (although only marginally so). The behavior that is perhaps most starkly different is the isotropic consolidation results. The parameter results match the isotropic consolidation results significantly better than the optimized results with nearly all fit statistics indicating a better fit. Based on the triaxial behavior, the isotropic consolidation behavior, and the results of the PLAXIS modeling, the parameters (Averaged) were utilized to produce the results shown in Chapter 6.

A mesh size sensitivity analysis was conducted to establish that the “medium” element distribution option produced sufficient model accuracy. Figure 5-12 Sensitivity analysis of mesh density selection in PLAXISFigure 5-12 shows PLAXIS results using the “medium”, “fine”, “coarse”, and “very coarse” element distributions. Decreasing mesh size significantly impacts simulation time with the fine element distribution requiring approximately 5 times the compute time of the very coarse. As compute times can become prohibitively long for very dense mesh, the selection of the “transition” or “threshold” mesh where further mesh refinement produced marginal gains in accuracy was the objection of the sensitivity analysis. The results indicate that the medium element distribution appears to be the “threshold” mesh size. This is reinforced by the descriptive statistics in Table 5-3. A piecewise comparison of the PLAXIS options indicates that the transition from a medium to fine mesh produces an order of magnitude less accuracy gain when compared with the transitions from very coarse to coarse and from coarse to medium. This change in the magnitude of accuracy gain is shown in the RSS, CoV, and RSS/CoV values and is indicative of the desired threshold.

Table 5-3 Descriptive statistics for mesh density sensitivity analysis.

Statistic	Very Coarse to Coarse	Coarse to Medium	Medium to Fine
RSS/CoV	1.46E-03	1.28E-03	3.73E-04
RSS	296.229	239.907	67.176
CoV	4.31E-01	3.07E-01	2.51E-02

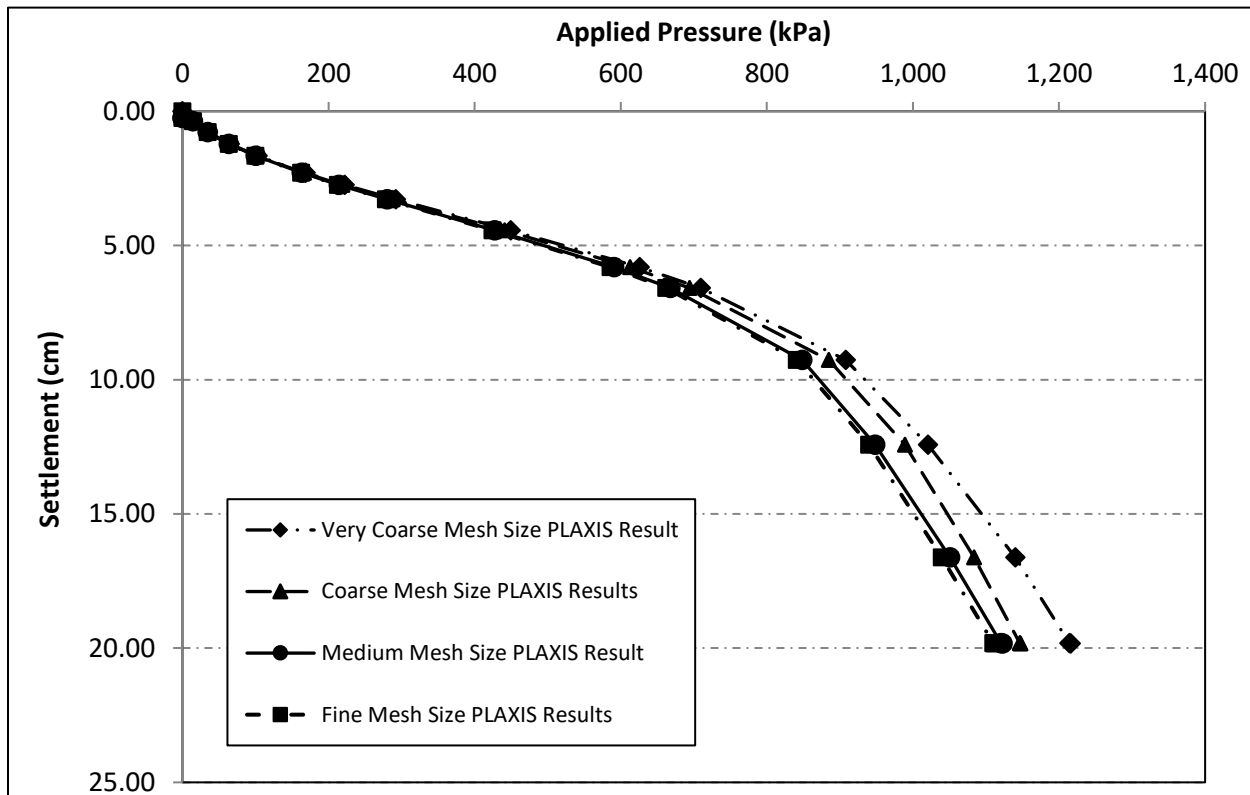


Figure 5-12 Sensitivity analysis of mesh density selection in PLAXIS

Simulation of two faced GRS piers (TF-6 and TF-9) was attempted using the same methodology discussed here. Numerical issues arose during simulation. Several different approaches were employed to calculate interface parameters with variation attempts falling in the range of typical values. Several different PLAXIS error codes were produced during simulation without obvious cause or pattern. The scope of this study did not allow for a sufficiently in-depth investigation to determine the underlying cause of the numerical difficulties. Discussion of recommendations and future work is included in Section 7.

6. Results

6.1 Stress Development

Three vertical cross-sections through the centerline of the GRS piers were utilized to visualize the final stress results: a 45° diagonal cross-section, an XZ cross-section, and a YZ cross-section. The effect of the geotextile reinforcement can be clearly seen in the stress development shown in Figure 6-1 through Figure 6-10. Shear stress development in the backfill is dissipated and transferred to the reinforcement. Figure 6-5 and Figure 6-10 show the spreading tendency that develops in the pier. The plots of σ_{yz} and σ_{zx} (shear stresses that are parallel to XZ and YZ cross-sections are projected onto each cross-section respectively) show the shear stress development adjacent to the reinforcement layers. When shear stress is transferred to the reinforcement layers, a confining stress is generated. This confining stress can be seen in the σ_{xx} and σ_{yy} plots. The normal stress gradient in the geotextile reinforcement further supports the existence of a confining stress provided by the reinforcement.

Shear stress development and the corresponding shear stresses are shown in Figure 6-2Figure 6-3Figure 6-7Figure 6-8, and Figure 6-4 and Figure 6-9, respectively. The deviatoric strains reflect a total deviator strain and thus reflect a combination of stress development. The deviator strains are indicative of the stress dissipation provided by the reinforcement. Deviator strains develop in the backfill between reinforcement and are resisted by the geotextile layers. Of particular interest is the development of an approximately semicircular region of deviator strain near the edges of the pier whose loci are located roughly halfway between reinforcement layers. Examination of TF-7's stage-by-stage deviator strain development indicates that these loci move closer to the center of the pier with each successive load increase. This corresponds with an increase in deviatoric strain in the center of the pier as well as a concentration of strain, inducing a more pronounced gradient both vertically and to a lesser degree horizontally. This effect is likely the precursor to the development of the shear band that was observed during testing.

Another interesting feature of stress development is the localization of "stress bulbs" approximately underneath the edges of the footing. The development of localized increased shear stress can be seen in both TF-7 and TF-10 but is more immediately obvious in TF-7. The localized shear stress is accompanied by a reversal (or approximate reversal) of sign across the reinforcement layers. Division of the GRS piers based on function during loading can thus be visualized based on the location of the stress bulbs. During loading, a central "bearing column" that bears the majority of the induced vertical stress appears to develop. A transition "shearing zone" appears to bound the bearing column. The shearing zone's location and extent seem to be controlled by the extent of the footing and the reinforcement spacing. The shearing zones appear to be large when reinforcement spacing is larger. This can be seen with relative clarity in Figure 6-5 and Figure 6-10. An exterior "confining shell" is generated by the reinforcement. This shell has low shear stress but also low horizontal stress. The spalling observed in TF-10 during testing was likely this "confining shell" without whom, progressive shear failure of the backfill between reinforcement layers occurs.

As indicated during load testing (Nicks et al., 2013), no clear shear plane can be seen to develop during simulation of TF-10. Instead, fairly random highly localized increased stress (indicative of a failure of the soil fabric) can be seen to develop as shown in Figure 6-6, Figure 6-7, and Figure 6-8.

Although full pier failure was not observed during simulation (not all load steps were successfully calculated), this behavior is consistent with a cascade failure of the soil fabric as was observed during load testing. Similarly, TF-7 emergent behavior appears consistent with observed failure during loading testing. The initial development of a shear plane can be seen in the shear stress development at the top and bottom of the pier (as shown in Figure 6-1, Figure 6-2, and Figure 6-3). Although final failure was not successfully simulated, the propagation of the top and bottom shear stress development towards each other as successive reinforcement occurs would result in an observable shear plane failure. The development of a well-defined shear plane is consistent with the behavior observed during load tests (Nicks et al., 2013).

A final observation is that the magnitude of stress development is significantly higher in TF-7 when compared to TF-10. The magnitude of stress in TF-7's backfill is approximately twice that of TF-10. However, the magnitude of forces in the geotextile reinforcement are approximately equivalent. The development of significantly higher stresses in TF-7 can thus occur due to the reinforcing and confining effects provided by the geotextile. This can be interpreted as a shift to the right in shear-normal stress space. An increase in the major principal stress occurs but is precipitated by a corresponding increase in the minor principal stress (such as that provided by the reinforcement), increasing shear stress without reaching the yield state.

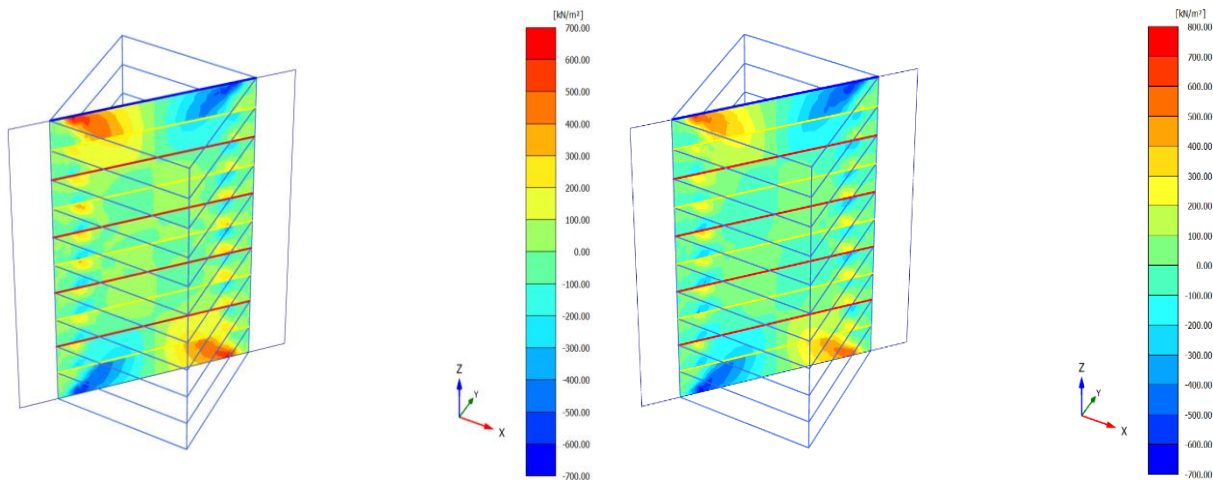


Figure 6-1 TF-7 45° diagonal cross-section shear stress distribution: σ_{yz} (kPa) – Left, σ_{zx} (kPa) - Right.

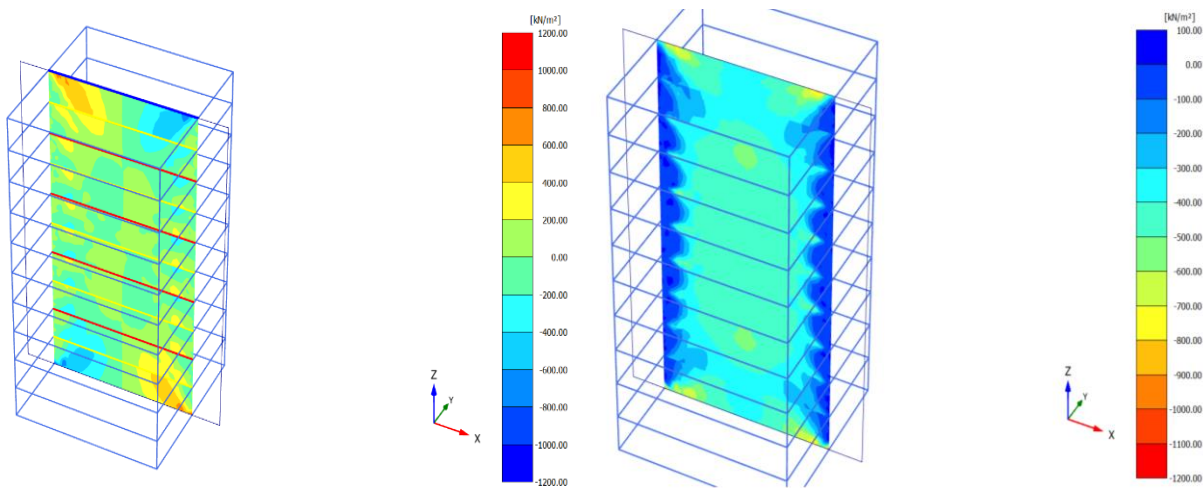


Figure 6-2 TF-7 YZ-plane cross-section stress distributions: σ_{xz} (kPa) – Left, σ_{xx} (kPa) - Right.

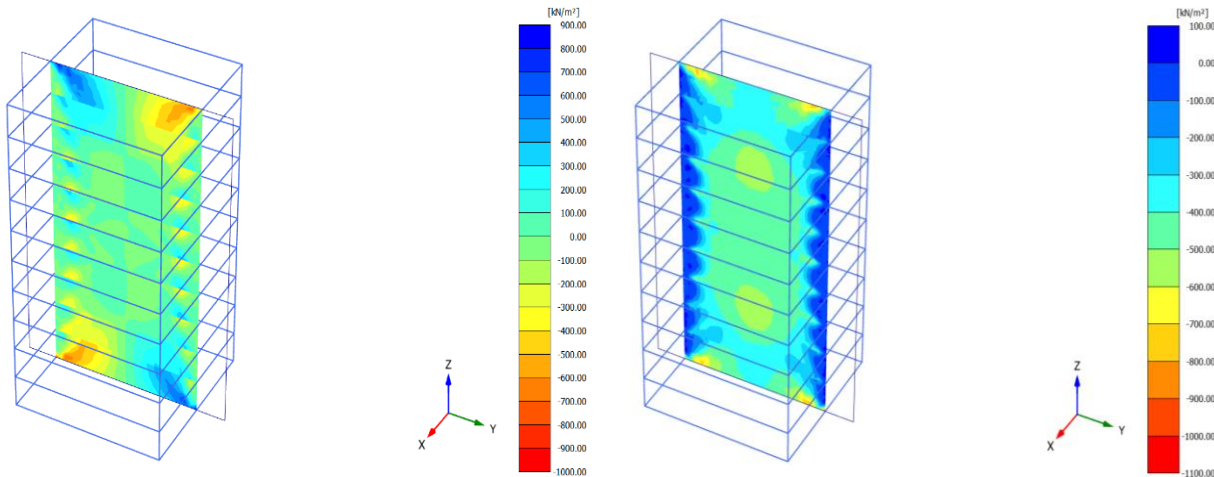


Figure 6-3 TF-7 XZ-plane cross-section stress distributions: σ_{yz} (kPa) – Left, σ_{yy} (kPa) - Right.

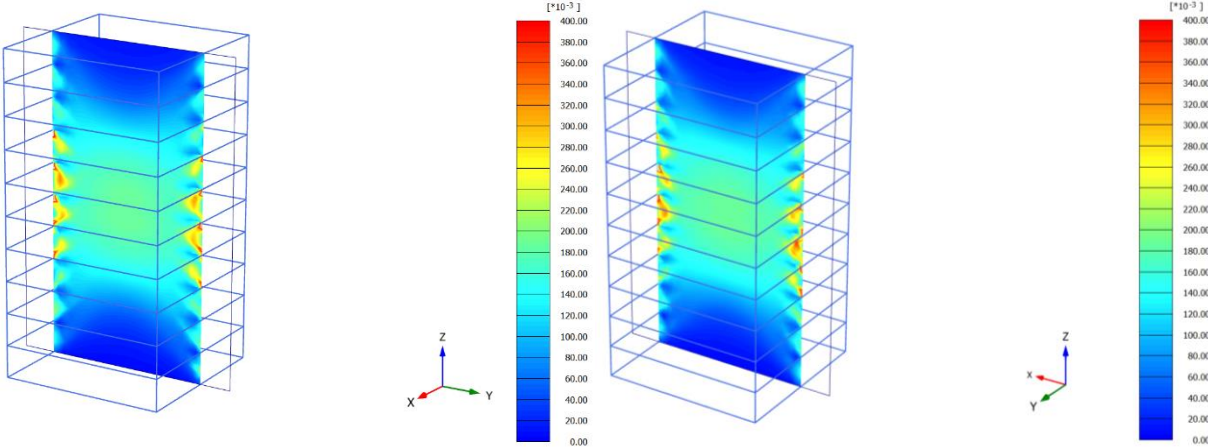


Figure 6-4 Deviatoric strain γ_s distributions: Left - YZ cross-section, Right - XZ cross-section.

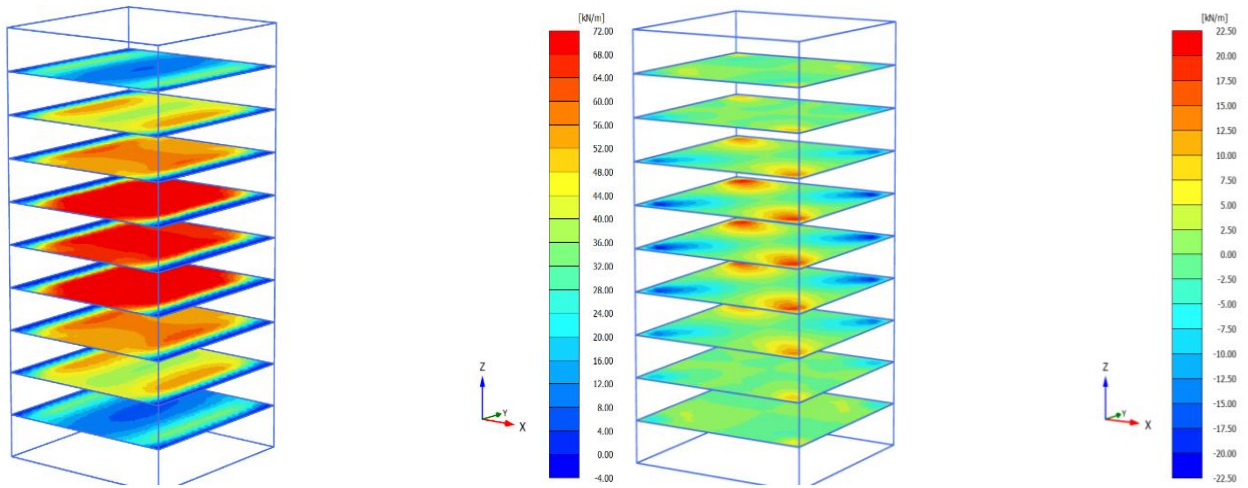


Figure 6-5 TF-7 geotextile force distributions: N_1 (in-plane force, kN/m) – Left, Q_{12} (in-plane shear, kN/m) - Right

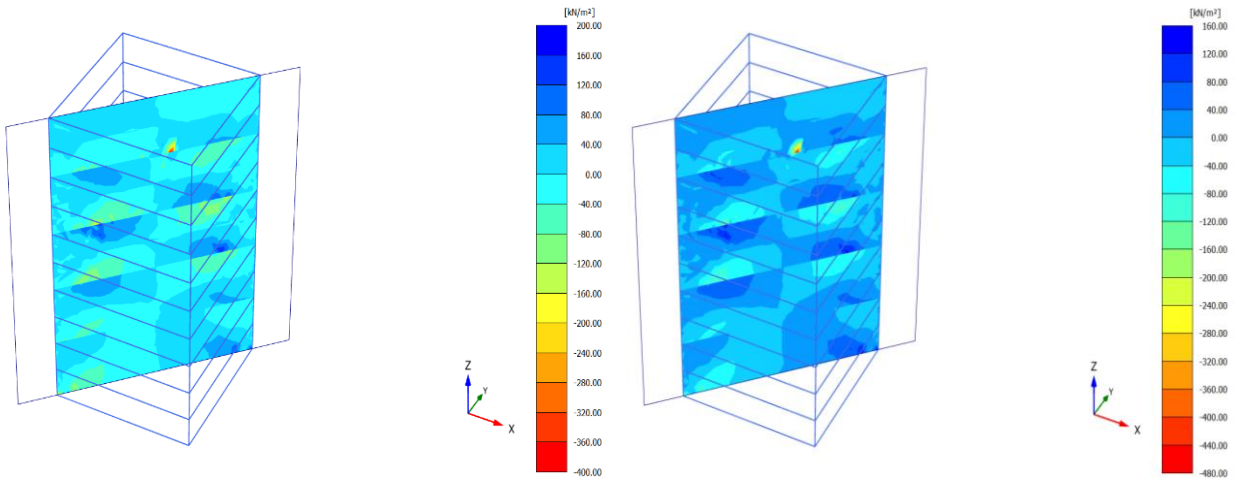


Figure 6-6 TF-10 45° diagonal cross-section shear stress distribution: σ_{yz} (kPa) – Left, σ_{zx} (kPa) - Right.

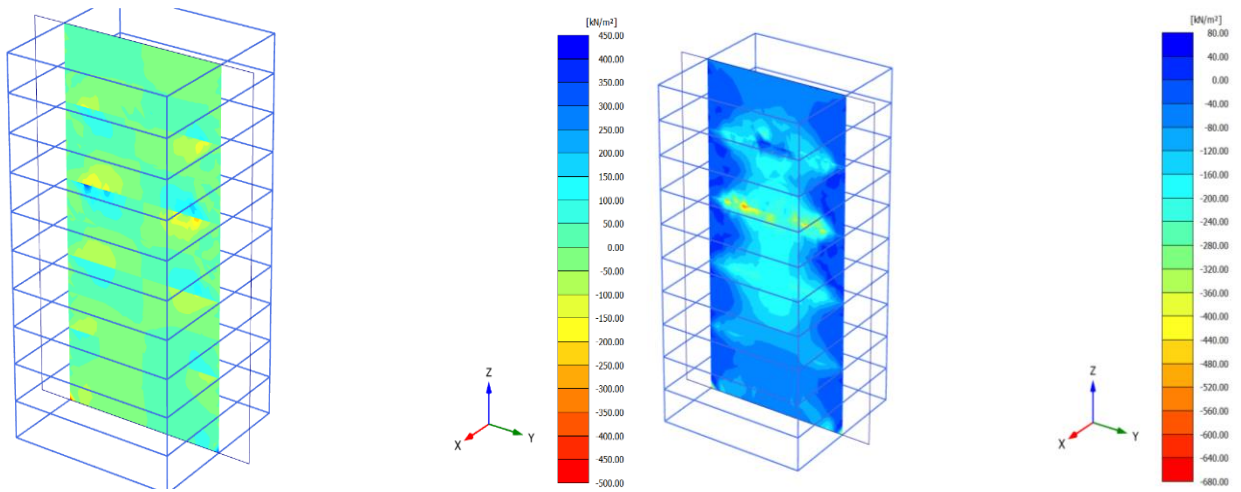


Figure 6-7 TF-10 XZ-plane cross-section stress distributions: σ_{yz} (kPa) – Left, σ_{yy} (kPa) - Right.

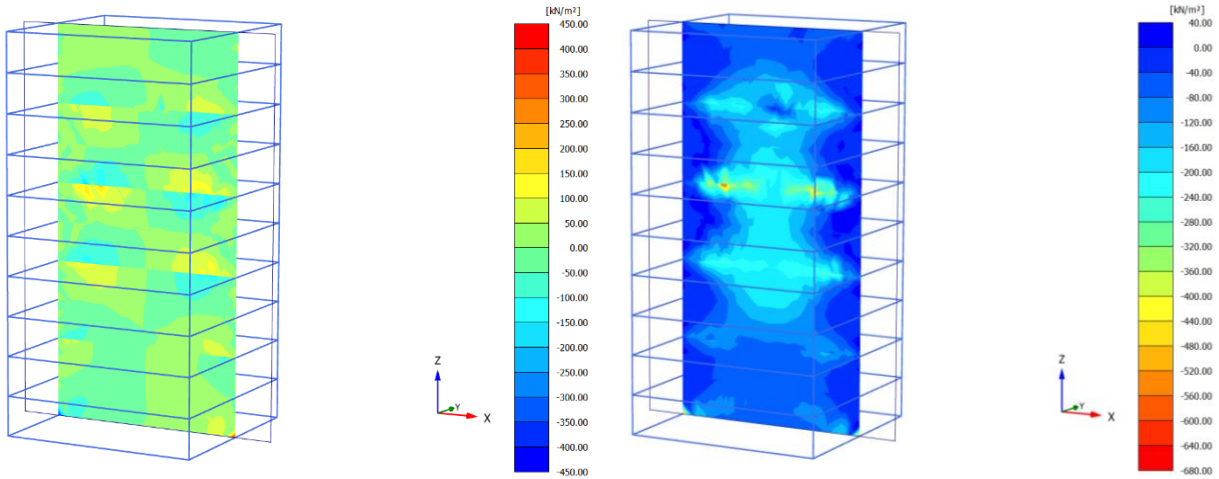


Figure 6-8 TF-10 YZ-plane cross-section stress distributions: σ_{zx} (kPa) – Left, σ_{xx} (kPa) - Right.

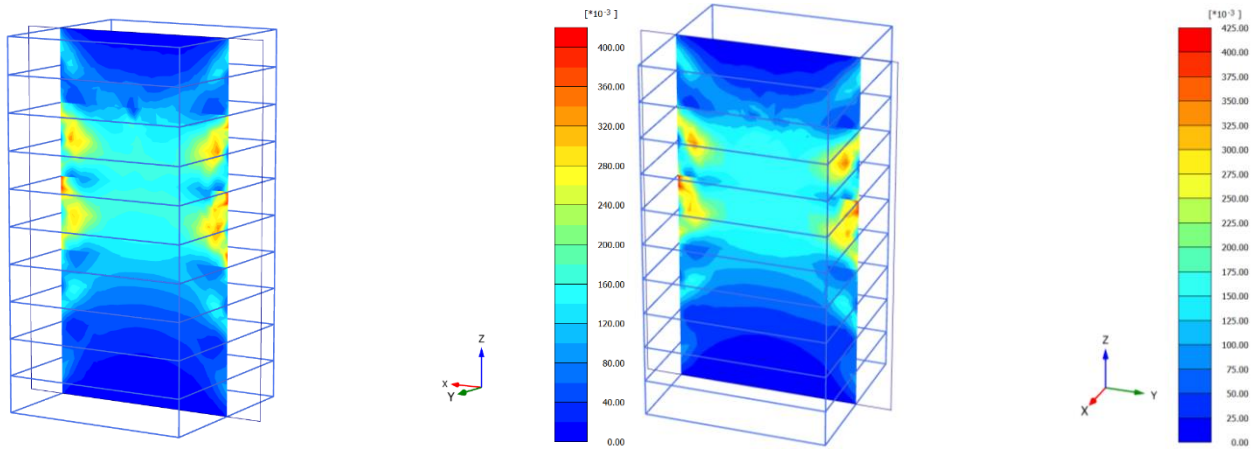


Figure 6-9 Deviatoric strain γ_s distributions: Left - XZ cross-section, Right - YZ cross-section

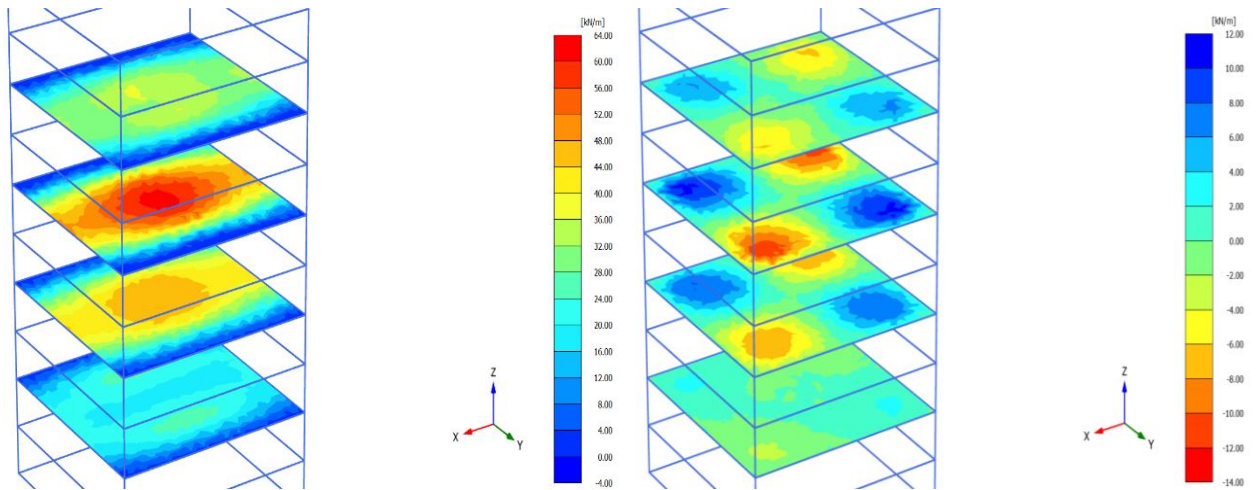


Figure 6-10 TF-10 geotextile force distributions: N_2 (in-plane force, kN/m) – Left, Q_{12} (in-plane shear; kN/m) - Right

6.2 Vertical Displacement

PLAXIS-generated vertical displacements for TF-7 and TF-10 are shown in Figure 6-11 and Figure 6-12. In general, the vertical displacements from testing appear to be bounded by the PLAXIS model. Simulation of TF-7 generates behavior stiffer than test data. This contrasts with PLAXIS results for TF-10, which generated behavior that was softer than test data. Descriptive statistics are included in the following table:

Table 6-1 Descriptive statistics for PLAXIS TF-7 and TF-10 model vertical displacements.

GRS Pier	R²	R	CoV	RSS	C_v	RSS/CoV
<i>TF - 7</i>	0.96413	0.98190	150905	1.73E+05	0.883934	1.145405
<i>TF - 10</i>	0.99046	0.99522	16753	3.72E+04	0.720752	2.22
<i>Average</i>	0.97730	0.98856				

Visual inspection of the vertical displacement seems to further indicate that the TF-10 results approximate the test behavior better than the TF-7 results. This is further reinforced by the **R²**, **R**, **RSS**, and **C_v** values listed in Table 6-1.

An interesting feature and notable difference between the simulation results and the test data is the small strain behavior. The initial portion of the load-settlement curve (settlement <5 cm) shows that the PLAXIS model is failing to fully capture reinforcement mobilization. This can be seen most clearly in Figure 6-11, but also to a lesser degree in Figure 6-12. The opposite concavities of the test data and the simulation results in the first ~8 steps imply a difference in the strength mobilization mechanism. The downward concavity of the test data implies that the reinforcement is mobilized early with the shear resistance that the geotextile provides preventing early-stage plastic behavior. The opposite is implied by the upward concavity of the PLAXIS results. The premature termination of the simulations prior to pier failure, prevented the full mobilization of the reinforcement layers. Forces within the reinforcement were generally below the wide width tensile strength with strains that did not exceed 5%.

Gradual mobilization of the reinforcement of the geotextile precipitates a positive change in the composite stiffness of the GRS pier. This would also result in a different value for the peak or yield strength. The ratio of geotextile plastic strain relative to aggregate backfill plastic strain would be affected by the mobilization displacement of the geotextile. Early-stage plastic yielding of the aggregate backfill results in later-stage soil behavior that is better represented by fully softened material parameters as opposed to partially softened or hardening (dilative) parameters. The mobilization behavior of the geotextile is regulated by interface elements in PLAXIS. Thus, interface element parameters must be properly considered when modeling the soil-geosynthetic interaction that is so indicative of GRS structures.

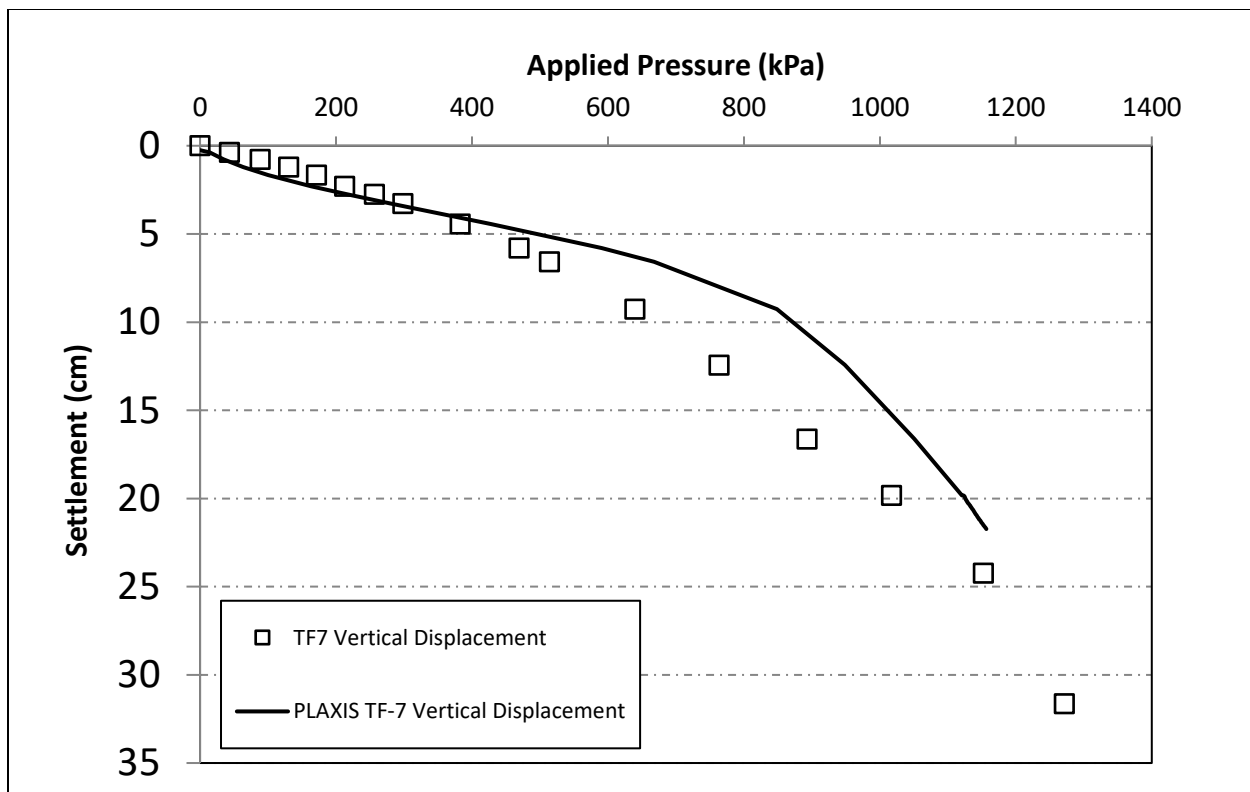


Figure 6-11 TF-7 vertical displacement at the center of the top of the pier.

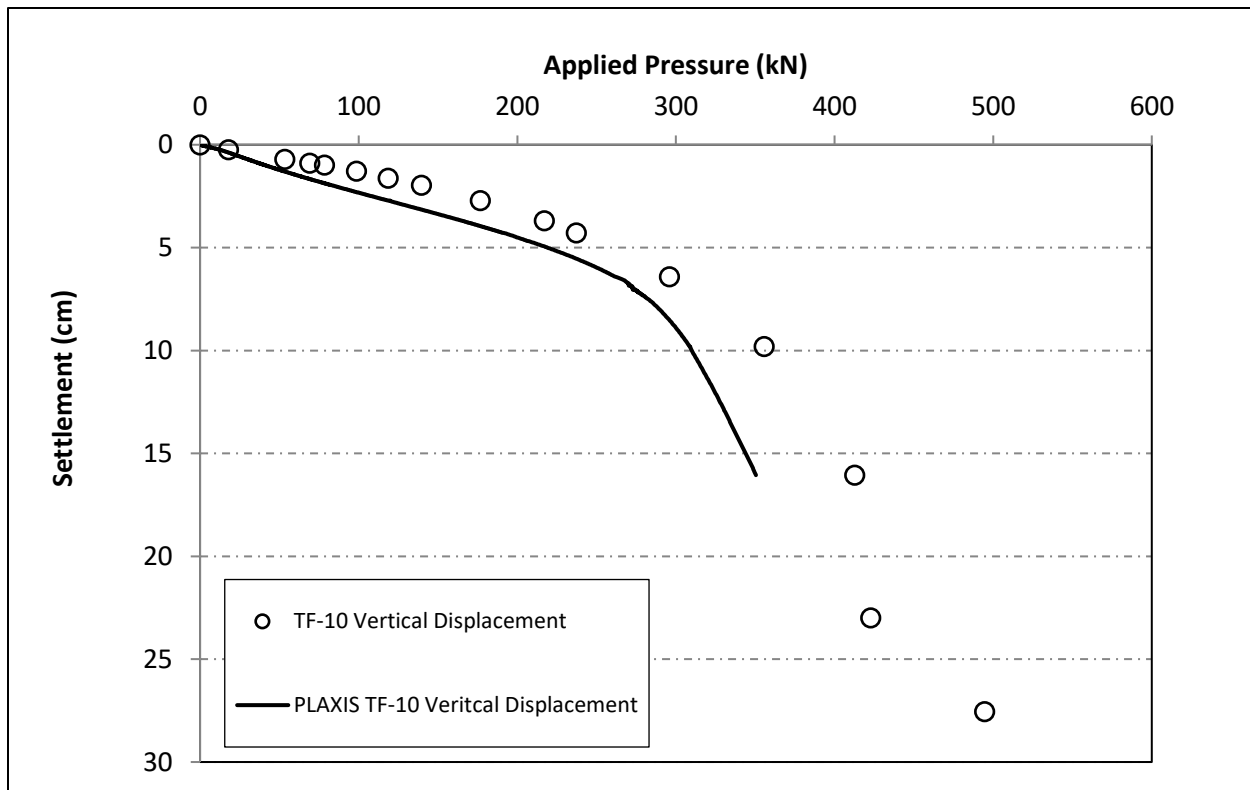


Figure 6-12 TF-10 vertical displacement at the center of the top of the pier.

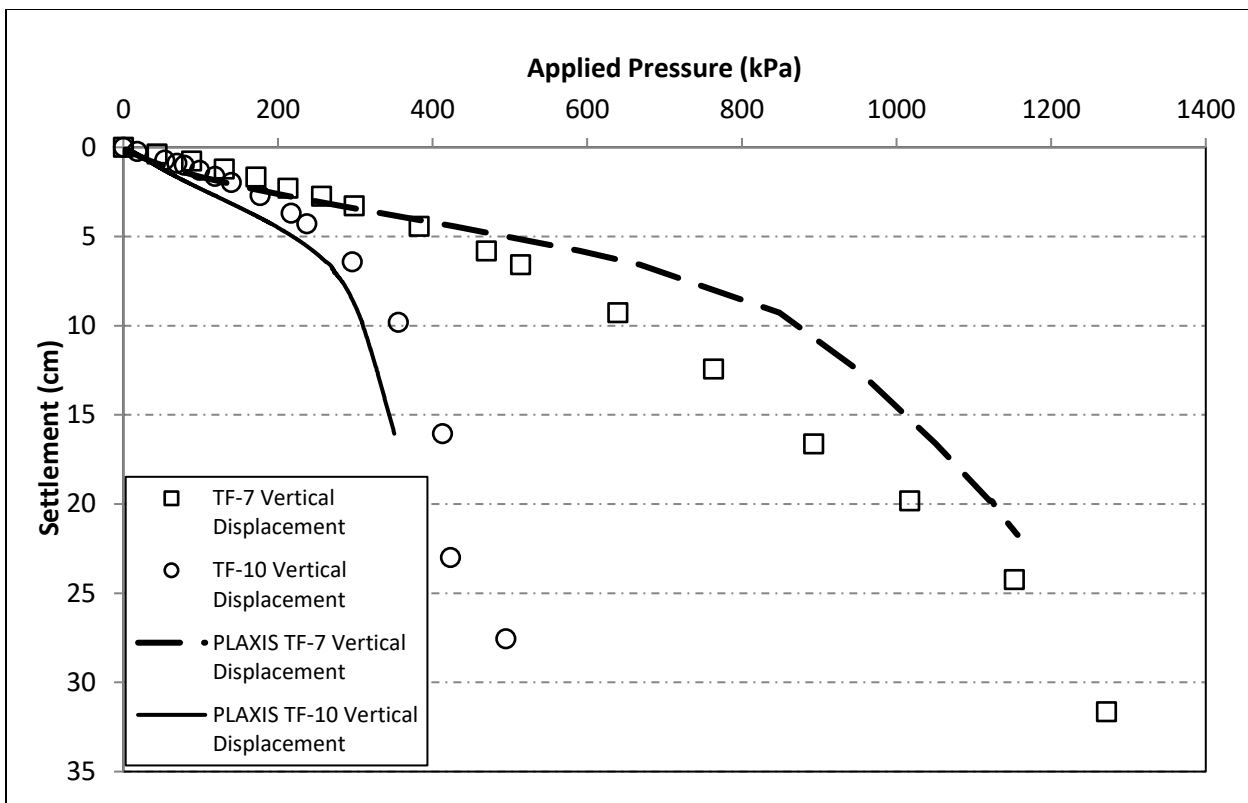


Figure 6-13 TF-7 and TF-10 vertical displacements vs PLAXIS models.

6.3 Horizontal Displacement

PLAXIS generated horizontal displacements along the height of the GRS piers vs. the horizontal displacement test data is shown in Figure 6-14 through Figure 6-19. The results are presented with corresponding load steps, i.e., “6.0 psi (measured)” is equivalent to the same load step/same vertical displacement as “2.06 psi (PLAXIS)” in Figure 6-14. The horizontal displacement results from simulation appear to approximate the typical shape of the displacement GRS pier fairly well. Small strain behavior presents the largest discrepancy between horizontally displaced shapes. The PLAXIS results present a largely consistent displaced shape with further displacement simply stretching or intensifying key features. The testing data presents a significantly less consistent displaced horizontal shape. This is especially true in the small strain range, with the general displaced shape changing with each load step.

The simulation results appear to most accurately model horizontal displacements for the center three LVDTs. This is further reinforced by the descriptive statistics listed in Table 6-2. R^2 and R values for the middle three LVDTs are consistently above 0.96, indicating a very good correlation. The PLAXIS results tended to underestimate horizontal deflection when compared to test data. Direct comparison of the horizontal displacements is difficult as simulation resulted in equivalent vertical displacement, not equivalent footing pressure. As such, delineation of whether displacements are underestimated due to lower footing loads or due to a failure to capture lateral earth behavior becomes difficult. For TF-7, there is a possible threshold load step where the underestimated lateral deflection transitions from being related to lower footing loads to being related to a failure to capture material behavior. It appears that somewhere around load step 6 or 7 is this threshold point. On the other hand, TF-10 does not appear to have this same

“threshold” point, and it is generally unclear whether the underestimation of lateral deflection is due to lower footing loads, a failure to fully capture material behavior, or some combination thereof.

The evolution of testing lateral displaced shape compared to the PLAXIS displaced shape implies that some additional variability in the GRS pier exists that is not being accounted for. Both TF-7 and TF-10 tended to produce larger relative displacement at the top of the pier during testing in the early loading stages. This evolves to a centrally bulging pier that is indicative of most of the GRS mini-pier testing conducted by the FHWA (Nicks et al., 2013). The PLAXIS results do not reflect this evolution. The elevation displaying the largest displacements at early stages also displayed the largest displacements at later stages. This discrepancy is likely due to the assumptions made about how consistent the aggregate backfill is, and the idealization of the reinforcement geotextile.

The ratio of the final vertical pressure and horizontal displacement generated by the simulation for TF-7 is approximately 100. This is compared to a ratio of approximately 20 to 50 for TF-10. This difference in magnitude implies that the generation of horizontal displacement is significantly less in TF-7 at similar vertical loads when compared with TF-10. Figure 6-20 shows this ratio as consistently larger in TF-7. Figure 6-20 shows that TF-10 produces vertical pressure vs horizontal displacement ratios that are well distributed, indicating that no single reinforcement layer bears a large majority of horizontal stress and shear development. This is not the case with TF-7. The final ratios for the central three measurement locations (LVDT-6, -7, and -8) are approximately $\frac{1}{4}$ of the top and bottom locations (LVDT-5 and -9). This indicates that the central reinforcement layers experience significantly higher horizontal stress. This observation is consistent with Figure 6-5 and Figure 6-10. The force heatmaps show that the largest in-plane forces develop in the central reinforcement layers in TF-7 while the largest reinforcement in-plane force in TF-10 develops in the layer with the largest vertical pressure to horizontal displacement ratio (LVDT-7).

Table 6-2 Descriptive statistics for PLAXIS TF-7 and TF-10 model horizontal displacements

GRS Pier	LVDT	R²	R	CoV	RSS	C_v	RSS/CoV
<i>TF-7</i>	LVDT-5	0.82315	0.90727	0.03226	1.07128	0.46696	0.03012
	LVDT-6	0.96760	0.98367	0.16221	0.12393	0.94334	1.30895
	LVDT-7	0.99814	0.99907	0.25675	0.06891	1.01614	3.72560
	LVDT-8	0.97294	0.98637	0.20394	0.50899	0.91003	0.40068
	LVDT-9	0.88770	0.94218	0.01984	0.05194	0.87294	0.38194
	Average	0.92991	0.96371				
<i>TF-10</i>	LVDT-5	0.95770	0.97862	0.03401	0.24216	0.81283	0.14042
	LVDT-6	0.99688	0.99844	0.22427	0.16460	1.20408	1.36249
	LVDT-7	0.98822	0.99409	0.07222	0.45290	0.80124	0.15946
	LVDT-8	0.96603	0.98287	0.05071	0.25672	0.88264	0.19753
	LVDT-9	0.82058	0.90586	0.01558	0.17306	0.76801	0.09001
	Average	0.94588	0.97198				

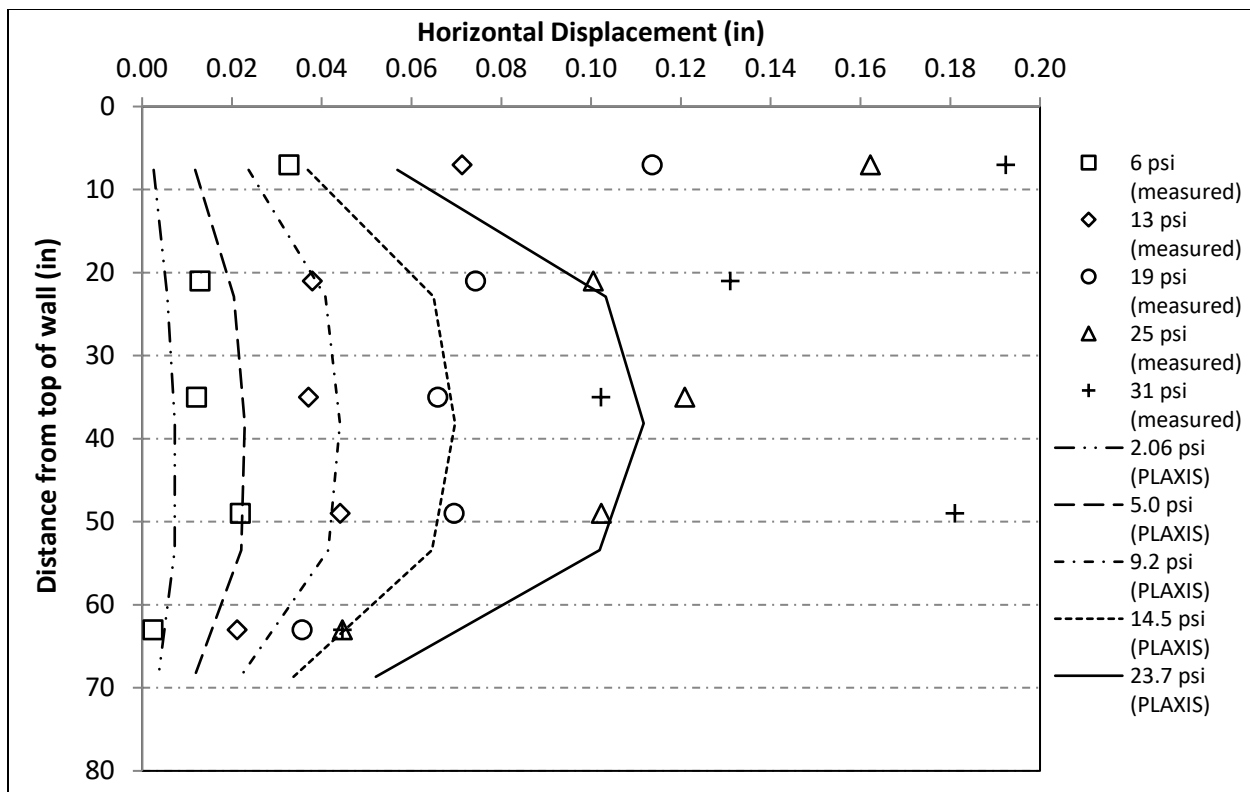


Figure 6-14 TF-7 horizontal displacement at 0 to 0.90 inches of vertical displacement.

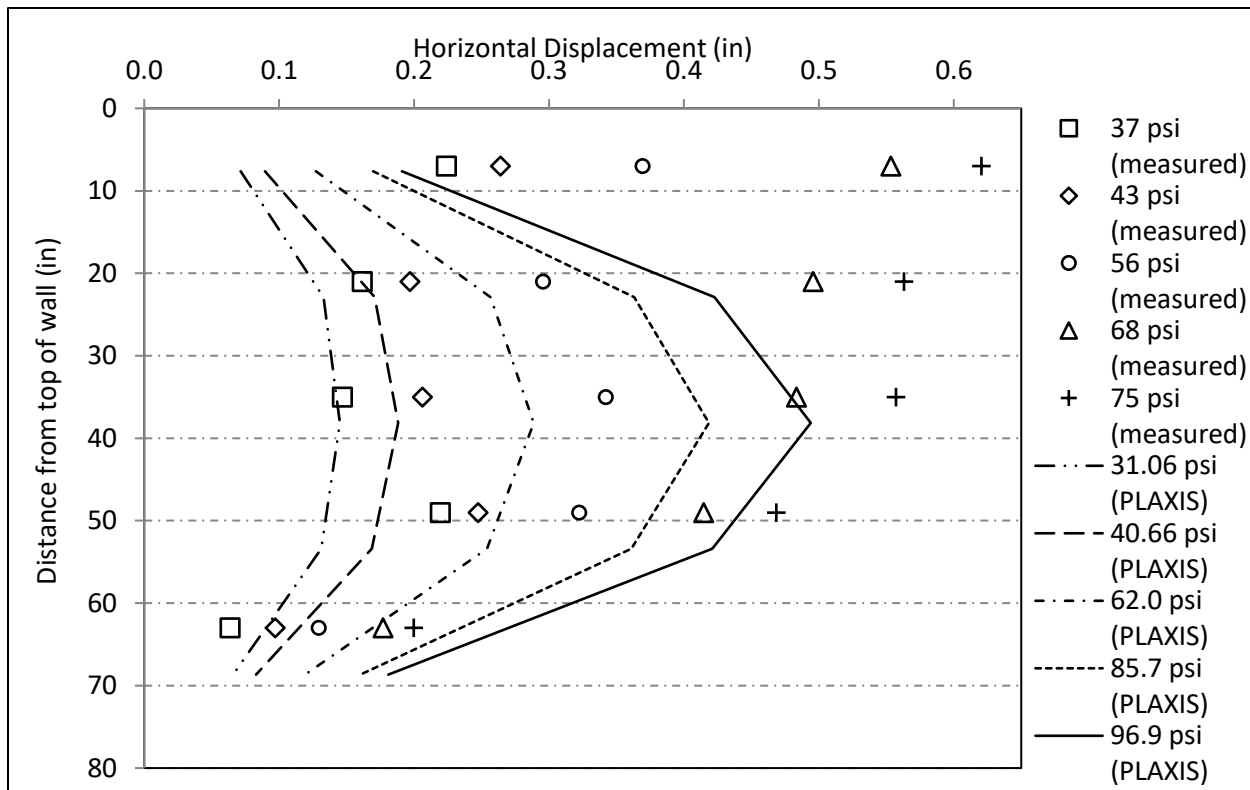


Figure 6-15 TF-7 horizontal displacement at 1.08 to 2.59 inches of vertical displacement.

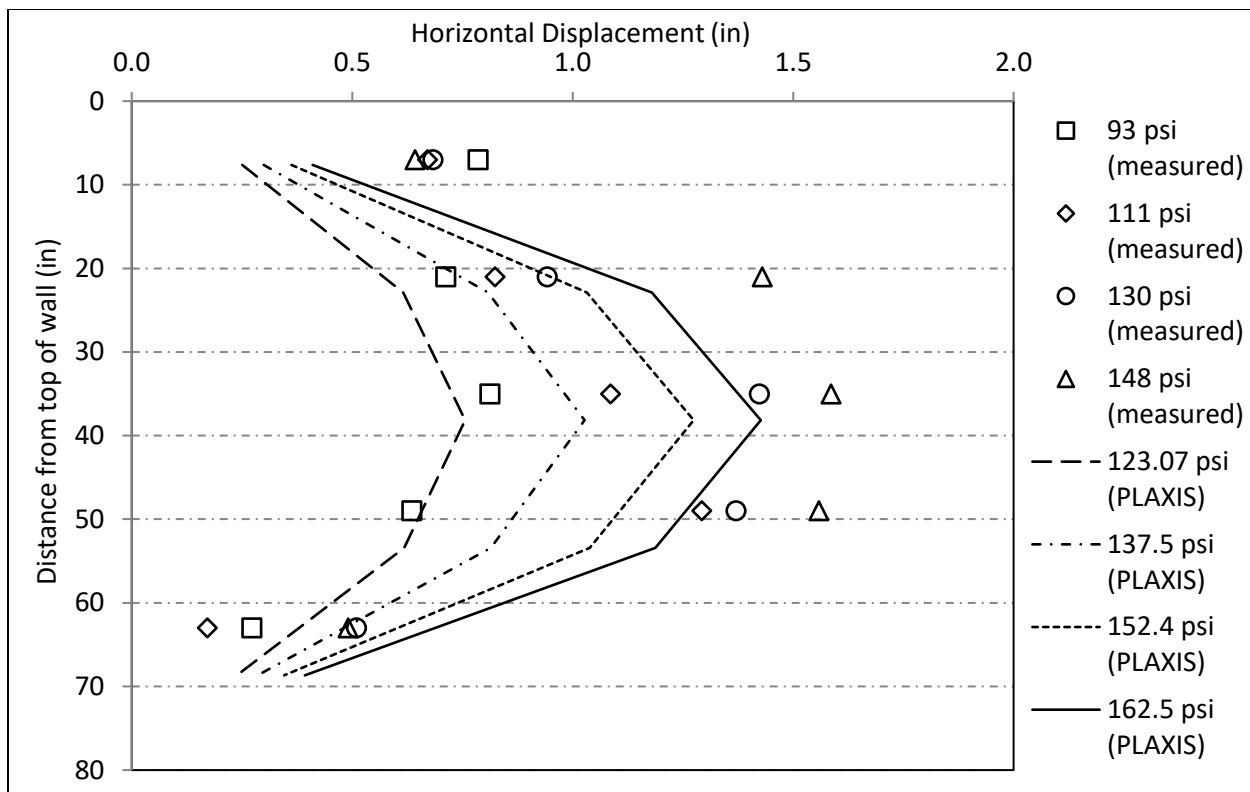


Figure 6-16 TF-7 horizontal displacements at 3.65 to 9.54 inches of vertical displacement.

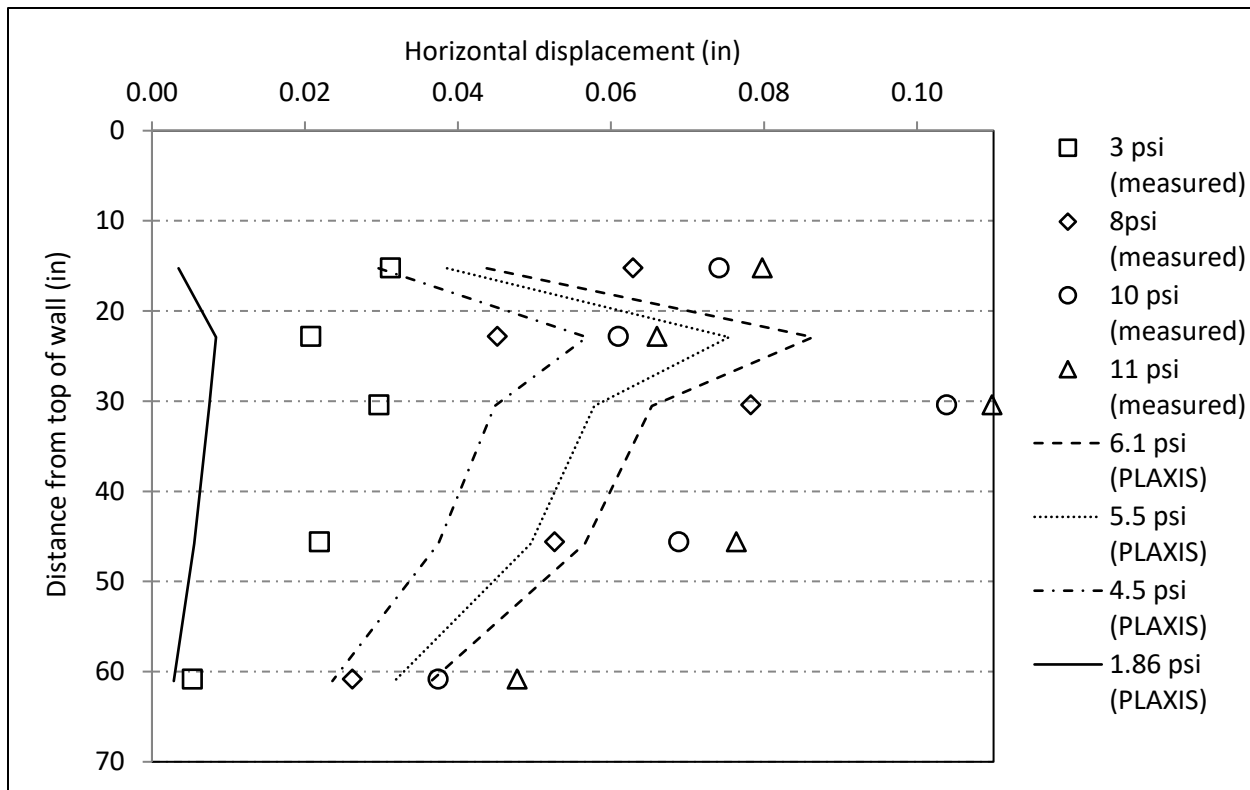


Figure 6-17 TF-10 horizontal displacements at 0 to 0.39 inches of vertical displacement.

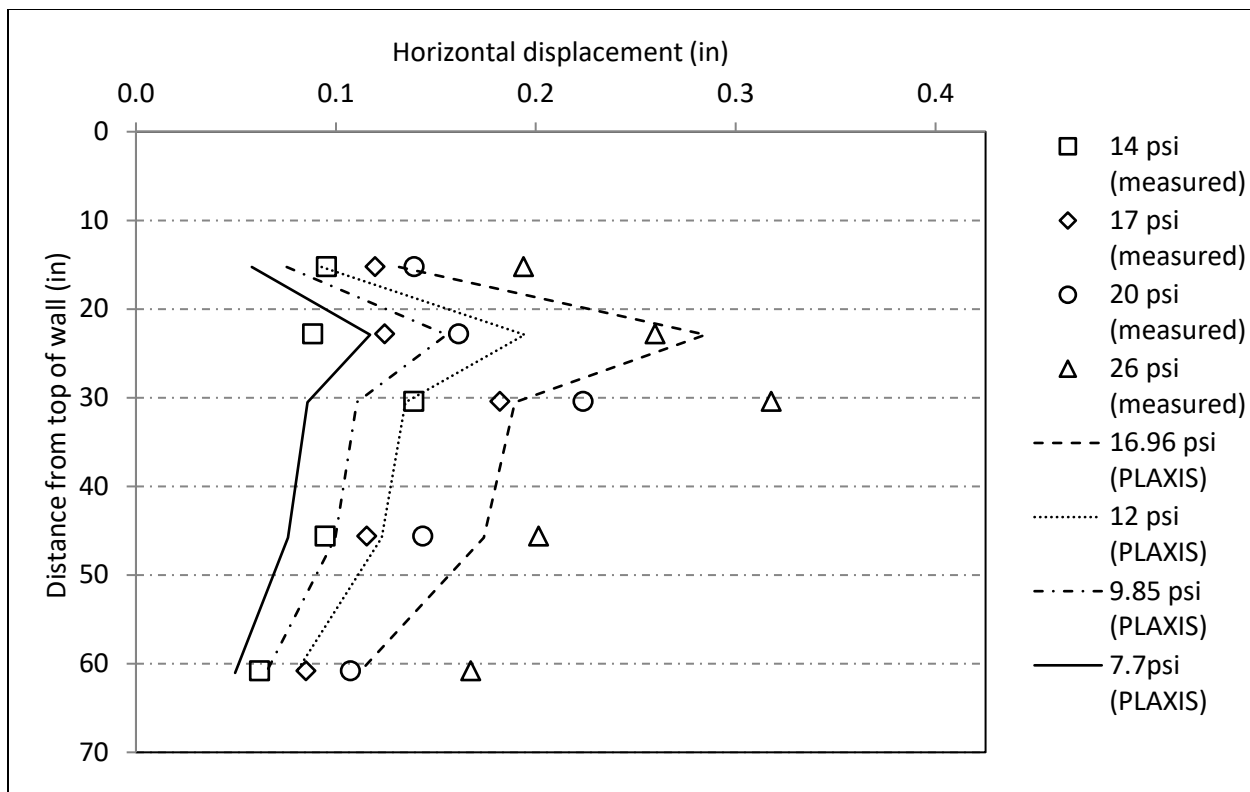


Figure 6-18 TF-10 horizontal displacements at 0.50 to 1.56 inches of vertical displacement.

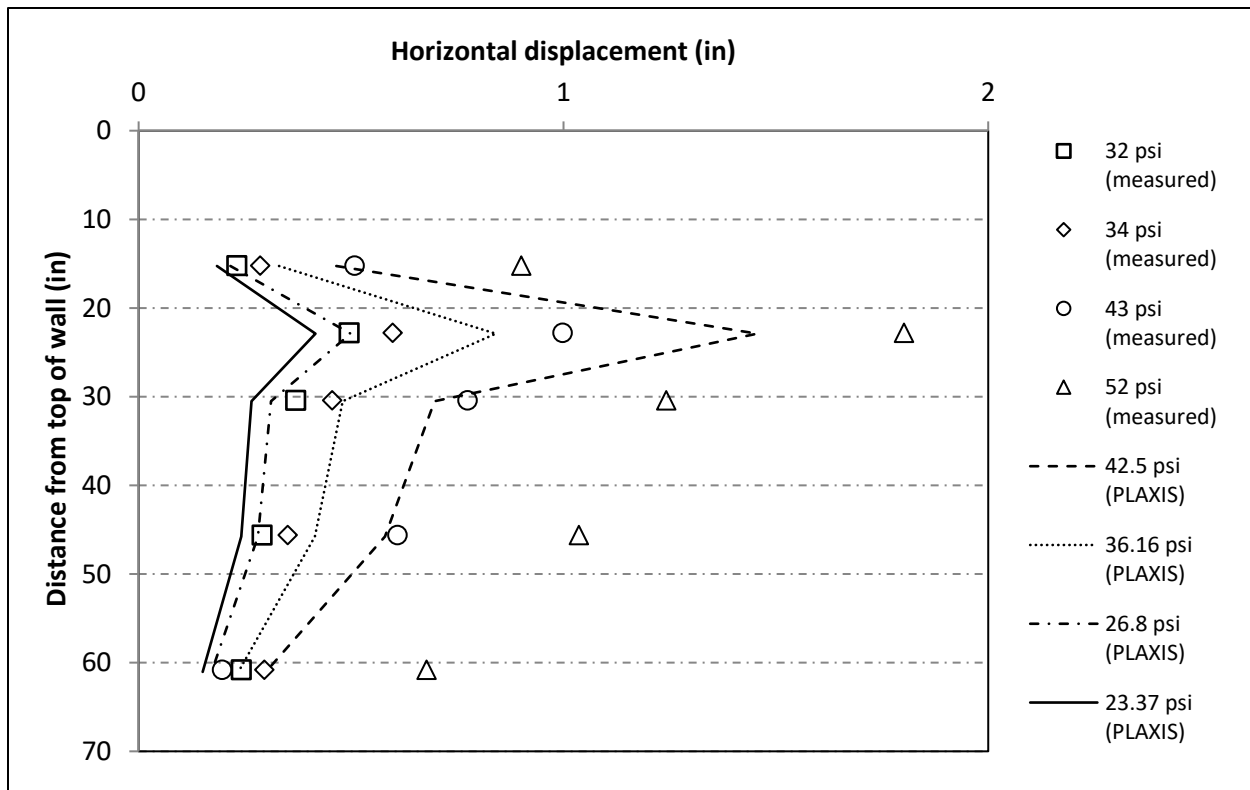


Figure 6-19 TF-10 horizontal displacements at 1.46 to 3.86 inches of vertical displacement.

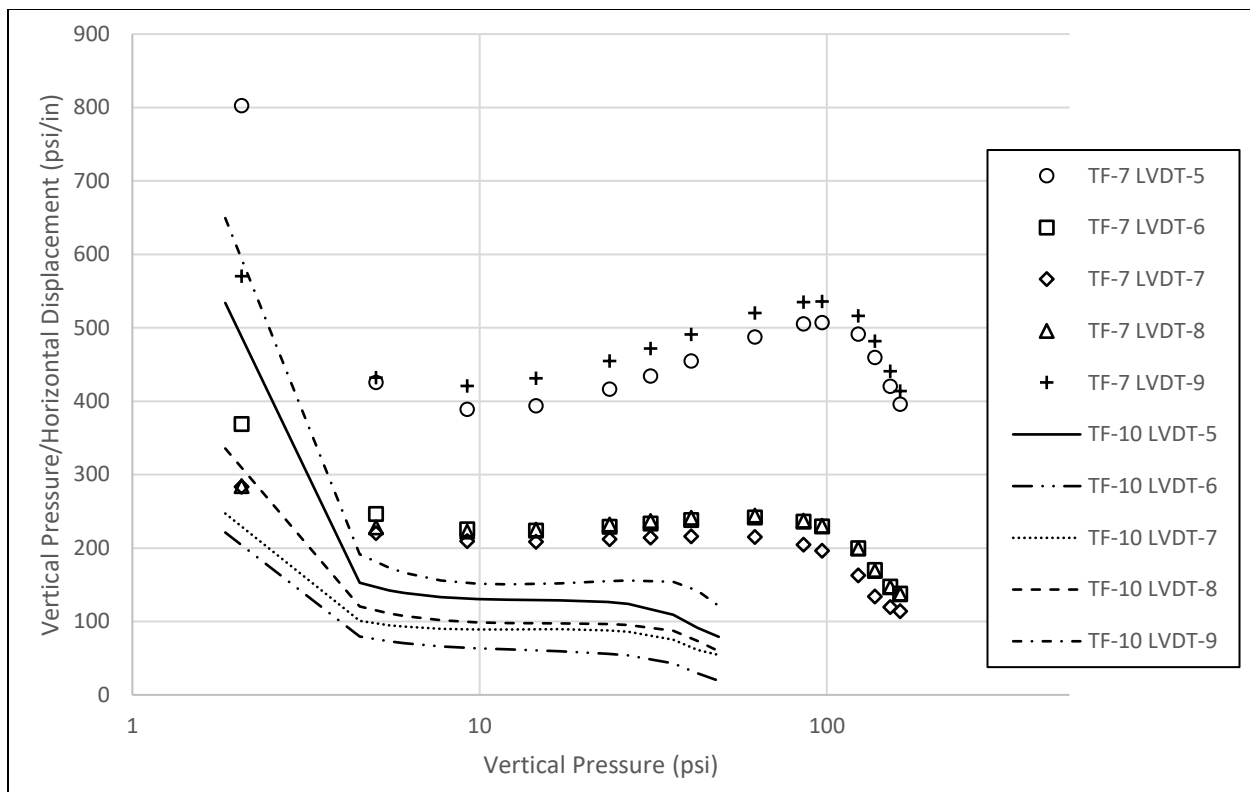


Figure 6-20 PLAXIS vertical pressure vs horizontal displacement behavior curves.

7. Conclusions

7.1 Conclusions

The development of a usable and practical 3D FEM model of GRS structures is a nuanced exercise, requiring careful consideration of available data and model parameters. The insights gained during the course of this study are:

- An optimization framework to generate Subloading t_{ij} parameters (or parameters of any more complex geomaterial constitutive model) can yield material parameters that generate model behavior very closely approximating available test data. Probabilistic optimization can help visualize parameter space and underscore the sensitivity of initialization. Depending on the model, initialization may have a significant or a negligible effect on optimization. Traditional error weighing techniques do not generate better optimization results when optimizing for the Subloading t_{ij} constitutive model.
- A good approximation of GRS pier behavior can be generated using an FEM model with Subloading t_{ij} user-define soil model in PLAXIS 3D.
- A spreading tendency is generated by the soil layers while a confining tendency is generated by the geotextile reinforcement. This is characterized by successive shear stress building up and unloading into the geotextile reinforcement. Three stress “zones” developed during loading of the GRS piers: a central “bearing column”, handling the bulk of the compressive stress, a transitional “shear zone”, in which shear stress develops in the form of bulb-like shapes, and a “confining shell”, providing confinement to the shear zone and without which progressive shear failure occurs. No clearly defined shear plane appeared during modeling of TF-10 which is consistent with test observations. The beginnings of a shear plane in TF-7 were witnessed during late-stage loading.
- The simulation failed to fully capture reinforcement mobilization in the GRS pier. This led to a failure to capture load distribution in early-stage loading and a failure to capture late-stage soil behavior due to prior strain development. This manifested as opposite curvatures of the vertical displacement testing data versus the PLAXIS results.
- Small strain behavior was not fully captured by the modeling. A certain randomness is present in the test data, indicating backfill material that is less likely to be as consistent as assumed and geotextile reinforcement with behavior likely less ideal than assumed. Displacement at the top and bottom of the piers during early-stage loading is not fully captured by the PLAXIS model. The PLAXIS models generated fairly consistent displaced shapes while the test data presented an evolving displaced shape during loading steps.
- Vertical pressure vs horizontal displacement ratios indicate that stress development primarily occurred in the central geotextile reinforcement layers of TF-7. This contrasts with stress development in TF-10, in which stress development was more distributed but

tended to be largest in the second from the top reinforcement layer and the backfill material above it.

7.2 Recommendations

Future investigation into this topic should include several areas not covered in this study. Of primary interest is the faced GRS pier behavior. The load testing indicated that the influence of the CMU facing seems to significantly affect the load-displacement behavior of the GRS piers. Stress development and bearing capacity of the GRS piers appear to increase with the addition of facing. The effect of the inclusion of facing in combination with reinforcement spacing should be investigated in a FEM environment.

Further study of interface properties, including the values assumed in Section 4.3 should be included in future study. The behavior of the interface elements is key to properly capturing mobilization of the reinforcement layers. Interface properties are also incredibly significant when attempting to model the facing and will need to be investigated alongside any modeling of the CMU facing. Further lab testing to establish interface properties may be warranted should available approximations fail to provide reasonable results.

The latest version of the Subloading t_{ij} model includes an unsaturated component. The behavior of the GRS piers is fundamentally unsaturated and to fully capture soil behavior the inclusion of unsaturated behavior should be investigated. In addition, further consideration of the applicability of the existing testing data should be included in any future work. The CD triaxial testing was conducted in a saturated state and at a relative compaction of 95% of the standard Proctor. Similarly, the large-scale direct shear testing failed to capture the same behavior as the CD triaxial testing (e.g., dilation of the sample at a confining stress of 5 psi).

8. References

- Abu-Farsakh, M., Ardah, A., & Voyiadjis, G. (2018, June). 3D Finite element analysis of the geosynthetic reinforced soil-integrated bridge system (GRS-IBS) under different loading conditions. *Transportation Geotechnics*, 15, 70-83. doi:10.1016/j.trgeo.2018.04.002
- Adams, M., Nicks, J., Stabile, T., Wu, J., Schlatter, W., & Hartmann, J. (2011, January). Geosynthetic Reinforced Soil Integrated Bridge System Synthesis Report. *Geosynthetic Reinforced Soil Integrated Bridge System Synthesis Report*. Federal Highway Administration. Retrieved from <https://www.fhwa.dot.gov/publications/research/infrastructure/structures/11027/index.cfm>
- American Concrete Institute. (2011). *Building Code Requirements for Structural Concrete (ACI 318-11)*. Farmington Hills, MI: American Concrete Institute.
- Ardah, A., Abu-Farsakh, M., & Voyiadjis, G. (2017, December). Numerical evaluation of the performance of a Geosynthetic Reinforced Soil-Integrated Bridge System (GRS-IBS) under different loading conditions. *Geotextiles and Geomembranes*, 45, 558-569. doi:10.1016/j.geotexmem.2017.07.005
- Bolton, M. D. (1986, March). The strength and dilatancy of sands. *Géotechnique*, 36, 65-78. doi:10.1680/geot.1986.36.1.65
- Cubrinovski, M., & Ishihara, K. (1999, October). Empirical Correlation between SPT N-Value and Relative Density for Sandy Soils. *Soils and Foundations*, 39, 61-71. doi:10.3208/sandf.39.5_61
- Desai, C. S., Zaman, M., Lightner, J. G., & Siriwardane, H. J. (1984, January). Thin-layer element for interfaces and joints. *International Journal for Numerical and Analytical Methods in Geomechanics*, 8, 19-43. doi:10.1002/nag.1610080103
- El-Sohby, M. A. (1969). Deformations of Sands Under Constant Stress Ratio. (pp. 111-119). International Society for Soil Mechanics and Geotechnical Engineering. Retrieved from <https://www.issmge.org/publications/publication/deformation-of-sands-under-constant-stress-ratios>
- Foreman-Mackey, D., Hogg, D. W., Lang, D., & Goodman, J. (2013, March). emcee: The MCMC Hammer. *Publications of the Astronomical Society of the Pacific*, 125, 306-312. doi:10.1086/670067
- Geo-slope, I. L. (n.d.). Parameterizing the Modified Cam Clay Model. *Parameterizing the Modified Cam Clay Model*. Sequent. Retrieved from <https://downloads.geoslope.com/geostudioresources/examples/11.2/SigmaW/Parameterizing%20the%20Modified%20Cam%20Clay%20Model.pdf>
- Goodman, J., & Weare, J. (2010, January). Ensemble samplers with affine invariance. *Communications in Applied Mathematics and Computational Science*, 5, 65-80. doi:10.2140/camcos.2010.5.65
- Goodman, R. E., Taylor, R. L., & Brekke, T. L. (1968, May). A Model for the Mechanics of Jointed Rock. *Journal of the Soil Mechanics and Foundations Division*, 94, 637-659. doi:10.1061/jsfea.0001133

- Hashiguchi, K. (1989). Subloading surface model in unconventional plasticity. *International Journal of Solids and Structures*, 25, 917-945. doi:10.1016/0020-7683(89)90038-3
- Helwany, S. M., Wu, J. T., & Froessl, B. (2003, June). GRS bridge abutments—an effective means to alleviate bridge approach settlement. *Geotextiles and Geomembranes*, 21, 177-196. doi:10.1016/s0266-1144(03)00004-9
- Helwany, S. M., Wu, J. T., & Kitsabunnarat, A. (2007, October). Simulating the Behavior of GRS Bridge Abutments. *Journal of Geotechnical and Geoenvironmental Engineering*, 133, 1229-1240. doi:10.1061/(asce)1090-0241(2007)133:10(1229)
- Huang, B., Bathurst, R. J., & Hatami, K. (2009, October). Numerical Study of Reinforced Soil Segmental Walls Using Three Different Constitutive Soil Models. *Journal of Geotechnical and Geoenvironmental Engineering*, 135, 1486-1498. doi:10.1061/(asce)gt.1943-5606.0000092
- Institute, A. C. (2011). Building Code Requirements for Structural Concrete (ACI 318-11). *Building Code Requirements for Structural Concrete (ACI 318-11)*. American Concrete Institute.
- Geo Institute (2019). Shear and Normal Stiffness of Interface Elements when Using Subloading tij. *Shear and Normal Stiffness of Interface Elements when Using Subloading tij*.
- Iwamoto, M. K. (2014, May). *Observations from Load Tests on Geosynthetic Reinforced Soil*. Ph.D. dissertation. Retrieved from <https://scholarspace.manoa.hawaii.edu/items/64ff765f-c3bb-45fa-90ba-de8dfeaf6dab>
- Kaya, L. (2016, August). *NUMERICAL LOAD TESTING OF a GEOSYNTHETIC REINFORCED SOIL*. Ph.D. dissertation. Retrieved September 21, 2023, from <https://scholarspace.manoa.hawaii.edu/items/407d09dc-6943-4d86-9b69-4415dbc0c8fb>
- Lade, P. V. (1977). Elasto-plastic stress-strain theory for cohesionless soil with curved yield surfaces. *International Journal of Solids and Structures*, 13, 1019-1035. doi:10.1016/0020-7683(77)90073-7
- Lade, P. V., & Duncan, J. M. (1975, October). Elastoplastic Stress-Strain Theory for Cohesionless Soil. *Journal of the Geotechnical Engineering Division*, 101, 1037-1053. doi:10.1061/ajgeb6.0000204
- Martin, J. P., Koerner, R. M., & Whitty, J. E. (1984). Experimental Friction Evaluation of Slippage Between Geomembranes, Geotextiles and Soils., (pp. 191-196).
- Matsuoka, H., & Nakai, T. (1974). Stress-Deformation and Strength Characteristics of Soil Under Three Different Principal Stresses. *Proceedings of the Japan Society of Civil Engineers*, 1974, 59-70. doi:10.2208/jscej1969.1974.232_59
- Mirmoradi, S. H., & Ehrlich, M. (2015, March). Numerical Evaluation of the Behavior of GRS Walls with Segmental Block Facing under Working Stress Conditions. *Journal of Geotechnical and Geoenvironmental Engineering*, 141. doi:10.1061/(asce)gt.1943-5606.0001235

- Müller, W. W., & Saathoff, F. (2015, June). Geosynthetics in geoenvironmental engineering. *Science and Technology of Advanced Materials*, 16, 034605. doi:10.1088/1468-6996/16/3/034605
- Nakai, T. (1989, March). An Isotropic Hardening Elastoplastic Model for Sand Considering the Stress Path Dependency in Three-Dimensional Stresses. *Soils and Foundations*, 29, 119-137. doi:10.3208/sandf1972.29.119
- Nakai, T. (2013). *Constitutive modeling of geomaterials : principles and applications*. Taylor & Francis.
- Nakai, T. (n.d.). tij地盤解析研究会 . tij地盤解析研究会 . Retrieved May 26, 2024, from <https://geo-tij.jp/>
- Nakai, T., & Hinokio, M. (2004, April). A Simple Elastoplastic Model for Normally and Over Consolidated Soils with Unified Material Parameters. *Soils and Foundations*, 44, 53-70. doi:10.3208/sandf.44.2_53
- Nakai, T., & Matsuoka, H. (1986, September). A Generalized Elastoplastic Constitutive Model for Clay in Three-Dimensional Stresses. *Soils and Foundations*, 26, 81-98. doi:10.3208/sandf1972.26.3_81
- Nakai, T., & Mihara, Y. (1984, June). A New Mechanical Quantity for Soils and its Application to Elastoplastic Constitutive Models. *Soils and Foundations*, 24, 82-94. doi:10.3208/sandf1972.24.2_82
- Nakai, T., & Shahin, H. M. (2013, January). Simple and Unified Modelong of Time-Dependent Behavior for Various Geomaterials. *Springer series in geomechanics and geoengineering*, 617-625. doi:10.1007/978-3-642-32814-5_83
- Nakai, T., Shahin, H. M., Kikumoto, M., Kyokawa, H., Zhang, F., & Farias, M. M. (2011, December). A Simple and Unified Three-Dimensional Model to Describe Various Characteristics of Soils. *Soils and Foundations*, 51, 1149-1168. doi:10.3208/sandf.51.1149
- Newland, P. L., & Allely, B. H. (1959, December). Volume Changes During Undrained Triaxial Tests on Saturated Dilatant Granular Materials. *Géotechnique*, 9, 174-182. doi:10.1680/geot.1959.9.4.174
- Newville, M., Otten, R., Nelson, A., Stensitzki, T., Ingargiola, A., Allan, D., . . . Caldwell, S. (2023). lmfit/lmfit-py: 1.2.1. *Zenodo*. doi:<https://doi.org/10.5281/zenodo.7887568>
- Nicks, J., Adams, M. T., Ooi, P., & Stabile, T. (2013, August). Geosynthetic Reinforced Soil Performance Testing—Axial Load Deformation Relationships. *FHWA*. Retrieved September 22, 2023
- Pham, T. Q. (2009, February). *Investigating Composite Behavior of Geosynthetic-Reinforced Soil (GRS)* Mass. Ph.D. dissertation.
- Pires-Sturm, A., Jaeger, R., & DeJong, J. (2022, September). Estimating Maximum and Minimum Void Ratio from Index Parameters. Association of State Dam Safety Officials, Inc.
- Roscoe, K. H., & Burland, J. B. (1968, January). *On the Generalised stress-strain Behaviour of 'wet' Clay*. (E. plasticity, F. A. Leckie, & J. Heyman, Eds.) Cambridge University Press,.

- Shen, P., Han, J., Zornberg, J. G., Morsy, A. M., Leshchinsky, D., Tanyu, B. F., & Chen, X. (2019, June). Two and three-dimensional numerical analyses of geosynthetic-reinforced soil (GRS) piers. *Geotextiles and Geomembranes*, 47, 352-368. doi:10.1016/j.geotexmem.2019.01.010
- Shibata, T. (1963, January). On the Volume Changes of Normally-Consolidated Clays. *Annals of Disaster Prevention Research Institute, Kyoto University*, 6, 128–134. doi:10.2472/jsms.12.264
- Storn, R., & Price, K. (1997). Differential Evolution – A Simple and Efficient Heuristic for global Optimization over Continuous Spaces. *Journal of Global Optimization*, 11, 341-359. doi:10.1023/a:1008202821328
- Taeb, A., & Ooi, P. S. (2020, January). Comparison of Field Behavior with Results from Numerical Analysis of a Geosynthetic Reinforced Soil Integrated Bridge System Subjected to Thermal Effects. *Transportation Research Record: Journal of the Transportation Research Board*, 2674, 294-306. doi:10.1177/0361198119899043
- Tatsuoka, F. (1980). Stress-strain behavior of an idealized anisotropic granular material. *Soils and Foundations*, 20, 75-90. doi:10.3208/sandf1972.20.3_75
- Tatsuoka, F., Tateyama, M., Koda, M., Kojima, K.-i., Yonezawa, T., Shindo, Y., & Tamai, S.-i. (2016, September). Research and construction of geosynthetic-reinforced soil integral bridges. *Transportation Geotechnics*, 8, 4-25. doi:10.1016/j.trgeo.2016.03.006
- Tatsuoka, F., Tateyama, M., Uchimura, T., & Koseki, J. (1997, January). Geosynthetic-Reinforced Soil Retaining Walls as Important Permanent Structures 1996 - 1997 Mercer Lecture. *Geosynthetics International*, 4, 81-136. doi:10.1680/gein.4.0090
- Tsesarsky, M., & Talesnick, M. L. (2006, October). Mechanical response of a jointed rock beam—numerical study of centrifuge models. *International journal for numerical and analytical methods in geomechanics*, 31, 977-1006. doi:10.1002/nag.568
- Wu, J. T., & Ooi, P. S. (2015, February). Synthesis of Geosynthetic Reinforced Soil (GRS) Design Topics. *Synthesis of Geosynthetic Reinforced Soil (GRS) Design Topics*. Federal Highway Administration. Retrieved July 7, 2024
- Youd, T. L. (1973, January). Factors Controlling Maximum and Minimum Densities of Sands. (pp. 98-112). American Society for Testing and Materials. doi:10.1520/STP37866s
- Zhao, R., Zheng, K., Wang, X., Jia, H., Li, X., Zhang, Q., . . . Yu, C. (2022, December). State-of-the-art and annual progress of bridge engineering in 2021. *Advances in Bridge Engineering*, 3. doi:10.1186/s43251-022-00070-1
- Zhao, R., Zheng, K., Wei, X., Jia, H., Liao, H., Li, X., . . . Yu, C. (2021, December). State-of-the-art and annual progress of bridge engineering in 2020. *Advances in Bridge Engineering*, 2. doi:10.1186/s43251-021-00050-x

Zheng, Y., & Fox, P. J. (2016, May). Numerical Investigation of Geosynthetic-Reinforced Soil Bridge Abutments under Static Loading. *Journal of Geotechnical and Geoenvironmental Engineering*, 142. doi:10.1061/(asce)gt.1943-5606.0001452

Zheng, Y., Fox, P. J., & McCartney, J. S. (2018, June). Numerical simulation of the deformation response of geosynthetic reinforced soil mini-piers. *Geosynthetics International*, 25, 271-286. doi:10.1680/jgein.18.00007

9. Appendix A

```
1 #This program performs a parameter optimization for Subloading tij geomaterials
  model based on triaxial testing data
2 # (axial strain, deviator stress, volumetric strain, and a known confining stress)
3 # and isotropic consolidation results (void ratio and mean pressure).
4 import pandas as pd
5 import numpy as np
6 import os
7 from lmfit import Model
8 import corner
9 import matplotlib.pyplot as plt
10
11 # Function for error handling for "Subloading_tij.exe" that cannot be intrepreted
  by the reader
12 def format_exp(x):
13     if isinstance(x, float):
14         return x
15     if x == "-Infinity" or "Infinity":
16         return 10**300.5
17     tmpp = x.rfind('+', 1)
18     tmpm = x.rfind('-', 1)
19     if tmpp == -1:
20         x = x[:tmpm-1] + "e" + x[tmpm:]
21     if tmpm == -1:
22         x = x[:tmpp-1] + "e" + x[tmpp:]
23     return x
24
25 #Defining the Subloading tij model that receives parameter inputs and outputs
  calculated Triaxial data and
26 # Isotropic Consolidation data
27 def tijmodelfn(astrains, Lamda, Rcs, Beta, a, N, Kappa, axk):
28
29     #Defining non iteration parameters/constants these are standard Subloading tij
  parameters
30     e0 = 0.3341
31     e_max = 0.551
32     pl = 1
33     aAF = a
34     aIC = a
35     Qw0 = 0
36     bw = 0
37     Pa = 14.7
38     powerIC = 2
39     wgt_IC = 1
40     pw = 1
41     bXk = 0
42     w_hpSoft = 1
43     Poisson = 0.2
44     axk = int(round(axk))
45
46     #Writing parameter values to array to be written to the input files
47     tparams = [Lamda, Kappa, Rcs, N, Poisson, Beta, e_max, e0, aAF, aIC, pl, axk,
      Qw0, bw, pw, bXk, Pa, powerIC, wgt_IC, w_hpSoft]
48     tparams2 = np.array([0.003, 1.e-7, 0.0, 1.e-7, 0.0, 0.0, 1.e10, 1.0, 0.0])
49     tparams3 = np.array([2.0, 5.0, 2.0])
50
51     #Writing to/creating the Subloading_tij.exe parameter input file
```



```

100     print(temp['εv'])
101     temp['εv'] = temp['εv'].map(format_exp)
102
103     #Dimensioning a results array and writing to it.
104     SS = np.empty([1013, 2])
105
106     SS[0:301, :] = temp[['εv', 'q']].to_numpy(dtype='float64')
107
108     #Deleting results allowing Subloading_tij.exe to be run again.
109     os.remove("Ana.cal")
110
111     #Defining starting void ratio for second confining stress
112     tparams[7] = 0.3331
113
114     #Rewriting parameter file using updataed parameter values, this might be
115     #optimized by replacing with a text search
116     # and replace.
117     with open('Para.txt', 'w') as para:
118         arglist = ["Model      1", "iVersion    3", "iCyclic&iCreep    0", "
119         iAssoc    3", "Elastic      N"]
120         desc = ["[1: Subloading tij,    2: Cam clay]", "[0: original,    3:
121         alternative, 4: alternative4",
122             "[0: no-creep,        1: creep,        10: cyclic]",
123             "[0: (AF+IC) for original, 3: (AF+IC) for alternative, 1: (AF
124 ) for both iVersions",
125             "[H: non-linear Hookean,    N: no-tension elastic]"]
126         tempdf = pd.DataFrame(desc, index=arglist, columns=[''])
127         tempdfAsString = tempdf.to_string(header=False, index=True)
128         para.write(tempdfAsString)
129         para.write("\nLamda\tKappa\tRcs N\tPoisson\tBeta\te_max\te0\tAF*\tIC*\t
130         pl\taxk\tQw0\tbw*\tpw\tbxk\tPa\tPowerIC\twgt_IC\tw_hpSoft\n")
131         for param in tparams:
132             para.write("%s" % param)
133             para.write("\t")
134             para.write("\n\nLamda_alfa\tVoiddot_ref\tVoiddot_min\tVoiddot_ini\t
135             bR_faster\tbR_slower\tVoiddot_max\tw_Vcrp\tw_Psi\n")
136             for param in tparams2:
137                 para.write("%s" % param)
138                 para.write("\t")
139                 para.write("\n\nna_cyc\tkm_cyc\tkn_cyc\n")
140                 for param in tparams3:
141                     para.write("%s" % param)
142                     para.write("\t")
143
144         para.close()
145
146     #Rewriting stress path file, confining stress 10.0 psi
147     with open('Path.txt', 'w') as path:
148         path.write("NoPath= 1\n")
149         path.write("InitialStresses= 10.0\t10.0\t10.0\t0.0\t0.0\t0.0\n")
150         path.write("Triaxial\tDrain\tsrConstant\t0.15\t300\t1")
151
152     path.close()
153
154     #Running Subloading_tij.exe
155     os.system(r'"C:\Users\Miles Drazkowski\Documents\Miles Drazkowski\Thesis\

```

```

149 Optimization Paramters\Without 20psi\with consol\SubloadingTij_a.exe")
150
151     #Reading results and error handling
152     temp = pd.read_fwf('Ana.cal', encoding='shift_jis', colspecs=colspecs, names=
153     names, skiprows=10)
154     temp.fillna(value=10 ** 101.5, inplace=True)
155
156     if temp['q'].dtypes == 'object':
157         temp['q'] = temp['q'].map(format_exp)
158
159     if temp['ev'].dtypes == 'object':
160         print(temp['ev'])
161         temp['ev'] = temp['ev'].map(format_exp)
162
163     #Writing to Results array
164     SS[301:602, :] = temp[['ev', 'q']].to_numpy(dtype='float64')
165
166     os.remove("Ana.cal")
167
168     #Initial void ratio for next stress path
169     tparams[7] = 0.3233
170
171     #Rewriting parameter file using updataed parameter values
172     with open('Para.txt', 'w') as para:
173         arglist = ["Model      1", "iVersion    3", "iCyclic&iCreep    0",
174         "iAssoc    3", "Elastic      N"]
175         desc = "[1: Subloading tij,    2: Cam clay]", "[0: original,    3:
176         alternative, 4: alternative4",
177         "[0: no-creep,        1: creep,        10: cyclic]",
178         "[0: (AF+IC) for original, 3: (AF+IC) for alternative, 1: (AF
179         ) for both iVersions]",
180         "[H: non-linear HooKean,    N: no-tension elastic]"
181         tempdf = pd.DataFrame(desc, index=arglist, columns=[''])
182         tempdfAsString = tempdf.to_string(header=False, index=True)
183         para.write(tempdfAsString)
184         para.write("\nLamda\tKappa\tRcs N\tPoisson\tBeta\te_max\te0\tAF*\tIC*\t
185         pl\taxk\tQw0\tbw*\tpw\tbxk\tPa\tPowerIC\twgt_IC\tw_hpSoft\n")
186         for param in tparams:
187             para.write("%s" % param)
188             para.write("\t")
189             para.write("\nLamda_alfa\tVoiddot_ref\tVoiddot_min\tVoiddot_ini\t
190             bR_faster\tbR_slower\tVoiddot_max\tw_Vcrp\tw_Psi\n")
191             for param in tparams2:
192                 para.write("%s" % param)
193                 para.write("\t")
194                 para.write("\nna_cyc\tkm_cyc\tkn_cyc\n")
195                 for param in tparams3:
196                     para.write("%s" % param)
197                     para.write("\t")
198
199             para.close()
200
201             #Rewriting stress path file, confining stress 30.0 psi
202             with open('Path.txt', 'w') as path:
203                 path.write("NoPath= 1\n")
204                 path.write("InitialStresses= 30.0\t30.0\t30.0\t0.0\t0.0\t0.0\n")

```

```

199         path.write("Triaxial\tDrain\tsrConstant\t0.15\t300\t1")
200
201     path.close()
202
203     #Running Subloading_tij.exe
204     os.system(r"C:\Users\Miles Drakowski\Documents\Miles Drakowski\Thesis\
205     Optimization Paramaters\Without 20psi\with consol\SubloadingTij_a.exe")
206
207     #Reading results and error handling
208     temp = pd.read_fwf('Ana.cal', encoding='shift_jis', colspecs=colspecs, names=
209     names, skiprows=10)
210     temp.fillna(value=10 ** 101.5, inplace=True)
211
212     if temp['q'].dtypes == 'object':
213         temp['q'] = temp['q'].map(format_exp)
214
215     if temp['ev'].dtypes == 'object':
216         print(temp['ev'])
217         temp['ev'] = temp['ev'].map(format_exp)
218
219     #Writing to Results array
220     SS[602:903, :] = temp[['ev', 'q']].to_numpy(dtype='float64')
221
222     os.remove("Ana.cal")
223
224     #Initial void ratio for Isotropic consolidation.
225     tparams[7] = 0.3341
226
227     #Rewriting parameter file using updated parameter values
228     with open('Para.txt', 'w') as para:
229         arglist = ["Model      1", "iVersion    3", "iCyclic&iCreep      0", "
230         iAssoc      3", "Elastic      N"]
231         desc = "[1: Subloading tij,    2: Cam clay]", "[0: original,      3:
232         alternative, 4: alternative4]",
233             "[0: no-creep,          1: creep,          10: cyclic]",
234             "[0: (AF+IC) for original, 3: (AF+IC) for alternative, 1: (AF
235 ) for both iVersions]",
236             "[H: non-linear Hookean,  N: no-tension elastic]"
237         tempdf = pd.DataFrame(desc, index=arglist, columns=[''])
238         tempdfAsString = tempdf.to_string(header=False, index=True)
239         para.write(tempdfAsString)
240         para.write(
241             "\n\nLamda\Kappa\Rcs      N\Poisson\Beta\te_max\te0\taAF*\taIC*\tpl\t
242             axk\tQw0\tbw*\tpw\tbxk\tPa\tpowerIC\twgt_IC\tw_hpSoft\n")
243         for param in tparams:
244             para.write("%s" % param)
245             para.write("\t")
246             para.write(
247                 "\n\nLamda_alfa\Voiddot_ref\Voiddot_min\Voiddot_ini\tbR_faster\t
248             bR_slower\Voiddot_max\tw_Vcrp\tw_Psi\n")
249             for param in tparams2:
250                 para.write("%s" % param)
251                 para.write("\t")
252                 para.write("\n\nna_cyc\tkm_cyc\tkn_cyc\n")
253                 for param in tparams3:
254                     para.write("%s" % param)

```

```

248         para.write("\t")
249
250     para.close()
251
252     #Writing Stress Path file for isotropic consolidation with intial
253     # consolidation of 5.0 psi, loading to 50.0 psi
254     # and unloading to 5.0 psi
255     with open('Path.txt', 'w') as path:
256         path.write("NoPath= 2\n")
257         path.write("InitialStresses= 5.0\t5.0\t5.0\t0.0\t0.0\t0.0\n")
258         path.write("Consolidation\tOneDimensional\t50\t540\t10\n")
259         path.write("Consolidation\tOneDimensional\t5\t540\t10")
260
261     path.close()
262
263     #Running subloading_tij.exe
264     os.system(r'"C:\Users\Miles Drazkowski\Documents\Miles Drazkowski\Thesis\
265 Optimization Paramaters\Without 20psi\with consol\SubloadingTij_a.exe"')
266
267     #Reading results and error handling
268     colspecs = [(231, 241), (154, 167)]
269     names = ["e", "s1"]
270     temp = pd.read_fwf('Ana.cal', encoding='shift_jis', colspecs=colspecs, names=
271     names, skiprows=10)
272     temp.fillna(value=10 ** 101.5, inplace=True)
273
274     if temp['s1'].dtypes == 'object':
275         print(temp['s1'])
276         try:
277             temp['s1'] = temp['s1'].astype('float64')
278         except:
279             temp['s1'] = temp['s1'].map(format_exp)
280         else:
281             temp['s1'] = temp['s1'].astype('float64')
282
283     if temp['e'].dtypes == 'object':
284         print(temp['e'])
285         try:
286             temp['e'] = temp['e'].astype('float64')
287         except:
288             temp['e'] = temp['e'].map(format_exp)
289         else:
290             temp['e'] = temp['e'].astype('float64')
291
292     #Writing to results array
293     SS[904:1013, :] = temp[['e', 's1']].to_numpy(dtype='float64')
294
295     os.remove("Ana.cal")
296
297     SS = SS.astype('float64')
298
299     #Converting from percent strain to decimal strain
300     SS[0:903, 0] = SS[0:903, 0] / 100
301
302     #Flattening results into 1D array
303     SS = SS.flatten('F')

```

```

301
302     return SS
303
304 #Reading triaxial data and loading in data arrays
305 data = np.loadtxt("Triaxial Test Data and Consol.20.txt", dtype='float64')
306 xdata = data[:, 0]
307 xdata = np.resize(xdata, 2026)
308 ydata = data[:, 1:3]
309 ydata = ydata.flatten('F')
310 #Loading weights for error calculation (optional)
311 fweights = np.loadtxt('weightsforfitting.4124.txt', dtype='float64')
312 fweights=fweights.flatten('F')
313
314 #Defining parameter array and Model class
315 tparams = ['Lamda', 'Rcs', 'a', 'Beta', 'N', 'Kappa', 'axk']
316 tijmodel = Model(tijmodelfn, param_names=tparams)
317
318 print(tijmodel.param_names)
319
320 #Define Parameter class and add to Model
321 paramin = tijmodel.make_params(Lamda=dict(value=0.02073268, max=0.025, min=0.019
   ),
322                               Rcs=dict(value=5.08521251, max=5.5, min=4.5),
323                               Beta=dict(value=1.05154567, max=3, min=1), a=dict(
   value=103.324742, max=1000, min=10),
324                               N=dict(value=0.35760210, max=0.551, min=0.3323),
325                               Kappa=dict(value=0.00160315, max=0.0019, min=0.
   0013),
326                               axk=dict(value=1, max=50, min=1))
327
328 #Optimization algorithm keyword arguements and optimization
329 emcee_kws = dict(steps=4500, nwalkers=500, burn=1000, is_weighted=False)
330 #difev_kws = dict(atol=0, tol=0, maxiter=10000000)
331 paramopt = tijmodel.fit(data=ydata, astrains=xdata, nan_policy='omit', params=
   paramin, method='emcee', fit_kws=emcee_kws)
332 #paramopt = tijmodel.fit(data=ydata, astrains=xdata, weights=fweights, nan_policy
   ='omit', params=paramin,
333 #method='differential_evolution', fit_kws=difev_kws)
334
335
336 #Writing Optimization results to file and printing results as well as confidence
   intervals
337 with open('Optparatest20D.4-15-24.txt', 'w') as opt:
338     opt.write(paramopt.fit_report())
339 opt.close()
340 print(paramopt.fit_report())
341 print(paramopt.ci_report())
342
343 #Plotting emcee acceptance fraction
344 plt.plot(paramopt.acceptance_fraction, 'o')
345 plt.title('Test20.0')
346 plt.xlabel('walker')
347 plt.ylabel('acceptance fraction')
348 plt.savefig('AcceptanceFractest20.update.3.png')
349
350 #Plotting posterior distributions

```

```
351 para_plot = corner.corner(paramopt.flatchain, labels=paramopt.var_names, truths=
  list(paramopt.params.valuesdict().values()))
352 para_plot.savefig('paramplotvoltest20.update.3.png')
353
354 plt.show()
355 ara_plot.show()
```

10. Appendix B

```
1 import pandas as pd
2 import numpy as np
3 import os
4 from scipy.optimize import minimize_scalar
5
6 count = 1
7
8 #Error Handling, handles Subloading_tij.exe outputs that are NAN
9 def format_exp(x):
10     if isinstance(x, float):
11         return x
12     if x == "-Infinity" or "Infinity":
13         return 10**300.5
14     tmpp = x.rfind('+', 1)
15     tmpm = x.rfind('-', 1)
16     if tmpp == -1:
17         x = x[:tmpm-1] + "e" + x[tmpm:]
18     if tmpm == -1:
19         x = x[:tmpp-1] + "e" + x[tmpp:]
20     return x
21
22 def tijmodelfn(e0, itr):
23
24 #Input of final stress state for layered condition in which soil layers are placed
25 #and compacted in succesion
26 stress_states = np.array([[7.332556785, 0.332556785],
27                           [7.997670356, 0.997670356],
28                           [8.662783927, 1.662783927],
29                           [9.327897497, 2.327897],
30                           [9.993011068, 2.993011068],
31                           [10.65812464, 3.658124638],
32                           [11.32323821, 4.323238209],
33                           [11.98835178, 4.98835178],
34                           [12.65346535, 5.65346535],
35                           [13.31857892, 6.318578921]])
36
37 inputstress = np.array([stress_states[itr,0], stress_states[itr,1]])
38
39 # Parameters from optimization
40 N = 0.3576
41 e_max = 0.551
42 pl = 1
43 a = 103.32
44 aAF = a
45 aIC = a
46 Qw0 = 0
47 bw = 0
48 Pa = 14.7
49 powerIC = 2
50 wgt_IC = 1
51 pw = 1
52 bXk = 0
53 Kappa = 0.0016
54 w_hpSoft = 1
55 Poisson = 0.2
56 Lamda = 0.0207
```

```

56     Rcs = 5.085
57     Beta = 1.052
58     axk = 1
59
60 #Parameter Array
61     tparams = [Lamda, Kappa, Rcs, N, Poisson, Beta, e_max, e0.item(), aAF, aIC,
62     pl, axk, Qw0, bw, pw, bxk, Pa, powerIC, wgt_IC, w_hpSoft]
63     tparams2 = np.array([0.003, 1.e-7, 0.0, 1.e-7, 0.0, 0.0, 1.e10, 1.0, 0.0])
64     tparams3 = np.array([2.0, 5.0, 2.0])
65
66 #Running model for given iteration, model parameters, and stress state, Input for
67 #parameter text file
68     with open('Para.txt', 'w') as para:
69         arglist = ["Model      1", "iVersion    3", "iCyclic&iCreep    0", "
70 iAssoc    3", "Elastic      N"]
71         desc = "[[1: Subloading tij,    2: Cam clay]", "[0: original,    3:
72 alternative, 4: alternative4]",
73             "[0: no-creep,        1: creep,        10: cyclic]",
74             "[0: (AF+IC) for original, 3: (AF+IC) for alternative, 1: (AF
75 ) for both iVersions]",
76             "[H: non-linear Hookean,    N: no-tension elastic]"]
77         tempdf = pd.DataFrame(desc, index=arglist, columns=[''])
78         tempdfAsString = tempdf.to_string(header=False, index=True)
79         para.write(tempdfAsString)
80         para.write(
81             "\n\nLamda\tKappa\tRcs      N\tPoisson\tBeta\te_max\tte0\ttaAF*\taIC*\tpl\t
82 axk\tQw0\tbw\tbw\tbxk\tPa\tpowerIC\twgt_IC\tw_hpSoft\n")
83         for param in tparams:
84             para.write("%s" % param)
85             para.write("\t")
86         para.write(
87             "\n\nLamda_alfa\tVoiddot_ref\tVoiddot_min\tVoiddot_ini\tbR_faster\t
88 bR_slower\tVoiddot_max\tw_Vcrp\tw_Psi\n")
89         for param in tparams2:
90             para.write("%s" % param)
91             para.write("\t")
92         para.write("\n\nna_cyc\tkm_cyc\tkn_cyc\n")
93         for param in tparams3:
94             para.write("%s" % param)
95             para.write("\t")
96
97     para.close()
98
99 #Input for stress path text file
100    with open('Path.txt', 'w') as path:
101        path.write("NoPath= 2\n")
102        path.write("InitialStresses= 0.332556785,\t0.332556785,\t0.332556785,\t0.
103 0,\t0.0,\t0.0\n")
104        path.write("Consolidation\tOneDimensional\t%s\t1000\t10\n" % inputstress[
105 0])
106        path.write("Consolidation\tOneDimensional\t%s\t1000\t10\n" % inputstress[
107 1])
108
109    path.close()
110
111 #Run Subloadingtij.exe from given file path (same path as Path and Para files)

```

```

102     os.system(r'"C:\Users\Miles Drazkowski\Documents\Miles Drazkowski\Thesis\Ko
Calculation\SubloadingTij_a.exe"')
103
104 #Pull resulting void ratio from results
105     colspecs = [(231, 241)]
106     names = ["e"]
107     temp = pd.read_fwf('Ana.cal', encoding='shift_jis', colspecs=colspecs, names=
names, skiprows=10)
108
109 #Error Handling
110     temp.fillna(value=10 ** 101.5, inplace=True)
111     if temp['e'].dtypes == 'object':
112         print(temp['e'])
113         try:
114             temp['e'] = temp['e'].astype('float64')
115         except:
116             temp['e'] = temp['e'].map(format_exp)
117         else:
118             temp['e'] = temp['e'].astype('float64')
119
120 #Writing results to array
121     SS = temp[['e']].to_numpy(dtype='float64')
122     SStemp = SS[200]
123 #Determine if e0 (0.245) is reached to determine where to calculate K0
124     if round(SStemp[0],4) == 0.245:
125         #Reading horizontal and vertical stresses from calculated values
126         colspecs = [(12, 25), (25, 38)]
127         names = ["sx", "sy"]
128         temp = pd.read_fwf('Ana.cal', encoding='shift_jis', colspecs=colspecs,
names=names, skiprows=10)
129         #Error handling
130         if temp['sx'].dtypes == 'object':
131             print(temp['sx'])
132             try:
133                 temp['sx'] = temp['e'].astype('float64')
134             except:
135                 temp['sx'] = temp['e'].map(format_exp)
136             else:
137                 temp['sx'] = temp['e'].astype('float64')
138         if temp['sy'].dtypes == 'object':
139             print(temp['sy'])
140             try:
141                 temp['sy'] = temp['e'].astype('float64')
142             except:
143                 temp['sy'] = temp['e'].map(format_exp)
144             else:
145                 temp['sy'] = temp['e'].astype('float64')
146         sxtemp = temp[['sx']].to_numpy(dtype='float64')
147         sytemp = temp[['sy']].to_numpy(dtype='float64')
148
149 #Calculate K0
150     K0 = sytemp[200]/sxtemp[200]
151 #Write K0 to txt file
152     with open('k0optvals.txt', 'a') as kopt:
153         kopt.write(str(K0))
154         kopt.write("\t")

```

```

155         kopt.write(str(itr))
156         kopt.write("\n")
157         kopt.close()
158
159     #Calculate residual
160     res = abs(0.245 - SS[200])
161
162     os.remove("Ana.cal")
163
164     return res
165
166 bnds = (0.245, 0.551)
167 x0 = 0.3341
168
169 #For each lift calculate the precompaction void ratio in order to generate the
   final void ratio by minimizing the
170 #residual using SciPy
171 for i in range(10):
172     k0paramopt = minimize_scalar(tijmodelfn, bounds=bnds, args=(i,), method='
   bounded')
173     with open('k0e0opt.txt', 'a') as opt:
174         resultx=str(k0paramopt.x)
175         opt.write(resultx)
176         opt.write("\n")
177         resultsuc=str(k0paramopt.message)
178         opt.write(resultsuc)
179         opt.write("\n")
180     opt.close()
181

```